IMPROVED MODELING OF UNSTEADY FREE SURFACE, PRESSURIZED AND MIXED FLOWS IN STORM-SEWER SYSTEMS

BY

ARTURO S. LEÓN

B.S., National University of San Cristobal de Huamanga, 1997
M.S., National University of Engineering, 2000

DISSERTATION

Submitted in partial fulfillment of the requirements
for the degree of Doctor of Philosophy in Civil Engineering
in the Graduate College of the
University of Illinois at Urbana-Champaign, 2007

Urbana, Illinois

Abstract

The main aim of this thesis is to advance our understanding of the process of flood-wave propagation through storm-sewer systems by improving the methods available for simulating unsteady flows in closed conduits ranging from free surface flows, to partly free surface-partly pressurized flows (mixed flows), to fully pressurized flows. Two fully-conservative, computationally efficient and robust models are formulated in this thesis. In the first model, pressurized flows are simulated as free surface flows using a hypothetical narrow open-top slot ("Preissmann slot"). In the second model, free surface and pressurized flows are treated independently while interacting through a moving interface. In the first model, a gradual transition between the pipe and the slot is introduced and an explicit Finite Volume (FV) Godunov-type Scheme (GTS) is used to solve the free surface flow governing equations. This model is called the *modified Preissmann model*. In the second model, both free surface and pressurized flows are handled using shock-capturing methods –specifically GTS schemes. Open channel-pressurized flow interfaces are treated using a shock-tracking-capturing approach. In this case, cell boundaries are introduced at the location of open channel-pressurized flow interfaces, subdividing some regular cells into two subcells, resulting in a variable mesh arrangement that varies from one time step to the next. For boundary conditions, an intrinsically conservative second-order accurate formulation is developed.

The proposed formulation for boundary conditions maintains the conservation property of FV schemes and does not require any special treatment to handle shocks at boundaries. Comparisons between simulated results and experiments reported in the literature show that the two formulated models can accurately describe complex flow features –such as negative open channel-pressurized flow interfaces, interface reversals, and open-channel surges– that have not been addressed well, or not considered at all, by previous models. Numerical simulations also show that the formulated models are able to produce stable results for strong (rapid) transients at field scale. The capability of the *modified Preissmann model* to simulate transient flows in complex hydraulic systems is demonstrated by its application to the Tunnel and Reservoir Plan (TARP) Calumet system in Chicago. In general, the scope of this work is limited to single-phase flows (liquids). However, a simplified model for air-water mixture flows, valid only when the amount of gas in the conduit is small, has been implemented in the pressurized flow regime. This work does not include the prediction of any type of air entrainment or air release.

Acknowledgements

This thesis would not have been possible without the support of many people. In particular the author wishes to express his sincere gratitude to his advisor, Prof. Marcelo H. García for his guidance and support throughout the graduate studies of the author. The author also wishes to thank Prof. Mohamed Ghidaoui of The Hong Kong University of Science and Technology for his insightful suggestions and comments during the preparation of this thesis. He also wishes to thank Dr. Arthur Schmidt for his invaluable help in many ways.

He also would like to express his gratitude to Professors Herman Krier, Gary Parker, Marcelo H. García and Arthur R. Schmidt for serving on the doctoral committee of the author.

The financial support of the Metropolitan Water Reclamation District of Greater Chicago and of the Civil and Environmental Engineering Department of the University of Illinois at Urbana-Champaign are also gratefully acknowledged.

The author is deeply indebted to his parents Cirilo León and Victoria Cuba for their love and encouragement throughout his life. Last, but not least, the author wishes to thank Hee Youn Cho for her friendship, love and continuous support. She also spent long hours helping the author with the editorial work needed to complete this thesis.

Table of Contents

List of Tables

List of Figures

List of Symbols

A = Cross-sectional area of flow
$\mathbf{A}$ = Jacobian matrix of flux vector
a = pressure-wave celerity in presence of liquid only
A_{dropsh} = horizontal cross-sectional area of dropshaft pond
A_f = full cross-sectional area of the pipe
a_g = general notation for pressure-wave celerity
a_m = pressure-wave celerity for the gas-liquid mixture
c = gravity wave celerity
$\bar{c}$ = average gravity wave celerity
c_1, c_2 = constants
Cr = Courant number
Cr_{max} = maximum Courant number
d = pipe diameter
E = total energy
E_0 = total energy at t=0
E_f = energy dissipation due to friction
E_t = total energy at time t
F = Froude number
$\mathbf{F}$ = Flux vector
f = Darcy-Weisbach friction factor
$\mathbf{F}^n_{i+1/2}$ = intercell flux
F_w = momentum term arising from the longitudinal variation of the channel width
g = acceleration due to gravity
H = absolute pressure head in meters of water
h = piezometric head measured over the conduit bottom
h_0 = reservoir head measured over the conduit bottom
i = mesh point location in x direction
$\mathbf{K}$ = eigenvector
k_f = bulk modulus of elasticity of the fluid
k_n = constant equal to 1.0 in Metric units and 1.49 in English units
L = length of pipe
M = Mass
M_0 = Mass at t=0
n_m = Manning roughness coefficient

Nx = Number of grids
p = pressure acting on the center of gravity of A_f
$\overline{p}$ = average pressure of the water column over the cross sectional area
Q = flow discharge
Q_m = mass flow discharge
R = hydraulic radius
$\mathbf{S}$ = vector containing source terms
s = wave speed
S_0 = bed slope
S_f = friction slope
s_L = left wave speed
s_R = right wave speed
T = top width
t = time
$\mathbf{U}$ = vector of flow variables
u = water velocity
$\overline{u}$ = average water velocity
$\mathbf{U}_i$ = vector of flow variables at node i
x = longitudinal coordinate
Y = Young's modulus of elasticity
y = water depth above channel bottom
$\overline{y}$ = vertical distance from the sewer invert to the centroid of the hydraulic area
y' = periodic perturbation
y_{dropsh} = water depth above dropshaft bottom
y_0 = uniform flow depth
z = elevation

$\alpha = \rho A$
β = coefficient equal to 1 for isothermal processes and 1.4 for adiabatic conditions
Δi = vector difference
Δt = time step
Δx = spatial mesh size
$\eta = A\overline{p}$
λ = eigenvalues
Ω = mass of fluid per unit length of conduit
$\phi = \int (c/A) dA$
ψ = volume fraction of gas
ρ_f = fluid density
θ = angle of reference

Superscripts

n = computational time level

Subscripts

i = mesh point location in x direction
L = left state
R = right state
$\star$ = star region
b = boundary
CFL = Courant-Friedrichs-Lewy criterion
ref = reference

IMPROVED MODELING OF UNSTEADY FREE SURFACE, PRESSURIZED AND MIXED FLOWS IN STORM-SEWER SYSTEMS

Arturo S. León, Ph.D.
Department of Civil and Environmental Engineering
University of Illinois at Urbana-Champaign, 2007
Marcelo H. García, Advisor

The main aim of this thesis is to advance our understanding of the process of flood-wave propagation through storm-sewer systems by improving the methods available for simulating unsteady flows in closed conduits ranging from free surface flows, to partly free surface-partly pressurized flows (mixed flows), to fully pressurized flows. Two fully-conservative, computationally efficient and robust models are formulated in this thesis. In the first model, pressurized flows are simulated as free surface flows using a hypothetical narrow open-top slot ("Preissmann slot"). In the second model, free surface and pressurized flows are treated independently while interacting through a moving interface. In the first model, a gradual transition between the pipe and the slot is introduced and an explicit Finite Volume (FV) Godunov-type Scheme (GTS) is used to solve the free surface flow governing equations. This model is called the *modified Preissmann model*. In the second model, both free surface and pressurized flows are handled using shock-capturing methods –specifically GTS schemes. Open channel-pressurized flow interfaces are treated using a shock-tracking-capturing approach. For boundary conditions, an intrinsically conservative second-order accurate formulation is developed. The proposed formulation for boundary conditions maintains the conservation property of FV schemes and does not require any special treatment to handle shocks at boundaries. Comparisons between simulated results and experiments reported in the literature show that the two formulated models can accurately describe complex flow features –such as negative open channel-

pressurized flow interfaces, interface reversals, and open-channel surges– that have not been addressed well, or not considered at all, by previous models. Numerical simulations also show that the formulated models are able to produce stable results for strong (rapid) transients at field scale. In general, the scope of this work is limited to single-phase flows (liquids). However, a simplified model for air-water mixture flows, valid only when the amount of gas in the conduit is small, has been implemented in the pressurized flow regime. This work does not include the prediction of any type of air entrainment or air release.

Chapter 1

Introduction

In closed conduit hydraulic systems, free surface and pressurized flows may co-exist simultaneously. For instance, Combined Sewer Overflow (CSO) systems are generally designed to operate in free surface flow regime. However, the large variations in the inflows together with the complex operation of these systems may result in flow conditions that vary from dry to free surface flow to partly free surface-partly pressurized flow (mixed flow), to fully pressurized flow. Transitions from one flow regime to another are governed by flow instabilities. The seminal articles by Yen (1986, 2001) classified the flow instabilities in a sewer pipe into the following five types: (1) Dry bed instability; (2) Supercritical-subcritical instability; (3) Roll wave instability; (4) Open channel-pressurized flow instability; and (5) Fully pressurized flow instability.

Yen (1986, pg. 283) wrote "None of these instabilities has been investigated in detail for unsteady flows, and perhaps except the second type instability they are not very well understood by most engineers." Unfortunately, and by and large, this remark is as valid today as it was then. While a few research attempts illuminated some of the features of these instabilities, this has not yet provided sufficient understanding to guide the development of new mathematical models.

The following discussion of the five types of instabilities summarizes the reviews of these instabilities by Yen (1986, 2001), highlights the main forces that are responsible for each instability and points out the features that a model needs to have to describe each instability.

Dry bed instability

This instability occurs when the bed is nearly dry, making it largely irrelevant to the study of sewer surcharging. This instability is governed by the gravity and surface tension forces in such a way that the fluid tends to collect in small isolated stagnant pools near the invert of the sewer when surface tension dominates, while a thin film (sheet) flow commences when gravity dominates. It must be noted, however, that flow routing through an originally dry sewer poses a major numerical difficulty at the wet-dry interface. The usual practice is to assume that the sewer is not completely dry, but has an initial thin film of water the depth of which depends on the capability of the numerical model. The same problem arises when the water level in the sewer becomes very small and most codes become unstable and produce negative water levels.

Supercritical-subcritical instability

The main forces that define the transition between supercritical and subcritical flow in a channel are the gravitational and inertial forces. The flow is supercritical when the Froude number is larger than unity and subcritical when the Froude number is smaller than unity. The fundamental difference between supercritical and subcritical regimes is related to whether flow disturbances can propagate in the direction opposite to the flow or not. In particular, while disturbances in a subcritical flow travel in both upstream and downstream directions, disturbances in a supercritical flow travel in the downstream direction only. The direction along which a disturbance can propagate has a profound implication in modeling open channel flows in sewers. For example, it is unphysical to impose external conditions at the downstream end of a sewer when the flow at this location is supercritical. Indeed, the solution of the open channel flow equations at a sewer boundary need to incorporate some conditions to check whether the flow is subcritical or supercritical so as to select the appropriate boundary conditions that need to be solved at the boundaries. The selection of appropriate boundary conditions can be very challenging when the flow at a particular boundary cycles rapidly between the subcritical and the supercritical regimes and often involves trial and error.

A number of processes and secondary instabilities lead to the formation of bores and jumps, also called shocks. Shocks are the final product of a complex chain of flow bifurcations initiated by the primary instability, namely, the supercritical-subcritical instability. For example, nonlinear and gravitational effects cause the flow at a shock to plunge into a roller. The flow in the roller is highly complex, involving air entrainment, strong turbulent actions and non-hydrostatic effects. Any model based on the shallow water equations has no hope of resolving the details of the flow inside the roller.

Fortunately, it turns out that flow details in a roller are not important for the computations of water level and flow rate in sewers and channels. The reasons for this are as follows. First, consider a control volume that extends from the front of the roller to its end. The complex mixing inside this control volume does not destroy mass. Also, the turbulent stresses inside this volume dissipate energy, but, being internal forces, do not destroy momentum. Therefore, it is sufficient to choose a model that can conserve mass and momentum, but not energy, across bores and jumps. The shallow water theory is well suited for this purpose. Second, the time and length scale of the roller are generally very small compared to the length and time scale that are of interest in sewer flows. This allows the modeler to treat the roller simply as a point of jump (discontinuity).

It is important to point out that the conceptualization of the roller by a discontinuity poses theoretical and numerical problems. Indeed, the differential form of the shallow water equations is invalid at the discontinuity, as the concept of derivatives simply fails at a jump. On the other hand, the integral form of the open channel flow equations across the discontinuity is valid since one can integrate a discontinuous function. Indeed, the integral form (also called the weak solution) gives the so-called shock conditions, which simply represent mass and momentum conservation across a jump. The validity of the integral form of the solution at a jump favors the use of Finite Volume schemes. Non-finite volume schemes often lead to non-physical oscillations near shock fronts.

The supercritical-subcritical instability is highly relevant to sewer surcharging. It is possible that this instability can induce water depths higher than the crown of the sewer, causing the transition to closed conduit flow. In addition, it is also possible that this instability triggers the open channel-pressurized flow instability even when the jump height is lower the sewer crown (see discussion below).

Roll wave instability

Roll waves can develop in perturbed steady supercritical flow when flow near the wave crests experience less resistance than the flow near the troughs. When this condition prevails, the wave front steepens since the flow near the crest catches up with the flow near the trough in front of it. The back of the wave, on the other hand, flattens out as the flow near the trough falls behind the flow near the wave crest. If the channel is long enough, the steepening of the wave fronts leads to the formation of hydraulic jumps (bores) and roll waves develop, where the flow surface becomes a series of quasi-periodic structures in the form of hydraulic jumps (bores) linked together by smooth gradually varying surface.

Most of the work on stability analysis (e.g., Dressler 1949, Kranenburg 1992, Brook et al. 1999) has been done for the case of steady uniform base flows and have shown that the critical Froude (F) number for the transition to roll waves is on the order of $F = 2.0$. When $F > 2.0$, the amplitude of small waves experiences an exponential growth at the initial stage. As the amplitude becomes large, nonlinear effects limit the growth of the instability, resulting in bores of constant amplitude. These estimates are based on depth-averaged shallow water equations when the momentum correction coefficient is equal to 1.0. However, Chen (1995) showed that the transitional Froude number is sensitive to the momentum correction factor.

The stability of a gradually varying flow in an open channel is studied in (Kranenburg 1990, Ghidaoui and Kolyshkin 2002). It is shown that the non-uniformity of the flow in the longitudinal direction has a significant impact on the flow stability. The spatial variability of the friction force in a non-uniform flow can induce conditions such that roll waves can develop in parameter regions that are deemed to be stable by the stability results of uniform flows.

Roll waves can be large enough to cause surcharging in sewers. Even when the jumps are not high enough to cause surcharging, roll waves can interact with the air in the gap between the water surface and crown, leading to open channel-pressurized flow instability, which causes surcharging. Therefore, the accuracy by which a model can predict the formation and amplitude of roll waves is important. Recall that the shallow water equations assume that the pressure is hydrostatic, and the wall shear during unsteady flow conditions is given by relations that are derived for steady flow conditions. These assumptions are questionable in roll wave flows. As a result, models that use the shallow water equations may not accurately predict the amplitude and speed of roll waves and may even predict that there are no roll waves when in fact these waves exist.

The comments on numerical modeling stated earlier in relation to the supercritical-subcritical instability remain valid for the case of roll waves since these waves contain jumps. In addition, the numerical scheme needs to have little numerical dissipation in order to allow for small waves to develop into roll waves when flow conditions are favorable. Large numerical dissipation can artificially suppress the growth of instabilities. It is also important to note that modelers may need to impose perturbations on their steady state solutions in order to investigate whether the steady state solutions are stable or whether roll waves will develop. Such perturbations are always present in real sewer flows, but not necessarily in mathematical models; thus, resulting in the need for introducing them by the modeler.

Open channel-pressurized flow instability

There are a number of mechanisms that lead to the transition from open channel to pressurized flow in a sewer. One of these mechanisms is the rapid increase of water depth following a sudden change at the boundaries of the sewer lines. Examples include a sudden rise of water level in a manhole or dropshaft, a sudden closure of a gate or stoppage of a pump at downstream end of a sewer, or a sudden opening of a gate at the upstream end of a sewer. Accurate modeling of the inception of surcharging by flow changes at boundary elements requires in-depth understanding of the flow's physics, not only inside the sewer, but also at its boundaries.

Another important surcharging mechanism is due to the Helmholtz instability that develops at the air-water interface inside a sewer line, causing entrapment of air cavities and large pressure oscillations. The Helmholtz instability occurs in regions inside the sewer where there is large difference between the speed of the air layer and the speed of the water layer. Differences in velocity between the air layer and the water layer underneath it can, for example, occur when there is a hydraulic jump or a shock front, which pushes the air in front in the direction opposite to the water layer. A counter current can also be set up when the water level at the downstream boundary drops suddenly below the sewer crown, causing the water to move out of the sewer while air rushes into the sewer to fill the void left by the water. The velocity differential at the air-water interface, along with the inevitable presence of surface water waves, causes the air pressure to be lowest near the crests of the perturbed interface and highest near its troughs. This pressure difference pushes the crest of the wave upward while the gravity force pulls the crest downward. The instability sets in when the pressure difference is larger than gravitational force (e.g., Kordyban 1977, Hamam and McCorquodale 1982). The amplitude of the water waves can become sufficiently large to reach the crown of the pipe (i.e., causing the air column to be bridged by water). As a result, air becomes trapped between successive water columns. The Helmholtz instability at the interface of two fluids with different speeds is a classical problem in fluid mechanics and its treatment can be found in numerous books, papers and monographs. However, these studies are often performed under geometrical and dynamic conditions that are very different from those in sewer flows.

A third surcharging mechanism, which is hereafter referred to as the geometrical instability, is due to the fact that the maximum steady surface flow in a converging sewer occurs at a water depth below the crown. The geometrical instability occurs when the wetted perimeter and thus the resistance force increase much faster than the inertial force as the water depth increases. This occurs in sewers with converging sections such as circular cross sections. Therefore, any increase in flow beyond the water level corresponding to maximum flow will cause flow oscillations and a sudden jump to pressurized flow (Yen 1986, 2001). The flow is found to become highly unstable at relative depths greater than 0.8 for sewers with circular cross sections. It is worthwhile to note that the flowrate in a sewer with circular cross section at a relative depth of about 0.8 is the same as when the sewer is full. The results of Hamam and McCorquodale (1982) indirectly show how the Helmholtz instability interacts with the geometric instability in such a way as to limit the range of gravity flows to depths below about 0.8 times the sewer diameter.

Another surcharging mechanism pointed out by Yen (1986, 2001) is due to lack of enough air supply into the sewer to compensate for the deficit created by entrainment of air at the air-water interface inside the sewer. The air entrainment is due to a shear instability at the air-water interface. The negative pressure created by the air deficit can cause increased flow oscillations resulting in sewer surcharging. A few illustrative examples are given in Yen (1986, 2001). Pressurization of the air phase in poor air ventilation has also been found to result in pre-bore motion or in the formation of gravity current flow where an air wedge at the top moves in opposite direction to the bore (Vasconcelos and Wright 2003).

Fully pressurized flow instability

This instability is associated with the geysering phenomena known to have occurred in numerous drainage systems. Preliminary work related to this instability can be found in Guo and Song (1991) and in the references listed in their paper. Consider a junction where a manhole or a dropshaft is connected to surcharged sewer lines. The pressure and flow variation at the junction acts as a forcing function to the water level in the manhole (dropshaft). Further forcing can be due to sudden runoff events. The water depth in the junction can become very high and may result in flooding and geysering when the forcing frequency by the runoff input and/or the waterhammer oscillation at the junction reaches the natural frequency of the manhole or the dropshaft or when the inflow is simply much higher than the outflow.

The physical processes leading to geysering or manhole overtopping are, generally, well understood. However, the quantitative analysis of geysering would require accurate estimation of runoff into junctions, accurate modeling of surcharging in the sewers and accurate formulation of flow behavior in manholes and dropshafts. It is noted that this instability is, often, preceded by the other four instabilities; thus, it is necessary that all other instabilities are well understood and modeled if geysering is to be predicted and mitigated.

As of examples of storm-sewer systems that have experienced surcharging, blow-off of manhole covers and geysering, many cases are reported in the literature (e.g., Hamam 1982, Guo and Song 1990). One example is a 10-foot trunk sewer in Hamilton, Ontario that experienced severe pressure transients during high flows (Hamam 1982). The pressure surges were large enough to blow a welded manhole cover off a dropshaft and cause basement flooding. Another well known system that has experienced structural and equipment damage as well as geysers above ground level associated with severe pressure transients is the Tunnel and Reservoir Plan (TARP) system in Chicago, Illinois (Guo and Song 1990). This was one of the first tunnel systems constructed in the United States for CSO control. Severe surge and geyser conditions developed during the early phases of implementation of the tunnel system resulted in the need to retrofit controls. At laboratory scale, Bziuk (1988) carried out over 200 mixed flow experiments on a storm-sewer model with an inlet dropshaft and demonstrated that severe pressure transients could occur during mixed-flow conditions. Since severe transients may occur in free surface, mixed or pressurized flow conditions, any realistic transient model of closed conduit systems must be capable of simulating, unsteady free surface flows, unsteady pressurized flows and the simultaneous occurrence of free surface and pressurized flows.

A transient flow model must not only be able to reproduce accurately the physical phenomena, but also be efficient numerically. For a given grid size and Courant number, one numerical scheme can be more accurate than another, but not necessarily more efficient numerically. A comparison of efficiency requires measuring the Central Processing Unit (CPU) time needed by each scheme to achieve the same level of accuracy (e.g., Zhao and Ghidaoui 2004). The computational speed or efficiency is of paramount importance for simulating the formation and propagation of hydraulic transients, where small simulation time steps are needed to reproduce the rapidly varying hydraulics. In particular the numerical efficiency is a critical factor for real-time control (RTC), since several simulations are required within a control loop in order to optimize the control strategy.

To date, mixed flows are simulated by one of two general approaches: (a) simulation of pressurized flows as free surface flows using a hypothetical narrow open-top slot ("Preissmann slot"); and (b) separate simulation of the free surface and pressurized flows. The Preissmann slot approach is computationally simpler as it only requires solution for one flow type (free surface flow); however this method may present accuracy and stability problems associated with the width and shape of the hypothetical slot and it can not simulate sub-atmospheric pressures.

The separate simulation of free surface and pressurized flows is more complex; however the methods based on this approach are able to simulate sub-atmospheric pressures in the pressurized flow regime. Current models based on this approach can not address some complex flow features well, such as open-channel surges, negative open channel-pressurized flow interfaces and interface reversals. In this approach, the location of the moving interface between the two flow types is tracked and treated as an internal interface. This is often referred to as the "shock-fitting" method (e.g., Guo and Song 1990, Fuamba 2002).

Recently, Vasconcelos et al. (2006) introduced a Decoupled Pressure Approach (DPA), which is formulated by modifying the open-channel Saint-

Venant equations to allow for overpressurization assuming that elastic behavior of the pipe walls will account for the gain in pipe storage. This model has been tested only using weak transients and it may present numerical instability problems.

Regardless of the approach used for simulating mixed flows, most of the models developed primarily to examine the formation and propagation of hydraulic transients use schemes based on the Method of Characteristics (MOC) to solve the governing equations (free surface and pressurized flows). The MOC transforms the partial differential equations of continuity and momentum into a set of ordinary differential equations that are relatively easy to solve. As a result, many methods and strategies have been developed to apply the MOC to one-dimensional flows. Among the benefits of MOC schemes are methods to incorporate complex boundary conditions into MOC solutions. Although the MOC can easily handle complex boundary conditions, interpolations necessary for Courant numbers less than 1.0 together with the fact that these schemes are not intrinsically conservative (mass and momentum are not conserved) result in smoothing (damping) of waves and diffusion of the wave fronts; diffusion makes waves arrive earlier to the boundaries, and damping reduces the wave peak and may artificially delay the time of occurrence of surcharging. Therefore, what is needed is a computationally efficient scheme that retains the same ability as the MOC in terms of handling boundary conditions, but provides higher resolution of waves.

In regard to boundary conditions (BC), the author is not aware of any model for sewer systems that uses a high-order BC at the extremes of the computational domain (boundaries). A numerical scheme may have second or higher-order accuracy in the internal cells, however if this scheme is coupled with BCs having only first-order accuracy, a degradation of the accuracy of the numerical solution in the internal cells may occur. Another issue of BCs in sewer systems that requires attention is the treatment of shocks at boundaries. Most of the current models implemented for transient flows in sewer systems use the theory of characteristics or Riemann invariants to connect the boundaries with the internal cells. Although this approach is accurate for smooth waves, important wave smoothing (damping) may occur when shocks are present at boundaries. Therefore, what is needed is a formulation of BCs that can achieve the same accuracy of the internal cells and that can handle shocks at boundaries well.

The broad objective of this thesis is to advance our understanding of the process of flood-wave propagation through storm-sewer systems by improving the methods available for simulating unsteady flows in closed conduits ranging from free surface flows, to mixed flows, to fully pressurized flows. The specific objectives of this work are:

1. The development and implementation of two efficient and robust models for simulating unsteady flows in closed conduits ranging from free surface flows, to partly free surface-partly pressurized flows, to fully pressurized flows, that can accurately describe complex flow features –such as negative open channel-pressurized flow interfaces, interface reversals, and open-channel surges. In the first model, pressurized flows are simulated as free surface flows using a hypothetical narrow open-top slot ("Preissmann slot"). In the second model, free surface and pressurized flows are treated independently while interacting through a moving interface. In the first model, a gradual transition between the pipe and the slot is introduced and the free surface flow governing equations

are solved using Godunov-type Schemes (GTS). This model is called the *modified Preissmann model*. GTS schemes belong to the family of shock-capturing methods. These methods capture discontinuities in the solution automatically, without explicitly tracking them (LeVeque 2002). In the second model, both free surface and pressurized flows are handled using shock-capturing methods –specifically GTS schemes. The moving interfaces between the two flow types are handled using a shock-tracking-capturing approach. In this case, cell boundaries are introduced at the location of open channel-pressurized flow interfaces, subdividing some regular cells into two subcells, resulting in a variable mesh arrangement that varies from one time step to the next. However, the vast majority of grid cells do not vary.

2. The implementation of intrinsically conservative and second-order accurate boundary conditions (same accuracy of internal cells).

3. The application of the *modified Preissmann model* to simulate transient flows in complex hydraulic systems. The Tunnel and Reservoir Plan (TARP) Calumet system of the Metropolitan Water Reclamation District of Greater Chicago is used as the test case.

In general, the scope of this work is limited to single-phase flows (liquids). However, a simplified model for air-water mixture flows, which is valid when the amount of gas in the conduit is small, has been implemented in the pressurized flow regime. This work does not include the prediction of any type of air entrainment or air release.

This thesis comprises six chapters, including this introduction. Since the models proposed in this thesis are intended for simulating free surface, pressurized and mixed flows, the description of the models is divided into three chapters: free surface flows (Chapter 2), pressurized flows (Chapter 3) and mixed flows (Chapter 4). The discussion on dry bed flows is included in Chapter 4. No specific chapter for a literature review was included, however, a brief review of the strengths and limitations of the current approaches for simulating transient mixed flows was presented earlier in this chapter. In-depth literature review of these approaches and of their numerical solutions can be found in Chapter 4. For free surface and pressurized flows, a literature review for the numerical solution of their governing equations is included at the beginning of its respective chapter. Chapter 5 deals with the application of the *modified Preissmann model* to the TARP Calumet system, and finally, Chapter 6 summarizes the conclusions of the thesis.

Chapter 2

Free surface flows

2.1 Introduction

Unsteady gravity flows in sewers have been traditionally modeled by numerically solving the one-dimensional equations of continuity and momentum. Commonly used models range in sophistication from kinematic wave to full dynamic wave solution of these equations (Yen 2001). Most of the models that solve these equations at the level of the full dynamic wave use an implicit finite-difference scheme when the formation of transients is secondary to issues such as conveyance capacity. However, most of the models developed primarily to examine the formation of hydraulic transients use schemes based on the Method Of Characteristics (MOC). The MOC can easily handle complex boundary conditions, however, interpolations necessary for Courant numbers less than one result in smoothing (damping) of waves and diffusion of the wave fronts; diffusion makes waves arrive earlier to the boundaries, and damping reduces the wave peak and may artificially delay the time of occurrence of surcharging. Therefore, what is needed is a computationally efficient scheme that retains the same ability as the MOC in terms of handling boundary conditions, but provides higher resolution of waves in sewers.

Godunov Type Schemes (GTS) for the solution of shallow water equations have been the subject of considerable research (Glaister 1988, Alcrudo et al. 1992, Fujihara and Borthwick 2000, Sanders 2001, Toro 2001, Caleffi et al. 2003, Zoppou and Roberts 2003). These schemes belong to the family of shock-capturing methods. These methods capture discontinuities in the solution automatically, without explicitly tracking them (LeVeque 2002). Discontinuities must then be smeared over one or more grid cells. Success requires that the method implicitly incorporate the correct jump conditions, reduce smearing to a minimum, and not introduce nonphysical oscillations near the discontinuities. GTS schemes fall within the group of Finite Volume (FV) methods that have the ability to conserve mass and momentum and to provide sharp resolution of discontinuities without spurious oscillations (Hirsch 1990). Additionally, unlike the MOC schemes, the resolution of GTS is not significantly reduced for low Courant numbers. Furthermore, the boundary conditions for these schemes are treated in a similar way to the MOC. Historically, a GTS for flows in rectangular channels was first implemented by Glaister (1988) and for non-rectangular prismatic channels by Alcrudo et al. (1992). Later, another scheme for non-prismatic channels was implemented and applied to triangular and trapezoidal channels by Sanders (2001). Lately, GTS methods for simulating transient free surface flows in sewers were implemented by León et al. (2006a). The latter also compared the accuracy and efficiency of GTS methods with that of MOC schemes. These authors show that, for a given level of accuracy, the second-order GTS schemes are significantly faster to execute than the fixed-grid MOC with space-line interpolation, and in some cases, the accuracy produced by the GTS schemes can not be matched by the accuracy of the MOC scheme, even when a Courant number close to one and a large number of grids is used.

The present chapter is based on León et al. (2005) and León et al. (2006a). This chapter is organized as follows: (1) the governing equations are presented in conservation-law form; (2) the corresponding integral form and FV discretization is described; (3) two Riemann solvers for the flux computation at the cell interfaces are provided; (4) a brief description for the formulation of boundary conditions is presented; (5) the stability constraints for the source term discretized using the second-order Runge-Kutta are formulated; and (6) the schemes are tested using several problems whose solution contain features that are relevant to transient flows in sewers. Finally, the results are summarized in the conclusion.

2.2 Governing equations

One-dimensional open-channel flow continuity and momentum equations for non prismatic channels or rivers may be written in its vector conservative form as follows (Chaudhry 1987):

$$\frac{\partial \mathbf{U}}{\partial t} + \frac{\partial \mathbf{F}}{\partial x} = \mathbf{S} \tag{2.1}$$

where the vector variable $\mathbf{U}$, the flux vector $\mathbf{F}$ and the source term vector $\mathbf{S}$ are given respectively by:

$$\mathbf{U} = \begin{bmatrix} A \\ Q \end{bmatrix}, \ \mathbf{F} = \begin{bmatrix} Q \\ \frac{Q^2}{A} + \frac{A\overline{p}}{\rho} \end{bmatrix} \text{ and } \mathbf{S} = \begin{bmatrix} 0 \\ F_w + (S_0 - S_f)gA \end{bmatrix} \tag{2.2}$$

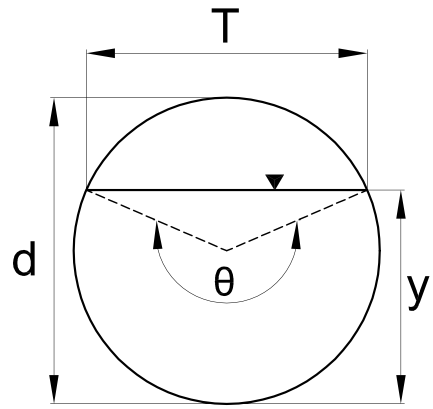

Figure 2.1: Definition of variables in circular cross-sections.

where A = cross-sectional area of the channel; Q = flow discharge; $\overline{p}$ = average pressure of the water column over the cross sectional area; ρ = liquid density; g = gravitational acceleration; S_0 = slope of the bottom channel; S_f = slope of the energy line, which may be estimated using an empirical formula such as the Manning's equation; and F_w = momentum term arising from the longitudinal variation of the channel width. For a circular cross-section channel (Fig. 2.1), F_w becomes zero, the hydraulic area is given by $A = d^2/8(\theta - \sin\theta)$, the hydraulic radius by $R = d/4(1 - \sin\theta/\theta)$, and the term $A\overline{p}/\rho$ contained in the flux term $\mathbf{F}$ in Eq. (2.2) is given by

$$\frac{A\overline{p}}{\rho} = \frac{g}{12}\left[(3d^2 - 4dy + 4y^2)\sqrt{y(d-y)} - 3d^2(d-2y)\arctan\frac{\sqrt{y}}{\sqrt{d-y}}\right] \quad (2.3)$$

where d is the diameter of the circular cross-section channel and y is the water depth.

2.3 Formulation of finite volume Godunov-type schemes

This method is based on writing the governing equations in integral form over an elementary control volume or cell, hence the general term of Finite Volume (FV) method. The computational grid or cell involves the discretization of the spatial domain x into cells of length Δx and the temporal domain t into intervals of duration Δt. The ith cell is centered at node i and extends from $i-1/2$ to $i+1/2$. The flow variables (A and Q) are defined at the cell centers i and represent their average value within each cell. Fluxes, on the other hand are evaluated at the interfaces between cells ($i-1/2$ and $i+1/2$). For the ith cell, the integration of Eq. (2.1) with respect to x from control surface $i-1/2$ to control surface $i+1/2$ yields:

$$\frac{\partial}{\partial t}\int_{i-1/2}^{i+1/2} \mathbf{U} dx + \mathbf{F}_{i+1/2} - \mathbf{F}_{i-1/2} = \int_{i-1/2}^{i+1/2} \mathbf{S} dx \tag{2.4}$$

Recalling that the flow variables (A and Q) are averaged over the cell, the application of Green's theorem to Eq. (2.4), gives:

$$\mathbf{U}_i^{n+1} = \mathbf{U}_i^n - \frac{\Delta t}{\Delta x}(\mathbf{F}_{i+1/2}^n - \mathbf{F}_{i-1/2}^n) + \frac{\Delta t}{\Delta x}\int_{i-1/2}^{i+1/2} \mathbf{S} dx \tag{2.5}$$

where the superscripts n and $n+1$ reflect the t and $t+\Delta t$ time levels respectively. In Eq. (2.5), the determination of $\mathbf{U}$ at the new time step $n+1$ requires the computation of the numerical flux at the cell interfaces at the old time n and the evaluation of the source term. The source terms are introduced into the solution through a second-order time splitting. The evaluation of the flux term is presented in the next section.

2.3.1 Flux computation

In the Godunov approach, the numerical flux is determined by solving a local Riemann problem at each cell interface. The Riemann problem for a general hyperbolic system is the following initial-value problem:

$$\frac{\partial \mathbf{U}}{\partial t} + \frac{\partial \mathbf{F}}{\partial x} = 0 \tag{2.6}$$

$$\mathbf{U}_x^n = \begin{cases} \mathbf{U}_L^n & \text{for } x \leq x_{i+1/2} \\ \mathbf{U}_R^n & \text{for } x > x_{i+1/2} \end{cases} \tag{2.7}$$

For each cell interface, the states $\mathbf{U}_L^n$ and $\mathbf{U}_R^n$ are estimated from a polynomial reconstruction whose order determines the accuracy of the scheme. For Godunov's first-order accuracy method, a piecewise constant polynomial is used, whereas a second-order accuracy scheme is produced if linear interpolation is used. Higher order accuracy Godunov schemes are found using higher order polynomials. Only first-order accuracy schemes produce monotone preserving solutions (Godunov 1959), however the accuracy of these schemes in smooth regions is of order one and a very fine grid would be required to minimize numerical errors. The rate of convergence of second or higher order schemes is much better than first order schemes. Therefore, to achieve a given level of accuracy, higher order schemes require much less grid points than the first order schemes. However, higher order schemes are prone to spurious oscillations in the vicinity of discontinuities. Total Variation Diminishing (TVD) methods may be used to avoid oscillations near sharp flow features and to preserve the accuracy of the schemes away from discontinuities. In this chapter, second-order accuracy in space and time is obtained by using a Monotone Upstream-centred Scheme for Conservation Laws (MUSCL) reconstruction in conjunction with a Hancock two-stage scheme for advancing the cell average solution from one time level to the next (e.g., Toro 2001). The TVD property of this method is ensured by applying the MINMOD pre-processing slope limiter (e.g., Toro 2001).

The intercell flux $\mathbf{F}_{i+1/2}$ is computed using an exact or approximate solution of the Riemann Problem. The intercell flux is then used to update $\mathbf{U}$ at the nodes. In order to reduce the computational time, the exact solution of the Riemann problem is usually replaced with an approximate one. These approximate solvers, if carefully selected, may lead to robust schemes with very good accuracy and that are simple to implement. In what follows, two efficient approximate Riemann solvers are derived for general cross-section open-channel flows and then applied for circular conduits.

2.3.2 Guinot approximate-state Riemann solver

In this approach, the solution of the Riemann problem is approximated by an intermediate region $\mathbf{U}_\star$ of constant state separated from the left and right states $\mathbf{U}_L$ and $\mathbf{U}_R$ by two waves that may be rarefactions or shocks (Fig. 2.2). From these three states only the intermediate state is unknown. This unknown state is obtained by assuming that the flow is continuous across these two waves (two rarefaction waves) and consequently the differential relationships provided by the generalized Riemann invariants hold across these waves. The derivation of the unknown state is presented next.

The characteristic form of Eq. (2.6) obtained by expressing the Jacobian matrix of $\mathbf{F}$ with respect to $\mathbf{U}$ is:

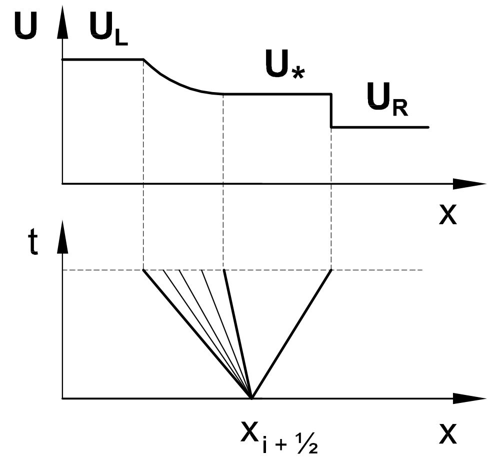

Figure 2.2: Principle of the Guinot Riemann solver in the physical space (top) and in the phase space (bottom).

$$\frac{\partial \mathbf{U}}{\partial t} + \mathbf{A}\frac{\partial \mathbf{U}}{\partial x} = 0, \quad \text{where } \mathbf{A} = \begin{bmatrix} 0 & 1 \\ c^2 - u^2 & 2u \end{bmatrix}$$

where u is the water velocity and c the celerity of the gravity wave in still water given by:

$$c = \sqrt{g\frac{d}{8}}\sqrt{\frac{\theta - \sin\theta}{\sin\frac{\theta}{2}}} \tag{2.8}$$

The eigenvalues (λ) and eigenvectors ($\mathbf{K}$) of $\mathbf{A}$ are given by: $\lambda_1 = u - c$, $\lambda_2 = u + c$, $\mathbf{K}_1^T = [1 \;\; u - c]$ and $\mathbf{K}_2^T = [1 \;\; u + c]$. These eigenvectors yield the following generalized Riemann invariants:

$$\begin{aligned} \tfrac{dA}{1} &= \tfrac{dQ}{u-c} \text{ across } \tfrac{dx}{dt} = u - c \\ \tfrac{dA}{1} &= \tfrac{dQ}{u+c} \text{ across } \tfrac{dx}{dt} = u + c \end{aligned} \tag{2.9}$$

The differential relationship across the first wave $dx/dt = u - c$ can be written as $(u - c)dA = dQ$, but since $dQ = udA + Adu$, it can be further simplified to

$du + (c/A)dA = 0$, which can be expressed as:

$$du + d\phi = 0 \tag{2.10}$$

where $\phi = \int (c/A)dA$. For a general cross section channel, ϕ can be determined approximately by integrating c/A between two successive values of A using any integration technique. For a circular cross-section (Fig. 1), ϕ is given by:

$$\phi = \sqrt{g\frac{d}{8}} \int_0^\theta \frac{1-\cos\theta}{\sqrt{(\theta - \sin\theta)\sin(\frac{\theta}{2})}}\, d\theta \tag{2.11}$$

Since an analytical integration for ϕ has not been found, the expression inside the integral in Eq. (2.11) was expressed in series and then integrated from 0 to θ resulting in:

$$\phi = \sqrt{g\frac{d}{8}}\left[\sqrt{3}\,\theta - \frac{\sqrt{3}}{80}\theta^3 + \frac{19\sqrt{3}}{448000}\theta^5 + \frac{\sqrt{3}}{10035200}\theta^7 + \frac{491\sqrt{3}}{27\times 7064780800}\theta^9 + ...\right] \tag{2.12}$$

By integrating the differential relationship across the first wave $dx/dt = u - c$ (Eq. 2.10) the following relationship is obtained.

$$u_L + \phi_L = u_\star + \phi_\star \tag{2.13}$$

Similarly, the generalized Riemann invariants across $dx/dt = u + c$ lead to the following relationship:

$$u_\star - \phi_\star = u_R - \phi_R \tag{2.14}$$

By combining Eqs. (2.13) and (2.14), the flow variables in the intermediate state (star region) are obtained:

$$u_\star = \frac{u_L + u_R}{2} + \frac{\phi_L - \phi_R}{2} \tag{2.15}$$

$$\phi_\star = \frac{\phi_L + \phi_R}{2} + \frac{u_L - u_R}{2} \tag{2.16}$$

If the left or right wave is a shock, the speed of this shock (c_s) can be computed by applying the Rankine-Hugoniot condition to either the continuity or the momentum equation. This gives the following relations:

$$\begin{aligned} c_{s\ (K\ =\ L,\ R)} &= \frac{Q_\star - Q_K}{A_\star - A_K} \\ c_{s\ (K\ =\ L,\ R)} &= \frac{\frac{Q_\star^2}{A_\star} - \frac{Q_K^2}{A_K} + \frac{A_\star \overline{p}_\star}{\rho} - \frac{A_K \overline{p}_K}{\rho}}{Q_\star - Q_K} \end{aligned} \tag{2.17}$$

After the computation of all the wave celerities and shock speeds (if present), it is possible to determine in which region the initial discontinuity is located and thus to compute the flux. In what follows, the scheme due to Guinot (2003) is summarized:

1. Compute $u_\star$ (or $Q_\star$) and $\phi_\star$ (or $A_\star$) using the Eqs. (2.15) and (2.16).
2. Determine u (or Q) and ϕ (or A) at the interface $i{+}1/2$ from the following tests:
   (a) if $s_L \geq 0$ and $s1_\star < 0$ the first wave is a shock. The shock speed c_s must be computed with $K = L$ using one of the relations given in the system of Eqs. (2.17). The solution is given by $\mathbf{U}_L$ if $c_s > 0$ and by $\mathbf{U}_\star$ otherwise.

(b) if $s_L \geq 0$ and $s1_\star > 0$ the solution is given by $\mathbf{U}_L$ regardless of the nature of the first wave.

(c) if $s_L < 0$ and $s1_\star > 0$ the solution is obtained by solving Eq. (2.13) with $u_\star = c_\star$.

(d) if $s1_\star \leq 0$ and $s2_\star \geq 0$ the solution is given by $\mathbf{U}_\star$.

(e) if $s2_\star < 0$ and $s_R > 0$ the solution is obtained by solving Eq. (2.14) with $u_\star = -c_\star$.

(f) if $s_R \leq 0$ and $s2_\star > 0$ the second wave is a shock. The shock speed c_s must be computed with $K = R$ using one of the relations given in the system of Eqs. (2.17). The solution is given by $\mathbf{U}_R$ if $c_s < 0$ and by $\mathbf{U}_\star$ otherwise.

(g) if $s_R \leq 0$ and $s2_\star < 0$ the solution is given by $\mathbf{U}_R$ regardless of the nature of the second wave.

where $s_L = u_L - c_L$, $s1_\star = u_\star - c_\star$, $s2_\star = u_\star + c_\star$ and $s_R = u_R + c_R$.

3. Once the flow variables (A and Q) at the interface $i + 1/2$ are known, the flux at the interface is computed using the Eq. (2.2).

2.3.3 HLL approximate Riemann solver

The HLL Riemann solver takes its name from the initials of Harten, Lax and Van Leer (Toro 2001). In this approach, the solution of the Riemann problem is approximated by an intermediate region $\mathbf{U}_\star$ of constant state separated from the left and right states $\mathbf{U}_L$ and $\mathbf{U}_R$ by two infinitely thin waves (shocks). Fig. 2.3 illustrates this approximation. In this method, the numerical flux $\mathbf{F}_{i+1/2}$ is obtained by applying the integral form of the conservation laws in appropriate control volumes yielding:

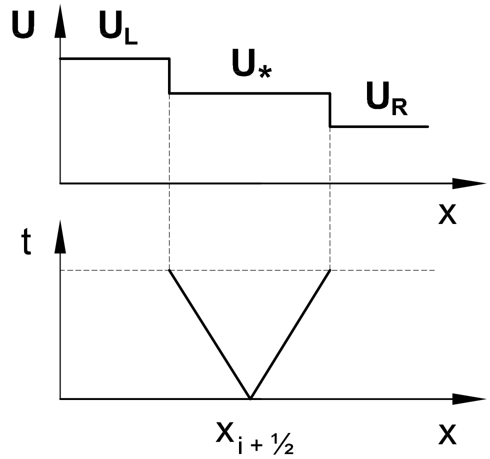

Figure 2.3: Principle of the HLL Riemann solver in the physical space (top) and in the phase space (bottom).

$$\mathbf{F}_{i+1/2} = \begin{cases} \mathbf{F}_L & \text{if } s_L > 0 \\ \frac{s_R\mathbf{F}_L - s_L\mathbf{F}_R + s_R s_L(\mathbf{U}_R - \mathbf{U}_L)}{s_R - s_L} & \text{if } s_L \leq 0 \leq s_R \\ \mathbf{F}_R & \text{if } s_R < 0 \end{cases} \tag{2.18}$$

where s_L and s_R are the wave speed estimates for the left and right waves, respectively. It can be noticed in Eq. (2.18) that the first and third fluxes correspond to supercritical flows moving to the right and left, respectively and the second one corresponds to a subcritical flow moving to the right or left. The wave speeds s_L and s_R are determined by eliminating $Q_\star$ in the system of Eqs. (2.17), resulting in:

$$s_L = u_L - M_L \, , \; s_R = u_R + M_R \tag{2.19}$$

where M_K ($K = L$, R) is given by

$$M_K = \sqrt{\left(\frac{A_\star \overline{p}_\star}{\rho} - \frac{A_K \overline{p}_K}{\rho}\right) \frac{A_\star}{A_K(A_\star - A_K)}} \tag{2.20}$$

where $A_\star$ is an estimate for the exact solution of A in the star region. Toro (2001) suggested several estimates for the flow depth in the star region ($y_\star$) in rectangular channels. Following some of these estimates are extended for a general cross-section channel.

Assuming the two-rarefaction wave approximation, an estimate for $\phi_\star$ (or equivalently $A_\star$) is given by Eq. (2.16). Since $A_\star$ and $\phi_\star$ are functions of θ, to determine $A_\star$, it is required to solve Eq. (2.16) for θ by iteration.

Another relation for $A_\star$ can be obtained by solving the Riemann problem for the linearized hyperbolic system $\partial \mathbf{U}/\partial t + \partial \mathbf{F}(\mathbf{U})/\partial x = 0$ with $\mathbf{F}(\mathbf{U}) \equiv \overline{\mathbf{A}}\mathbf{U}$, $\overline{\mathbf{A}} = \mathbf{A}(\overline{\mathbf{U}})$ and $\overline{\mathbf{U}} \equiv (\mathbf{U}_L + \mathbf{U}_R)/2$. The two eigenvalues for the matrix $\overline{\mathbf{A}}$ are given by: $\overline{\lambda}_1 = \overline{u} - \overline{c}$ and $\overline{\lambda}_2 = \overline{u} + \overline{c}$. The application of the Rankine-Hugoniot condition across the two waves [$\overline{\lambda}_i$ $(i = 1, 2)$] provides the following relation for $A_\star$:

$$A_\star = \frac{A_R + A_L}{2} + \frac{\bar{A}}{2\bar{c}}(u_L - u_R) \tag{2.21}$$

where $\bar{A} = (A_R + A_L)/2$ and $\bar{c} = (c_R + c_L)/2$.

Unlike in the case of Eq. (2.16), in Eq. (2.21) no iteration is required to estimate $A_\star$.

Another estimate for $A_\star$ that preserves the simplicity of Eq. (2.21) while adding two important new properties may be obtained based on the depth positivity condition (flow depth is greater than or equal to zero). The added properties are (Toro 2001): (1) it can handle situations involving very shallow water well; and (2) unlike the Riemann solver given in Eq. (2.21), the Riemann solver based on the depth positivity condition is found to be very robust in dealing with shock waves. Following a Riemann solver based on the depth positivity condition is derived.

In Eq. (2.16), enforcing $\phi_\star \geq 0$ leads to the depth positivity condition for the two-rarefaction wave approximation that is a limiting case contained in the exact solution of the Riemann problem.

$$u_R - u_L \leq \phi_R + \phi_L \tag{2.22}$$

To allow the simple solver given in Eq. (2.21) to have the same depth positivity condition as that of the exact solution of the Riemann problem, Eq. (2.21) is written as:

$$A_\star = \frac{A_R + A_L}{2} + \frac{u_L - u_R}{2\overline{W}} \tag{2.23}$$

where $\overline{W}$ is a parameter to be determined by enforcing that Eq. (2.23) has the same depth positivity condition as that of the exact solution of the Riemann problem.

Likewise, in Eq. (2.23), enforcing the condition $A_\star \geq 0$ leads to:

$$u_R - u_L \leq \overline{W}(A_R + A_L) \tag{2.24}$$

The right hand sides of Eqs. (2.22) and (2.24) are equal in the dry bed limit ($y_\star = 0$), since both Riemann solutions (linearized Riemann solver and the one based on the two-rarefaction wave approximation) achieve their limiting value when the flow depth is zero. This condition ensures that the approximate solver (linearized Riemann solver) satisfies the same positivity condition as that of the exact Riemann solution. Hence, comparing the right-hand sides of Eqs. (2.22) and (2.24), the parameter $\overline{W}$ is determined as:

$$\overline{W} = \frac{\phi_R + \phi_L}{A_R + A_L} \tag{2.25}$$

which can be substituted in Eq. (2.23), leading to another estimate for $A_\star$ based on the depth positivity condition;

$$A_\star = \frac{A_R + A_L}{2}\left[1 + \frac{u_L - u_R}{\phi_R + \phi_L}\right] \tag{2.26}$$

The types of non-linear left and right waves are determined by comparing $y_\star$ with the flow depths in the left and right states [$y_{_K}$ $(K = L, R)$]. The left or right wave is a shock if $y_\star > y_{_K}$ $(K = L, R)$, otherwise the wave is a rarefaction wave (smooth wave). When $A_\star$ is less or equal than A_K $(K = L, R)$, it is suggested to replace M_K with the gravity wave celerity c_K $(K = L, R)$ given by Eq. (2.8). The reason is because if the star region and the left and right states are connected by a rarefaction wave, the speeds (of the wave heads) of the left and right rarefaction waves are given respectively by $u_L - c_L$ and $u_R + c_R$ (Toro 2001). Thus, M_K may be expressed as:

$$M_K = \begin{cases} \sqrt{\left(\frac{A_\star \overline{p}_\star}{\rho} - \frac{A_K \overline{p}_K}{\rho}\right)\frac{A_\star}{A_K(A_\star - A_K)}} & \text{if } A_\star > A_K \\ c_K & \text{if } A_\star \leq A_K \end{cases} \tag{2.27}$$

Once the wave speed estimates are computed, the flux at the interface $i + 1/2$ (Eq. 2.18) is fully determined using Eq. (2.2).

2.4 Boundary conditions

In open-channel flows there are three flow regimes, subcritical, critical and supercritical, which have their counterparts in compressible flow, namely, subsonic, sonic and supersonic. In subcritical flows, small disturbances propagate upstream and downstream of the location of the perturbation, whereas in supercritical flows, small disturbances only can travel downstream. Thus, it is apparent that if the flow entering the domain is supercritical, two boundary conditions are needed, and if it is leaving the domain, no boundary condition is needed. Likewise, in subcritical flows, if the flow is entering or leaving the domain, only one boundary condition is needed. For instance, in subcritical regime, if a hydrograph ($Q\ vs\ t$) is to be prescribed at a boundary, the missing variable may be computed from the generalized Riemann invariants. For the left-hand boundary (interface $i = 1/2$), the generalized Riemann invariants across the wave $dx/dt = u + c$ (Eq. 2.14), or which is the same along the wave $dx/dt = u - c$ (negative characteristic c^-) yield:

$$\frac{Q_{1/2}^{n+1}}{A_{1/2}^{n+1}} - \phi_{1/2}^{n+1} = \frac{Q_1^n}{A_1^n} - \phi_1^n \tag{2.28}$$

For a general cross section channel, ϕ can be determined approximately by integrating c/A between two successive values of A using any integration technique. Since $A_{1/2}^{n+1}$ and $\phi_{1/2}^{n+1}$ are related, Eq. (2.28) can be solved for $A_{1/2}^{n+1}$. In the case of a circular cross-section channel, $A_{1/2}^{n+1}$ and $\phi_{1/2}^{n+1}$ are functions of the unknown variable θ, and Eq. (2.28) can be solved for θ by iteration (three or four iterations is usually enough to ensure convergence). The CPU time consumed by this iteration process represents only a very small fraction of the total CPU time. Knowing θ and consequently $A_{1/2}^{n+1}$ and the prescribed variable $Q_{1/2}^{n+1}$, the flux vector $\mathbf{F}_{1/2}^{n+1}$ at the boundary and at the time level $n+1$ can be computed using Eq. (2.2). Similarly, for the right-hand boundary (interface $i = N + 1/2$), the generalized Riemann invariants across the wave $dx/dt = u - c$ (Eq. 2.13), or which is the same along the wave $dx/dt = u + c$ (positive characteristic c^+) yield:

$$\frac{Q_{N+1/2}^{n+1}}{A_{N+1/2}^{n+1}} + \phi_{N+1/2}^{n+1} = \frac{Q_N^n}{A_N^n} + \phi_N^n \tag{2.29}$$

When using higher-order schemes, for the quality of the numerical solution to be preserved it is necessary to use a higher-order reconstruction in all the cells. Since common procedures of reconstruction such as MUSCL use one or more cell on each side of the cell to be reconstructed, generally one or more cells are missing within the first and last cells of the computational domain. Typical procedures to handle this problem are based on the implementation of ghost cells outside of the boundaries (see Chapter 3).

2.5 Incorporation of source terms

Similar to Zhao and Ghidaoui (2004), the source terms $\mathbf{S}$ are introduced into the solution through time splitting using a second-order Runge-Kutta discretization which results in the following explicit procedure.
First step (pure advection):

$$\mathbf{U}_i^{n+1} = \mathbf{U}_i^n - \frac{\Delta t}{\Delta x}(\mathbf{F}_{i+1/2}^n - \mathbf{F}_{i-1/2}^n) \tag{2.30}$$

Second step (update with source term by $\Delta t/2$):

$$\overline{\mathbf{U}}_i^{n+1} = \mathbf{U}_i^{n+1} + \frac{\Delta t}{2}\mathbf{S}\big(\mathbf{U}_i^{n+1}\big) \tag{2.31}$$

Last step (re-update with source term by Δt):

$$\overline{\overline{\mathbf{U}}}_i^{n+1} = \mathbf{U}_i^{n+1} + \Delta t\mathbf{S}\big(\overline{\mathbf{U}}_i^{n+1}\big) \tag{2.32}$$

The evaluation of the source terms $\mathbf{S}$ appearing on Eq. (2.2) requires the definition of the grid bottom slope $(S_0)_i$ given by

$$(S_0)_i = -\frac{z_{i+1/2} - z_{i-1/2}}{x_{i+1/2} - x_{i-1/2}} = -\frac{\Delta z_i}{\Delta x_i} \tag{2.33}$$

and the grid energy line slope $(S_f)_i$ which may be obtained from Manning's equation,

$$(S_f)_i = \frac{n_m^2}{{k_n}^2}\frac{\frac{Q_i}{A_i}\left|\frac{Q_i}{A_i}\right|}{R_i^{4/3}} \tag{2.34}$$

where k_n is 1.0 in Metric units and 1.49 in English units, R is the hydraulic radius and n_m is the so-called Manning roughness coefficient.

2.6 Stability constraints

Since the explicit second-order Runge-Kutta discretization has been used for the incorporation of $\mathbf{S}$ into the solution, the stability constraint must include not only the Courant-Friedrichs-Lewy (CFL) criterion for the convective part, but also the constraint for the source terms. The CFL constraint is given by:

$$Cr_{max} = \frac{\Delta t}{\Delta x_i} \text{ Max }_{i=1,2,\ldots N} \left(|u_i^n| + |c_i^n|\right) \leq 1 \tag{2.35}$$

where Cr_{max} is the maximum Courant number at time level n. From Eq. (2.35), the permissible time step for the convective part is given by:

$$\Delta t_{\text{max, CFL}} = \text{Min }_{i=1,2,\ldots N} \left[\frac{\Delta x_i}{|u_i^n| + |c_i^n|}\right] \tag{2.36}$$

The explicit second-order Runge-Kutta procedure involves two discretizations, which are stated by Eqs. (2.31) and (2.32). Eq. (2.31) is subject to the following stability constraint:

$$-1 \leq \frac{\overline{\mathbf{U}}_i^{n+1}}{\mathbf{U}_i^{n+1}} \leq 1 \tag{2.37}$$

Substituting Eq. (2.31) in Eq. (2.37), and due to the fact that the time step is always positive, the following relations are obtained:

$$\begin{gathered} \frac{\mathbf{S}(\mathbf{U}_i^{n+1})}{\mathbf{U}_i^{n+1}} \leq 0 \\ \frac{\mathbf{S}(\mathbf{U}_i^{n+1})}{\mathbf{U}_i^{n+1}} \Delta t \geq -4 \end{gathered} \tag{2.38}$$

The first inequality in Eq. (2.38) indicates that, for the solution to be stable, the source term $\mathbf{S}$ must be of opposite sign to the variable $\mathbf{U}$. From the second inequality and taking into consideration the first inequality, the following constraint is obtained:

$$\Delta t \leq -4 \frac{\mathbf{U}_i^{n+1}}{\mathbf{S}(\mathbf{U}_i^{n+1})} \tag{2.39}$$

Similarly, due to the explicit discretization in Eq. (2.32), the following stability constraint is obtained:

$$\Delta t \leq -2\frac{\mathbf{U}_i^{n+1}}{\mathbf{S}(\overline{\mathbf{U}}_i^{n+1})} \tag{2.40}$$

Thus, the permissible time step for the source term ($\Delta t_{max,\mathbf{S}}$) is given by:

$$\Delta t_{max,\mathbf{S}} = \text{Min}_{\ i=1,2,\ldots N}\left[-4\frac{\mathbf{U}_i^{n+1}}{\mathbf{S}(\mathbf{U}_i^{n+1})}, -2\frac{\mathbf{U}_i^{n+1}}{\mathbf{S}(\overline{\mathbf{U}}_i^{n+1})}\right] \tag{2.41}$$

Since the same time step Δt must be used for the convective part and the source term, $\mathbf{U}_i^n$ must be used instead of $\mathbf{U}_i^{n+1}$. Finally, the maximum permissible time step including the convective part and the source term will be given by:

$$\Delta t_{max} = \text{Min}_{\ i=1,2,\ldots N}\left[\Delta t_{max,\mathbf{S}},\ \ \Delta t_{\text{max, CFL}}\right] \tag{2.42}$$

2.7 Evaluation of finite volume Godunov type schemes

The purpose of this section is to test the accuracy and efficiency of the two GTS schemes using problems whose solution contain features that are relevant to transient flows in sewers such as shock, expansion and roll waves.

The performance of the GTS methods are evaluated by comparing them to the "Exact" solutions (available only for idealized conditions [e.g., frictionless and horizontal pipes]), "Near exact" solutions, the fixed-grid MOC scheme with space-line interpolation and experimental observations. The "Exact" solution is obtained - at the precision of the computer - with a program written to solve the general Riemann problem for the shallow water equations in circular conduits. The "Near exact" solution is obtained by grid refinement until convergence is achieved. Five tests cases are considered in this section. These are:

1. Hydraulic bores.
2. Comparison of accuracy and efficiency among GTS and MOC schemes without friction.
3. Comparison of accuracy and efficiency among GTS and MOC schemes in presence of friction.
4. Formation of roll waves.
5. Hydraulic routing.

In the following sections, for convenience, the maximum Courant number Cr_{max} is denoted by Cr. In addition, the grid size, Courant number, Manning roughness coefficient and channel slope used in each example are indicated in the relevant figures and thus will not be repeated in the text. Furthermore, the CPU times that are reported in this chapter were averaged over three realizations and computed using a Pentium IV 3.20 GHz personal computer.

2.7.1 Hydraulic bores

The purpose of this test is to demonstrate the capability of the GTS schemes in capturing accurately discontinuities such as hydraulic bores. Hydraulic bores often occur in sewers, particularly after an abrupt change in flow depth or discharge, such as the sudden closure of a downstream gate.

A uniform flow in a 1000 m long frictionless horizontal sewer with a diameter of 2.5 m is considered as the test problem. The initial condition of this problem involves a uniform flow depth ($y = 0.5$ m) and discharge ($Q = 2\ m^3/s$). At time $t = 0$, the supercritical flow is completely blocked at the downstream end of the sewer (e.g., sudden closure of a downstream gate) which generates a bore that travels upstream. The simulation results for the water depth profile at $t = 300\ s$ are shown in Fig. 2.4. The results show that the moving hydraulic bore is well resolved by both GTS schemes. Furthermore, the execution time of both methods is very similar (0.358 s and 0.353 s for the HLL and Guinot Riemann solvers respectively). The maximum Courant number used in the simulations was 0.3. This Courant number may seem small for practical applications, however it must be recalled that the gravity wave celerity is a function of the water depth which may change dramatically in most of the applications (e.g., from dry-bed conditions to near-full pipe), resulting in small Courant numbers for some portions of the system. Furthermore, this thesis is focused on mixed flows in which the celerity in pressurized flows may be two orders of magnitude greater than the gravity wave celerity, resulting in very low Courant numbers for free surface flows.

2.7.2 Comparison of accuracy and efficiency among GTS and MOC schemes without friction

This test is used to compare the accuracy and numerical efficiency of the two GTS schemes and the MOC with space-line interpolation without friction. For a given grid size and Courant number, one scheme can be more accurate than another one, but not necessarily more efficient numerically. A comparison of numerical efficiency requires measuring the CPU time needed by each of the

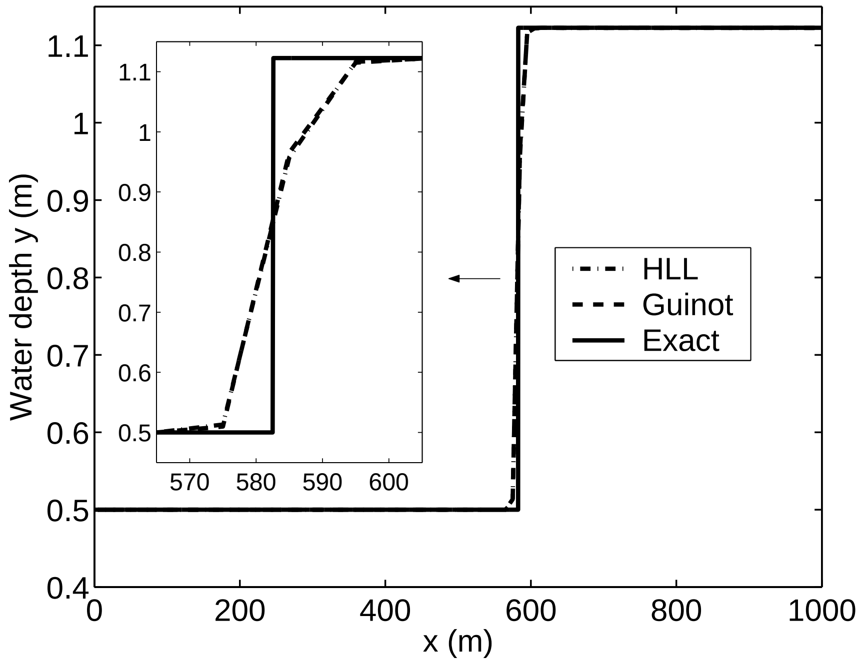

Figure 2.4: Water depth profile of a hydraulic bore in a sewer generated by complete blockage of the flow at sewer's downstream end ($\Delta x = 10$ m, $Cr = 0.3$, $t = 300$ s, $S_f = 0$, $S_0 = 0$).

schemes to achieve the same level of accuracy (e.g., Zhao and Ghidaoui 2004). The numerical efficiency of a model is a critical factor for real-time control, since small simulation time steps and a large number of grids are needed to reasonably reproduce the formation and propagation of hydraulic transients in sewer systems.

The test simulates the sudden opening of a gate separating two pools of still water with different depths mid-way in a 1000 m long frictionless horizontal sewer with a diameter of 15 m. Zero water flux boundary conditions are used in the analysis, namely $Q\ (0,t) = 0$ and $Q\ (1000,t) = 0$. The initial conditions are:

$$\begin{cases} y = 10.0\ m \ \text{ and } u = 0.0\ m/s \text{ for } x <= 500\ m \\ y = 3.0\ m \ \text{ and } u = 0.0\ m/s \text{ for } x > 500\ m \end{cases}$$

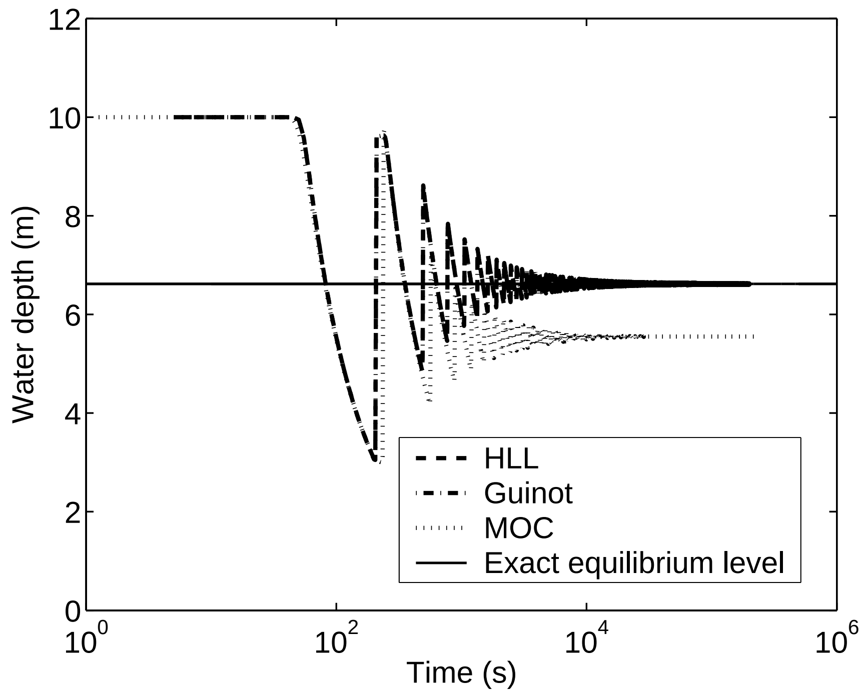

Figure 2.5: Water depth versus time at $x = 2.5$ m for test No. 2 ($\Delta x = 5.0$ m, $Cr = 0.3$, $S_f = 0$, $S_0 = 0$).

The ability of the schemes to conserve mass is first tested. Since zero water flux boundary conditions are used in the current test case, the total mass in the sewer is invariant with time. The simulation results for the water depth versus time at $x = 2.5$ m and the mass traces are shown in Figs. 2.5 and 2.6, respectively. The results show that unlike the MOC scheme, the two GTS schemes conserve mass. For instance, Fig. 2.6 shows that after 400 seconds of simulation, about 20% of the initial total water volume is lost by the MOC scheme and none by the two GTS schemes.

Next, the influence of the Courant number on the accuracy of the schemes before and after the shock and rarefaction waves have interacted with the zero water flux boundaries is investigated. The simulations results are shown in Figs. 2.7, 2.8 and 2.9. The results show that for the same Courant number, the numerical dissipation exhibited by the two GTS schemes is significantly

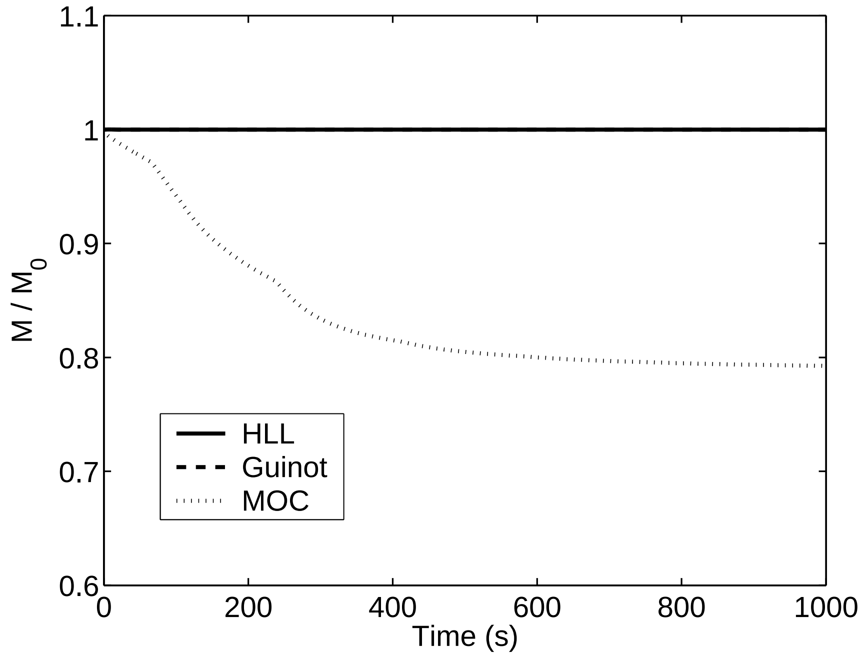

Figure 2.6: Mass traces for test No. 2 ($\Delta x = 5.0$ m, $Cr = 0.3$, $S_f = 0$, $S_0 = 0$).

smaller than that produced by the MOC scheme. Furthermore, unlike the MOC scheme, the two GTS schemes preserve their resolution for decreasing Courant number. The results also show that the jump simulated by the MOC scheme moves slower than the actual jump. The accurate prediction of the speed of jumps in sewer systems is very important because it dictates the timing at which surcharging occurs.

A quantitative measure of the numerical dissipation can be obtained by using the integral form of the energy equation (Ghidaoui and Cheng 1997). The absence of friction and gravity forces (recall that in this test case the sewer is assumed to be frictionless and horizontal) and the invariance of the total mass in the sewer with time imply that the total energy is conserved throughout the transient. Therefore, any dissipation found in the results is solely due to numerical dissipation. Fig. 2.10 shows the relative energy traces E_t/E_0 for different Courant numbers. This figure demonstrates that unlike the

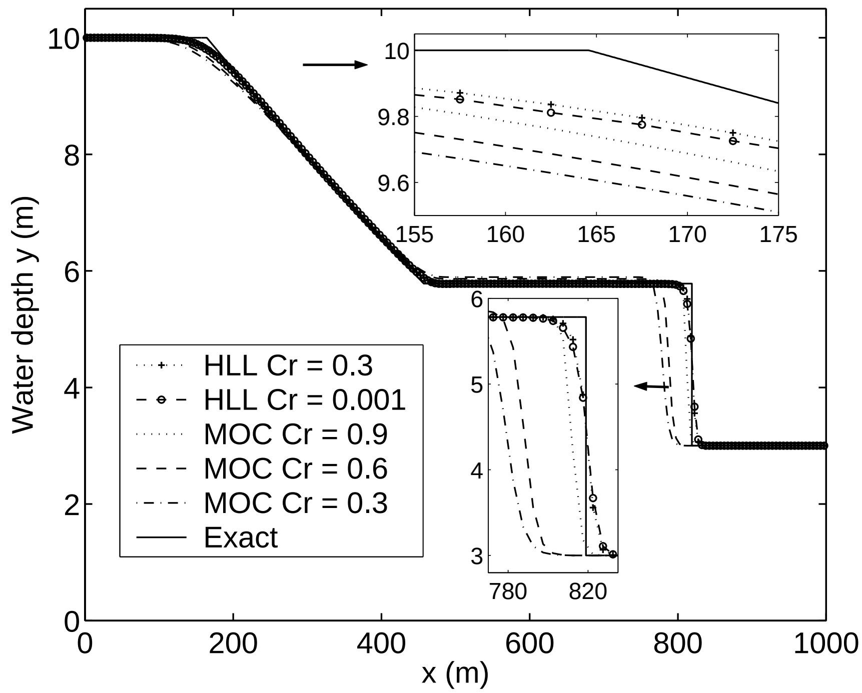

Figure 2.7: Water depth profile for test No. 2 before the shock and rarefaction waves have interacted with the zero water flux boundaries for HLL Riemann solver ($\Delta x = 5.0$ m, $t = 36$ s, $S_f = 0$, $S_0 = 0$).

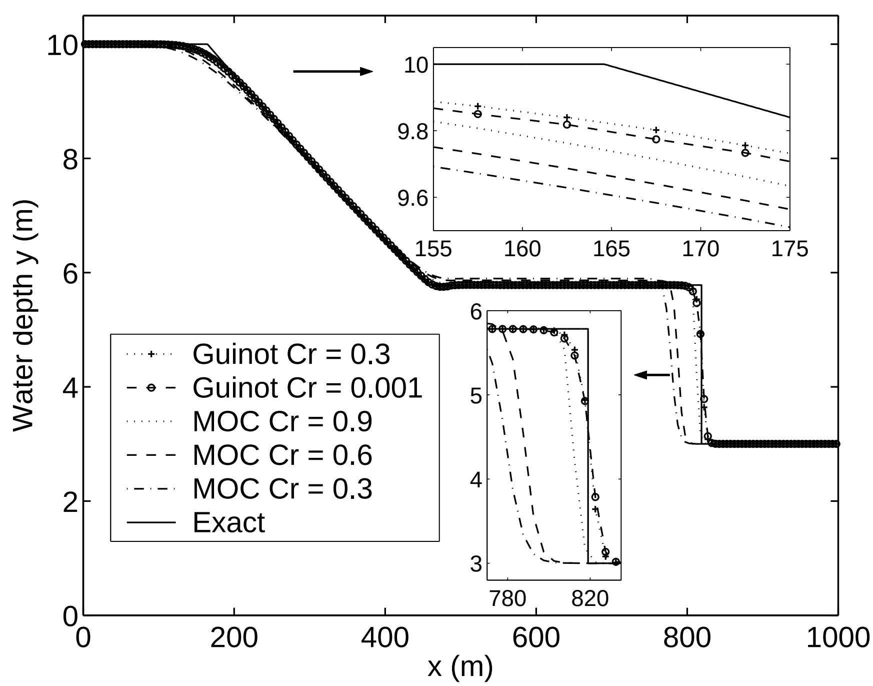

Figure 2.8: Water depth profile for test No. 2 before the shock and rarefaction waves have interacted with the zero water flux boundaries for Guinot Riemann solver ($\Delta x = 5.0$ m, $t = 36$ s, $S_f = 0$, $S_0 = 0$).

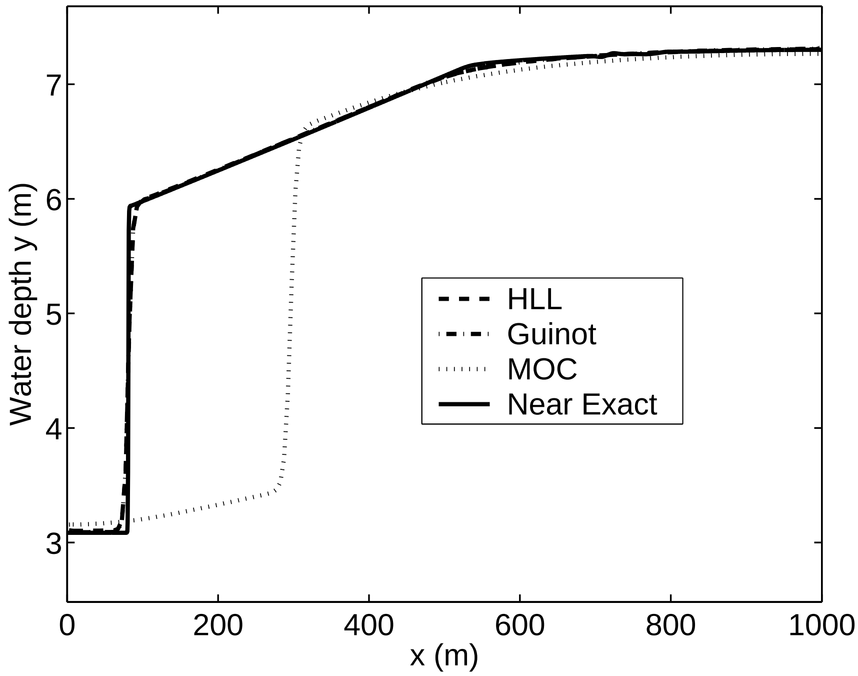

Figure 2.9: Water depth profile for test No. 2 after the shock and rarefaction waves have interacted with the zero water flux boundaries (Δx = 5.0 m, Cr = 0.3, t = 197 s, S_f = 0, S_0 = 0).

MOC scheme, the numerical dissipation exhibited by the two GTS schemes is not sensitive to the Courant number. This figure also shows that for a given Courant number, the numerical dissipation produced by the two GTS schemes is significantly smaller than that obtained by the MOC scheme. For instance, when $Cr = 0.3$, after 400 seconds of simulation, more than 40% of the initial total energy is dissipated by the MOC approach and only about 20% by both GTS schemes.

To this point, it is shown that for the same grid size and for the same Courant number, the two GTS schemes are more accurate than the MOC scheme with space-line interpolation. However, as pointed out by Zhao and Ghidaoui (2004), a comparison of numerical efficiency requires measuring the CPU time needed by each of the schemes to achieve the same level of accuracy.

To compare the efficiency of these schemes, before and after the shock

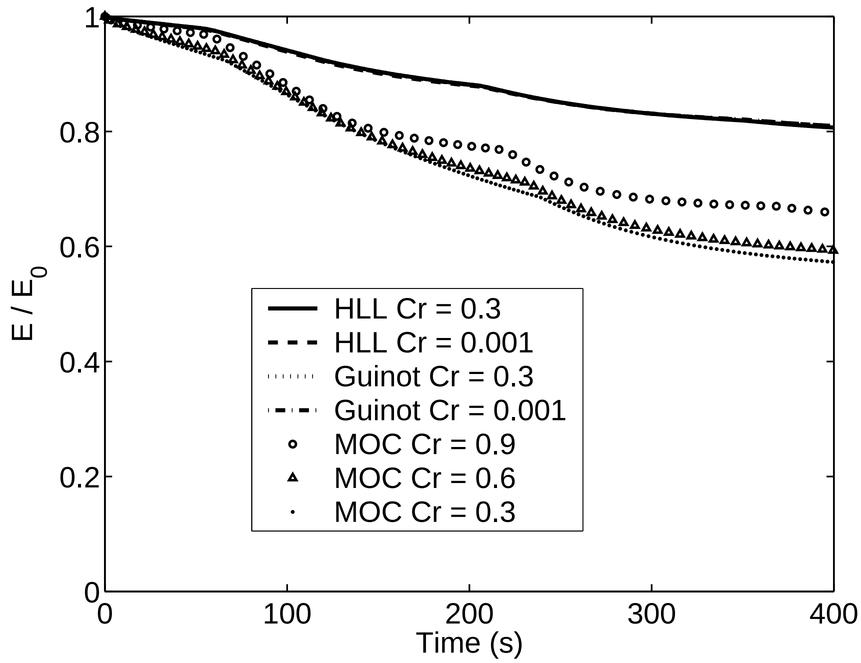

Figure 2.10: Energy traces for test No. 2 ($\Delta x = 5.0$ m, $S_f = 0$, $S_0 = 0$).

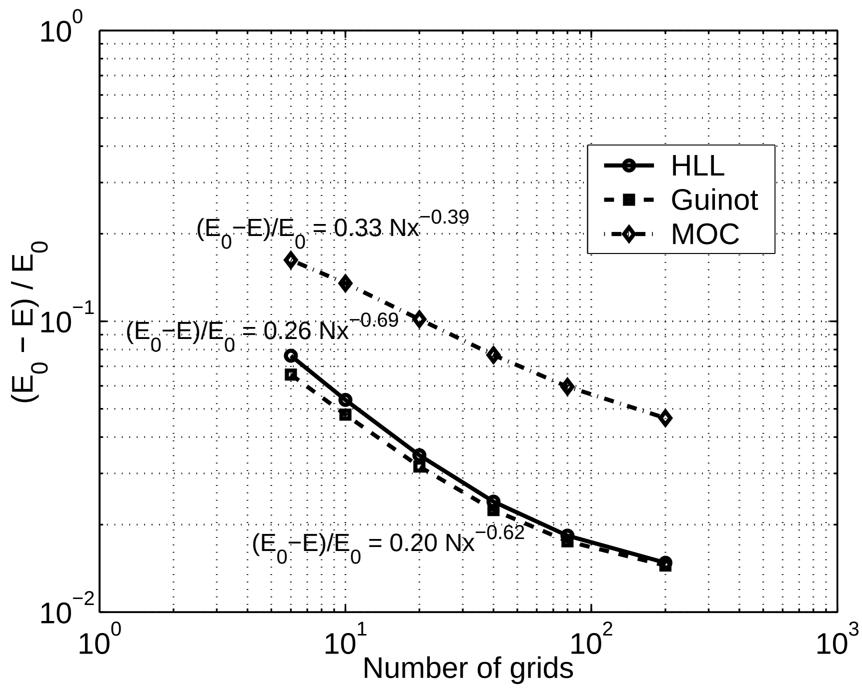

Figure 2.11: Relation between numerical dissipation and number of grids for test No. 2 before the shock and rarefaction waves have interacted with the zero water flux boundaries ($Cr = 0.3$, $t = 36$ s, $S_f = 0$, $S_0 = 0$).

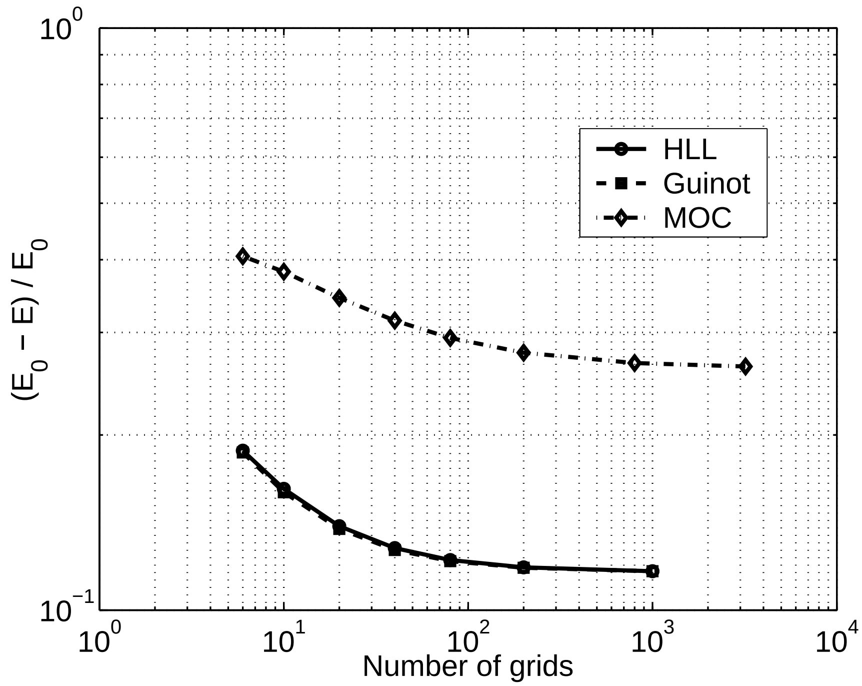

Figure 2.12: Relation between numerical dissipation and number of grids for test No. 2 after one wave cycle ($Cr = 0.3$, $t = 200$ s, $S_f = 0$, $S_0 = 0$).

and rarefaction waves have interacted with the boundaries (first interaction with the boundaries occurs at about 50 s), the numerical dissipation is plotted against the number of grids on log-log scale and shown in Figs. 2.11 and 2.12. Fig. 2.11 (before the shock and rarefaction waves have interacted with the boundaries) shows that the reduction in numerical dissipation when the number of grids is increased is approximately linear (on log log scale). However, when convergence is close to being achieved, the reduction of the numerical dissipation asymptotically tends to zero. In real-time simulations (due to the computational cost), the accuracy pursued in the numerical modeling will typically fall in the linear portion of Fig. 2.11. Hence, the linear relationships are used for the comparison of numerical efficiency. These linear relationships were fitted to power functions whose equations are given in Fig. 2.11. These equations were used to compute the number of grids needed by each of the schemes to achieve a given level of accuracy. These in turn were used to compute the CPU times. Accurate estimate of CPU times requires that our model is run for a sufficiently long simulation time. When using 50 seconds simulation time, the CPU time for the GTS schemes is in the order of 10^{-2} seconds. This CPU time is clearly too small to be reliable because the time allocated to uncontrolled processes during the simulation can have a significant impact on small CPU times. Therefore, the simulation time was increased to 10000 seconds, which results in CPU times that are in the order of 1 second. The results for the CPU times for the extended simulation time are presented in Table 2.1. It is noted that several interactions between the waves and the boundaries occurs during the extended simulation time. The tasks executed at a boundary node are similar to those executed at an internal node (i.e., the efficiency of the scheme is not altered by the interactions at the boundaries). Therefore, the extrapolation remains valid as long as the tasks executed at the boundaries are the same as those at the internal nodes. Notice in Table 2.1 that the two GTS schemes have similar efficiency. Also note that to achieve the same degree of accuracy, the MOC approach requires a much finer grid size than the two GTS methods. In addition, this table shows that to achieve the specified level of accuracy, the two GTS schemes are about 100 to 300 times faster to execute than the MOC approach.

The results after one wave cycle (Fig. 2.12) show that the accuracy produced by the two GTS schemes cannot be matched by the accuracy of the MOC scheme, even when using a large number of grids. The poor results obtained with the MOC scheme may be explained by recalling that this scheme does not conserve mass. At $t = 0$, the initial total energy (E_0) is only potential. After the flow has reached to a static equilibrium ($t = \infty$), the kinetic energy is zero

Table 2.1: Comparison of efficiency among the two GTS methods and the MOC scheme with space-line interpolation (Cr = 0.3, t = 10000 s, S_f = 0, S_0 = 0) [Nx is number of grids needed to achieve a specified level of accuracy].

Description		HLL	Guinot	MOC
$(E_0 - E)/E_0 = 2\%$	Nx	42	42	1324
	CPU time (s)	2.44	2.55	819.20
$(E_0 - E)/E_0 = 3\%$	Nx	23	22	468
	CPU time (s)	0.83	0.73	104.20

and the total energy is again only potential. If mass is conserved, the potential energy at $t = \infty$ is 77.1 % of E_0, which means that the maximum energy that can be dissipated in the system is 22.9 % of E_0. Any additional energy loss is a result of a numerical loss of mass in the simulation. The inability of the MOC scheme to conserve mass can produce dissipations beyond the maximum energy that can be dissipated (22.9 %), as can be observed in Fig. 2.10. In this figure for instance, when Cr = 0.3, after 400 s of simulation time, the MOC scheme has produced a numerical dissipation of more than 40%, about half of which can be attributed to the numerical loss of water mass (Fig. 2.6).

2.7.3 Comparison of accuracy and efficiency among GTS and MOC schemes in presence of friction

This test is used (1) to investigate and compare the accuracy and efficiency of the two GTS schemes and the MOC method with space-line interpolation in the presence of friction, and (2) to measure the relative magnitude of the numerical and physical dissipation. The parameters for this test case are the same than the previous one except friction is included using a Manning roughness coefficient of 0.015.

Because it is shown that the two GTS schemes have similar accuracy and efficiency, only the GTS scheme with HLL Riemann solver is considered in this test case. Since the energy dissipation in this case is only due to friction (E_f), the total energy (E) after a given period can be obtained by subtracting E_f attained during that period from the initial energy (E_0). E_f may be obtained by integration of the net work done by the force of friction over a given period.

The simulation results for the relative energy traces (E/E_0) for different numbers of grids and Courant numbers is presented in Fig. 2.13. The results for the GTS scheme show that for the same Courant number (e.g., $Cr = 0.3$), the numerical dissipation is reduced when the number of grids is increased (e.g., 200 instead of 40). Regarding the influence of the Courant number in the solution, it was pointed out previously that the two GTS schemes are not too sensitive to this parameter.

To determine if the dissipation produced by the GTS scheme is only physical, the traces of E/E_0 are compared with the trace of 1 - E_f/E_0 obtained with the HLL scheme using $Cr = 0.9$ and $Nx = 8000$. A maximum Courant number of 0.9 instead of 1.0 is used because when using an explicit scheme (as used here), the norm of the wave propagation velocity with respect to a fixed observer on the pipe ($|u \pm c|$) at time $t + 1$ may be greater than that at time t, resulting in a greater Cr at time $t+1$ compared to time t. Hence, if a Cr equal to one is used, numerical instabilities may be encountered during the simulations. The Courant number specified in the simulations is the maximum, which means only one or few cells will satisfy the specified maximum Courant number. Since only one or in the best of the cases few cells will achieve a

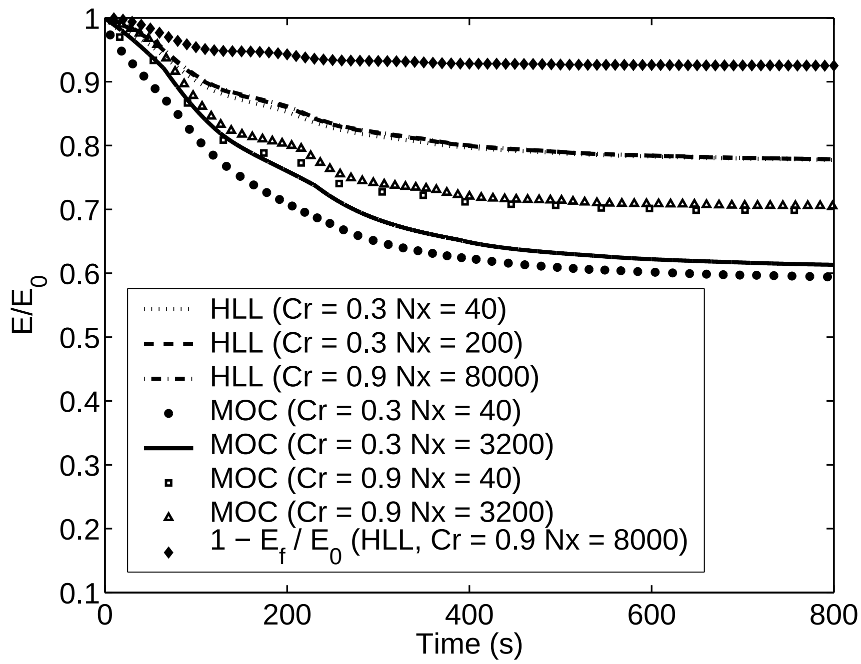

Figure 2.13: Energy traces for test No. 3 ($n_m = 0.015$, $S_0 = 0$).

Courant number equal or close to one, an exact solution can not be achieved numerically in free surface flows. Thus, the trace of 1 - E_f/E_0 (Fig. 2.13) is not exact but approximate and it contains some numerical dissipation. However, given the large number of cells used, it is expected that the trace of 1 - E_f/E_0 be close to the exact solution.

To have an idea about the ratio between physical and numerical dissipation for the given conditions, the traces of E/E_0 and 1 - E_f/E_0 after 400 s of simulation time is considered. At this time, the computed values of E/E_0 and 1 - E_f/E_0 are approximately 0.80 and 0.93, which means that the total energy dissipation in this example is 20% of the initial energy (E_0). However, the actual physical dissipation is about 7% of the initial energy and consequently the numerical dissipation is about 13%. In this case, to reduce the numerical dissipation, a maximum Courant number close to one and a large number of cells must be used.

In the case of the MOC scheme, the results show that for the same number of grids, the dissipation produced is highly dependent on the Courant number. When using a larger number of grids, the numerical dissipation is reduced but not enough to overcome the effect of a small Courant number. The results also show that after the first quarter wave cycle (about 50 s), the accuracy produced by the GTS scheme cannot be matched by the accuracy of the MOC scheme, even when using a Courant number close to one and a large number of grids. In this case, the physical dissipation is totally overwhelmed by the numerical dissipation. The reasons for the poor results obtained with the MOC scheme are similar to those discussed in the previous section.

2.7.4 Formation of roll waves

The purpose of this test is to demonstrate the ability of the GTS schemes to predict the formation of roll waves. The ability of a model to predict the formation and amplitude of roll waves is important because these waves constitute one of the instabilities that could lead to sewer surcharging. This instability is related to the friction in the channel bed and is caused mainly by the water moving considerably faster near the free surface than near the bed. Surcharging may occur when the amplitude of these waves is large enough to reach the sewer crown. Even when the amplitude of the roll waves is not high enough to reach the sewer crown, these waves may interact with the air in the gap between the water surface and sewer crown, leading to open channel-pressurized flow instability, which causes surcharging (Ghidaoui 2004).

Linear stability analysis applied to uniform base flow in a very wide channel has shown that the formation of roll waves starts to occur when the Froude number (F) is above 1.5 for the case of the Manning resistance formula. For circular channels this stability critical value is usually greater than 2.0 because of the sidewall effect (Yen 2001).

In a similar way to Zanuttigh and Lamberti (2002), to demonstrate the ability of the GTS schemes to predict the formation of roll waves, the evolution of the periodic perturbation $y' = 0.005\, sin\, (\pi t/2)$ imposed upstream ($x = 0$) over a uniform flow depth y_0 is analyzed. Because it is shown that the two GTS schemes have similar accuracy and efficiency, only the GTS scheme with HLL Riemann solver is considered in this test case. A code developed using the aforementioned GTS scheme was applied to verify if the perturbation is amplified for F higher than about 2.0 and attenuated otherwise. A 500 m long sewer with a diameter of 4 m is considered in the analysis. The range of flows used in the simulations is characterized by Froude numbers between 2.02 and 3.96 and a constant uniform flow depth $y_0 = 1$ m. The wall shear stress is represented using the Manning's equation with a coefficient equal to 0.015, constant along the channel. Since the flow is supercritical, two upstream boundary conditions are required. The first boundary condition is a periodic flow depth $(y_0 + y')$ and the second one is a steady discharge which is computed with the uniform flow parameters. Due to the type of flow regime, at the downstream end a non-reflective boundary condition is specified to avoid backward reflections into the domain.

The simulation results for the flow depth versus time at the downstream end of the channel ($x = 500$ m) together with the initial perturbation imposed upstream ($x = 0$ m) are presented in Fig. 2.14. This figure, although it does not present characteristics of roll waves (non-symmetric waves with steep fronts), shows that the perturbation is amplified for F higher than about 2.65 and attenuated otherwise. When different periodic perturbations were imposed

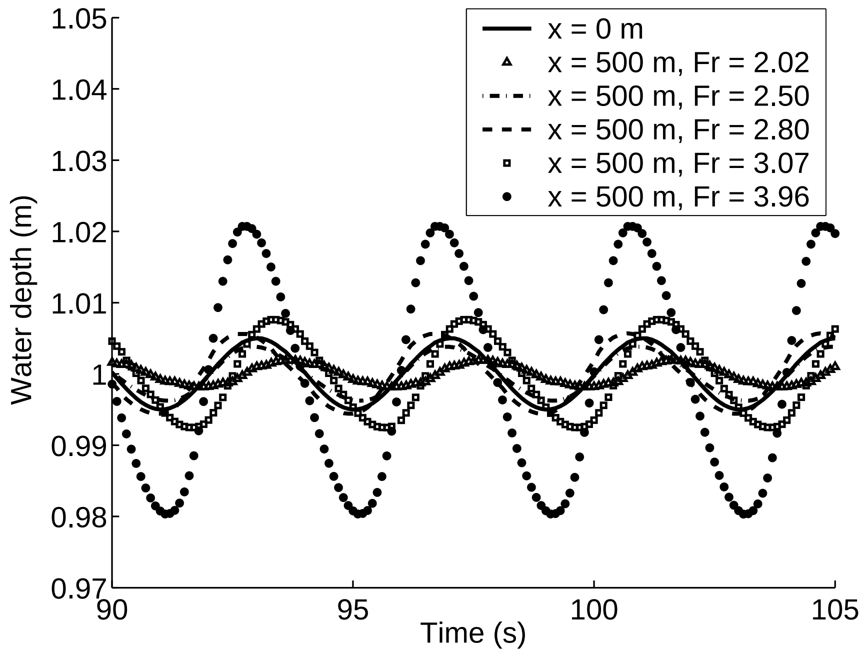

Figure 2.14: Flow depth versus time at downstream end of sewer ($x = 500$ m) for different Froude numbers together with the perturbation at sewer inlet ($x = 0$ m) [$\Delta x = 0.05$ m, $Cr = 0.8$, $n_m = 0.015$].

upstream ($x = 0$), the Froude numbers that dictated whether these perturbations were attenuated or amplified were no longer 2.65, but remained between 2.0 and 3.0. For the tested periodic perturbations, roll waves did not fully develop. A much longer channel (pipe) was needed for the full development of this type of waves. This is due to the fact that roll waves are induced by advective-type instability, where the instabilities grow spatially.

The correct development of the roll waves requires that the frequency of the forcing function at the upstream end be similar to the one for which the flow is least stable. The least stable mode is obtainable from linear stability theory. Such data is not available in this case and it appears that the value of frequency chosen here may not be representative of the least stable mode. One way to deal with this issue is to use a random perturbation. Random forcing at the upstream end subjects the flow to a wide range of perturbation frequencies.

The least stable mode grows rapidly with distance downstream and quickly becomes the dominant frequency of the flow and controls the behavior of the roll waves. Random perturbations are investigated below.

The random perturbation used in the analysis is $y' = 0.01 * ran$, where ran is a random number within the range $0 \leq x \leq 1$ generated at every time step. The simulation results for the flow depth versus the longitudinal distance (x) as well as the parameters used in this new simulation are presented in Fig. 2.15. The water waves shown in this figure present the typical characteristics of roll waves. However, the amplitude and speed of these waves may not be accurately predicted because of the assumptions inherent in the shallow water equations. Recall that the shallow water equations assume that the pressure is hydrostatic, the momentum correction coefficient is equal to one and the wall shear stress during unsteady flow conditions is given by relations that are derived for steady flow conditions. These assumptions are questionable in roll wave flows, where the fluid particles experience significant vertical motion and the velocity profile is far from the steady logarithmic profile. Experimental and theoretical work is required to investigate the importance of the assumptions inherent in the shallow water equations (Ghidaoui 2004).

2.7.5 Hydraulic routing

Most practical engineering problems of unsteady open-channel flows involve hydraulic routing. For instance, hydraulic routing simulations are used for determining the attenuation and translation of a flood hydrograph through a stream reach. Given the importance of hydraulic routing in unsteady open-channel flow problems, the purpose of this section is to evaluate the performance of the two GTS schemes in solving hydraulic routing problems by

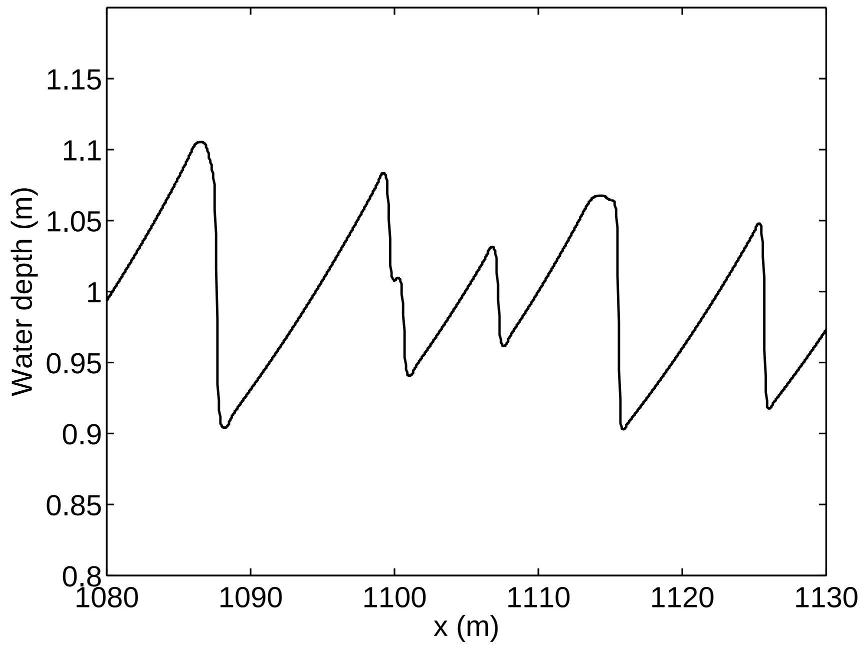

Figure 2.15: Water depth profile showing typical characteristics of roll waves. [$d = 4$ m, $l = 1200$ m, $\Delta x = 0.04$ m, $Cr = 0.8$, $t = 150$ s, $n_m = 0.015$, $S_0 = 0.10$].

comparing the results of the simulations obtained with these methods and experimental observations.

One of the sets of experiments conducted at the Wallingford Hydraulics Research Station (WHRS) in England by Ackers and Harrison in 1964 is considered as the test case. The unsteady flow experiments were performed by introducing prescribed flow hydrographs at the sewer's upstream end after running a steady flow for a period. At the sewer's downstream end, a free overfall was placed to enforce a critical flow at this location. Water stages were measured over time at several locations along the channel. The original data were reported in a paper by Ackers and Harrison (1964) and have been partially reproduced in a number of sources such as Franz and Melching (1997). The Ackers and Harrison paper does not report the values of the experimental data, but includes plots showing scaled data (data collected in

Table 2.2: Hydraulic characteristics of the scaled-up data from Ackers and Harrison (1964). Used with permission from Institution of Civil Engineers, London.

Sewer & inflow characteristics and units	**Scaled-up data values**
Length (m)	304.8000
Diameter (m)	0.3048
Bed slope	0.0010
Roughness height (cm)	0.06096
Manning's n_m (peak flow)	0.0116
Manning's n_m (base flow)	0.0115
Base flow (m^3/s)	0.004984
Peak inflow (m^3/s)	0.018689
Base flow depth (m)	0.0768
Inflow duration (s)	132
Shape of inflow hydrograph	symmetric trapezoid
Duration of peak inflow (s)	12

0.25-ft diameter pipe and scaled up to 1-ft diameter pipe by Froude criterion). Since the original experimental data were not available, the scaled up stage hydrograph is used for comparison here.

The scaled-up data reproduced in Table 2.2 is routed using both GTS methods. The simulated stage hydrographs are contrasted with the reported scaled experimental observations in Fig. 2.16. As shown in this figure, the performance of both GTS schemes is very similar for all the simulated cases. Furthermore, the execution time of both methods is very similar (8.86 s and 8.72 s for the HLL and Guinot Riemann solvers respectively). In addition,

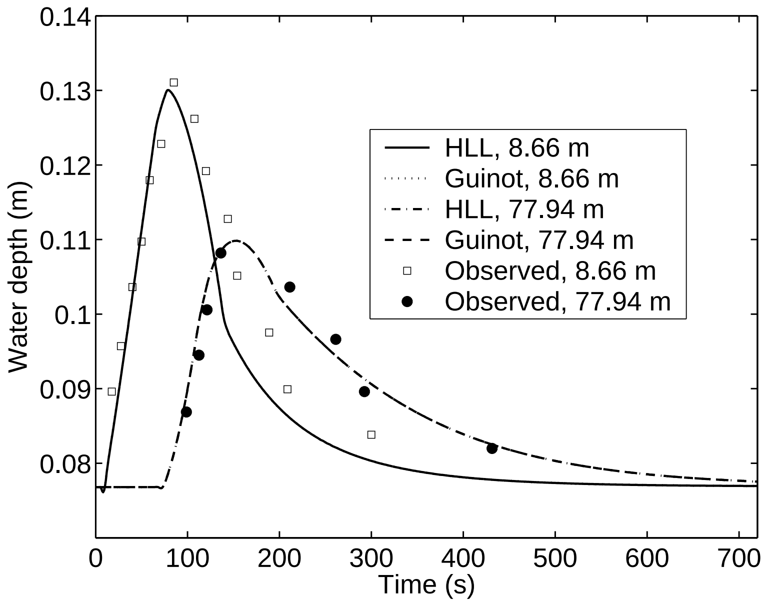

Figure 2.16: Simulated and observed water depths at $x = 8.66$ m and 77.94 m for scaled sewer pipe ($\Delta x = 1.016$ m, $Cr = 0.3$, $S_0 = 0.001$ and $n_m = 0.0116$) [Experimental data used with permission from Institution of Civil Engineers, London].

the results show that the stage hydrograph at $x = 77.94$ m from the upstream end seems to be equally well simulated by both GTS schemes. However at $x = 8.66$ m from the upstream end, the dispersion shown by the observed stage hydrograph is clearly larger than predicted by both GTS methods, which is specially noticeable on the receding portion of the hydrograph. Franz and Melching (1997) using the so called Full Equations (FEQ) model obtained very similar results to those obtained using the two GTS schemes. They suggest that the discrepancies between simulated and observed values may be due to possible scaling problems and due to the fact that some of the experiments done by Ackers and Harrison included flows in the transition region between laminar and fully turbulent flow, which causes that the roughness coefficient be a function of the Reynolds number.

Chapter 3

Pressurized flows

3.1 Introduction

Most liquids flowing in pipelines contain dissolved gases in solution that may include free gas, although the volumetric proportion may be very small. In absence of free air or vapor in a liquid piping system, the pressure wave speed remains constant. The existence of even a very small fraction of gas dispersed throughout the liquid in the pipeline can greatly reduce the propagation speed of the pressure wave (e.g., Wylie and Streeter 1993). When the amount of gas in the conduit is small ($<\approx 1\%$ in volume), the gas-liquid mixture (two-phase) flow can be treated in a similar way to that of a single-phase flow (pure liquid) using the single-equivalent fluid approximation. In this chapter, the same numerical technique is proposed to solve single-phase and two-phase (using the single-equivalent fluid approximation) flows. Current methods available for modeling these flows (single and two-phase) are briefly described in the following section. These methods were proposed for simulating water hammer flows, however they are valid in general for unsteady pressurized flows.

3.1.1 Methods for single-phase water hammer flows

Among the approaches proposed to solve the single-phase (pure liquid) water hammer equations are the Method of Characteristics (MOC), Finite Differences (FD), Wave Characteristic Method (WCM), Finite Elements (FE), and Finite Volume (FV). In-depth discussions of these methods can be found in Chaudhry and Hussaini (1985), Ghidaoui and Karney (1994), Szymkiewicz and Mitosek (2004), Zhao and Ghidaoui (2004), and Wood et al. (2005). Among these methods, MOC-based schemes are most popular because these schemes provide the desirable attributes of accuracy, numerical efficiency and programming simplicity (e.g., Wylie and Streeter 1993, Zhao and Ghidaoui 2004, Ghidaoui et al. 2005). In fact, in a review of commercially available water hammer software packages, it is found that eleven out of fourteen software packages examined use MOC schemes (Ghidaoui et al. 2005).

As was mentioned above, MOC-based schemes are most popular to simulate single-phase transient flows in pipes. The MOC transforms the partial differential equations of continuity and momentum into a set of ordinary differential equations that are relatively easy to solve. As a result, many methods and strategies have been developed to apply the MOC to one-dimensional flows.

For many years the fixed-grid MOC has been used with good success to simulate transient conditions in pipe systems and networks (Karney and Ghidaoui 1997), however one difficulty that commonly arises relates to the selection of an appropriate level of discretization (or time step) to use for the analysis. The obvious trade-off is between computational speed and accuracy. In general the smaller the time step, the longer the run time but the greater the numerical accuracy.

The challenge of selecting a time step is made difficult in pipeline systems by two conflicting constraints. First, to calculate many boundary conditions, such as obtaining the head and discharge at the junction of two or more pipes, it is necessary that the time step be common to all pipes. The second constraint arises from the nature of the MOC. If the advective terms in the governing equations are neglected (as is almost always justified), the MOC requires that ratio of the distance Δx to the time step Δt be equal to the wave speed in each pipe. In other words, the Courant number should ideally be equal to one and must not exceed one by stability reasons. For most pipeline systems, having as they do a variety of different pipes with a range of wave speeds and lengths, it is impossible to satisfy exactly the Courant requirement in all pipes with a reasonable (and common) value of Δt.

Faced with this challenge, researchers have sought for ways of relaxing the numerical constraints. Two contrasting strategies present themselves. The "method of wave-speed adjustment" changes one of the pipeline properties (usually the wave speed, though more rarely the pipe length is altered) so as to satisfy exactly the Courant condition. Despite the obvious liberties this kind of adjustment takes with the physical problem, this procedure is widely recommended in the pipeline literature (e.g., Wylie and Streeter 1983, Chaudhry 1987). The second alternative is to allow Courant numbers less than one and to interpolate between known grid points. The most common methods include linear interpolation at a fixed time level, including both space-line interpolation and reach-out in space interpolation (Wiggert and Sundquist 1977), as well as interpolation at a fixed location, such as time-line interpolation or reach-back in time interpolation (Goldberg and Wylie 1983). Lai (1989) combined these options to form what he calls multimode scheme. A number of nonlinear interpolation techniques also have been proposed including the Holly-Preissmann scheme (Holly and Preissmann 1977), Holly-Preissmann with time-line interpolation (Liggett and Chen 1994), and a method that uses cubic splines (Sibetheros et al. 1991).

Ghidaoui and Karney (1994) have developed the concept of an equivalent partial differential equation to analyze theoretically the numerical properties of a variety of interpolation schemes. They found that all common interpolation procedures considerably distort the original governing equations and that even interpolation procedures may change the wave speed. Thus, Ghidaoui and Karney (1994) concluded that it is unlikely that any discretization approach would be ideal for all pipeline systems and for all kind of disturbances.

Recently, FV Godunov-Type Schemes (GTS) that belong to the family of shock-capturing schemes have been applied to single-phase water hammer problems with good success. The first application of GTS to single-phase water hammer problems is due to Guinot (2000), who presented first and second-order schemes based on Taylor series expansions of the Riemann invariants. He showed that his second-order scheme is largely superior to his first-order scheme, although the Taylor series development introduces an inevitable inaccuracy in the estimated pressure, especially in the case of low pressure-wave celerities. A second application is due to Hwang and Chung (2002), whose second-order accuracy scheme is based on the conservative form of the compressible flow equations. Although this scheme requires an iterative process to solve the Riemann problem, these authors state that their scheme requires a little more arithmetic operation and CPU time than the so-called Roe's scheme, but is able to get more accurate computational results than the latter scheme. Later, Zhao and Ghidaoui (2004) presented first and second-order schemes for solution of the non-conservative water hammer equations. These authors show that, for a given level of accuracy, their second-order GTS requires much less memory storage and execution time than either their first-order GTS or the fixed-grid MOC scheme with space-line interpolation. It is pointed out that the numerical tests carried out by these authors were for low Courant numbers. When a Courant number very close to 1.0 is used, as shown in the present paper, the MOC scheme can be more efficient than the scheme of Zhao and Ghidaoui.

3.1.2 Methods for two-phase water hammer flows (single equivalent fluid approximation)

The partial differential equations that describe two-phase flows in closed conduits can be simplified to a great extent when the amount of gas in the conduit is small. In this case, the gas-liquid mixture can be treated as a single-equivalent fluid (e.g., Chaudhry et al. 1990, Martin 1993, Wylie and Streeter 1993, Guinot 2001a). The governing equations when using the single-equivalent fluid approximation are identical to those for a single-phase flow. Due to this fact, similar techniques to those for a single-phase flow are used to solve the two-phase flow governing equations based on the single-equivalent fluid concept. However, since shocks may be produced during transient conditions in two-phase flows (e.g., Padmanabhan and Martin 1978), only those methods that can handle shocks without special treatment are suitable for these applications.

In the literature, numerical schemes that have been proposed for modeling one-dimensional two-phase flows using the single-equivalent fluid approximation include MOC schemes, Lax-Wendroff schemes, a plethora of explicit schemes, and implicit methods (e.g., Chaudhry et al. 1990, Martin 1993). The MOC scheme requires isolation of shocks. The Lax-Wendroff scheme has the advantage that shock waves can be handled without special treatment (e.g., Martin 1993). However, the solution produces an overshooting of the shock front, followed by damped oscillations. These oscillations can be eliminated by introducing pseudo-viscosity. Artificial damping may be also necessary when using explicit schemes (e.g., Martin 1993). When using implicit methods, biasing or weighting problems may be encountered (e.g., Martin 1993).

Recently, Guinot (2001a, 2001b) has applied GTS schemes to two-phase flows with good success. The first-order GTS presented by Guinot (2001a) showed that numerical diffusion leads to a very fast degradation of the solution quality after a few oscillation periods. The second-order scheme by Guinot (2001b) is largely superior to his first-order scheme, although an iterative process is required to solve the Riemann problem. Lately, León et al. (2006c) presented a highly efficient GTS scheme for two-phase water hammer flows. In their scheme no iteration is required for the solution of the Riemann problem.

The present chapter focuses on the formulation and numerical efficiency assessment of a second-order accurate FV shock-capturing scheme for simulating one and two-phase water hammer flows. This chapter which is based on León et al. (2006c) is organized as follows: (1) the governing equations are presented in conservation-law form; (2) the corresponding FV discretization is described; (3) a brief description of the proposed second-order scheme for the internal cells is presented; (4) Riemann solvers for the flux computation at the cell interfaces are provided; (5) a brief description for the formulation of second-order boundary conditions is presented; (6) stability constraints for the source term discretized using the second-order Runge-Kutta are formulated; (7) incorporation of the source terms into the solution is briefly described; and (8) results from testing the proposed model under single and two-phase flow conditions are presented.

3.2 Governing equations

The governing equations that describe two-phase flows in closed conduits can be simplified to a great extent when the amount of gas in the conduit is small. In this case, it can be assumed that there is no relative motion or slip between the gas and the liquid and both phases can be treated as a "single-equivalent fluid" with average properties (e.g., Martin 1993, Wylie and Streeter 1993). Furthermore, the characteristic time scale of the transients is so small that adsorption/desorption of gas can be considered negligibly small (Zielke et al. 1989). The mass and momentum conservation equations for the "single-equivalent fluid" assumptions are identical to those for a liquid-phase flow and can be written in their vector conservative form as follows (e.g., Chaudhry 1987, Martin 1993):

$$\frac{\partial \mathbf{U}}{\partial t} + \frac{\partial \mathbf{F}}{\partial x} = \mathbf{S} \tag{3.1}$$

where the vector variable $\mathbf{U}$, the flux vector $\mathbf{F}$ and the source term vector $\mathbf{S}$ may be written as:

$$\mathbf{U} = \begin{bmatrix} \Omega \\ Q_m \end{bmatrix}, \mathbf{F} = \begin{bmatrix} Q_m \\ \frac{Q_m^2}{\Omega} + A_f p \end{bmatrix} \text{ and } \mathbf{S} = \begin{bmatrix} 0 \\ (S_0 - S_f)\rho_f g A_f \end{bmatrix} \tag{3.2}$$

where ρ_f is the fluid density, A_f is the full cross-sectional area of the conduit, $\Omega = \rho_f A_f$ is the mass of fluid per unit length of conduit, $Q_m = \Omega u$ is the mass discharge, u is the water velocity, p is the pressure acting on the center of gravity of A_f, g is the gravitational acceleration, S_0 is the slope of the conduit, and S_f is the slope of the energy line.

The vector Eq. (3.1) does not form a closed system in that the flow state is described using three variables: Ω, p and Q_m. However, it is possible to eliminate the pressure variable by introducing the general definition of the celerity of the pressure wave (a_g) (e.g., Guinot 2003), which relates p and Ω:

$$a_g = \left[\frac{d(A_f p)}{d\Omega}\right]^{1/2} \tag{3.3}$$

The pressure-wave celerity for the gas-liquid mixture (a_m) can be estimated as (Guinot 2001a):

$$a_m = \frac{a}{\sqrt{1 + \psi_{ref}\rho_{f_{ref}} a^2 \frac{p_{ref}^{\frac{1}{\beta}}}{p^{\frac{1+\beta}{\beta}}}}} \tag{3.4}$$

where a is the pressure-wave celerity in presence of liquid only, p_{ref} is a reference pressure for which the density is known ($\rho_{f_{ref}}$), β is a coefficient equal to 1.0 for isothermal processes and 1.4 for adiabatic conditions, and ψ_{ref} is the volume fraction of gas at the reference pressure. The water density measured at a temperature of 4 degrees Celsius under atmospheric pressure conditions is 1000 kg/m^3. Thus, the reference density and pressure when the liquid is water can be taken as 1000 kg/m^3 and 101325 Pa, respectively.

The relationship between the volume fraction of gas ψ and pressure for the "single-equivalent fluid" assumptions can be expressed as (Guinot 2001a):

$$p\psi^{\beta} = p_{ref}\psi_{ref}^{\beta} \tag{3.5}$$

The pressure-wave celerity in presence of liquid only depends upon the elastic properties of the conduit, the bulk modulus of elasticity of the fluid, as well as on the external constraints. The general expression of the pressure-wave celerity is given by (e.g., Chaudhry 1987):

$$a = \left[\frac{k_f/\rho_f}{1+\frac{k_f}{Y}\chi}\right]^{1/2} \tag{3.6}$$

where k_f is the bulk modulus of elasticity of the fluid, Y is Young's modulus of elasticity of the pipe material, and χ is a non-dimensional parameter that depends upon the geometric properties of the conduit and pipe restraints. Substituting Eq. (3.4) into Eq. (3.3) and integrating the differentials $d\Omega$ and dp (A_f is assumed to be constant) leads to the following equation that relates p and Ω:

$$\Omega = \Omega_{ref} + \frac{A_f}{a^2}\left[p - p_{ref} + (p_{ref}^{\frac{-1}{\beta}} - p^{\frac{-1}{\beta}})\beta\psi_{ref}\rho_{f_{ref}}a^2 p_{ref}^{\frac{1}{\beta}}\right] \tag{3.7}$$

where $\Omega_{ref} = \rho_{f_{ref}}A_f$. The pressure p in Eq. (3.7) can be determined by an iterative scheme such as the Newton Raphson method and typically between three and five iterations are needed to ensure convergence. In single-phase liquid flows, the pressure-wave celerity is constant and no iteration is required to determine p. In this case, the following relation between p and Ω is obtained:

$$p = p_{ref} + \frac{a^2}{A_f}(\Omega - \Omega_{ref}) \tag{3.8}$$

The flow variables used in this chapter are Ω and Q_m. However, the engineering community prefers to use the piezometric head h and flow discharge Q. The latter variables can be determined from Ω and Q_m as follows:

$$Q = \frac{Q_m}{\Omega} A_f \tag{3.9}$$

$$h = \frac{p - p_{ref}}{\rho_{f_{ref}} g} + \frac{d}{2} \tag{3.10}$$

where d is the pipe diameter and h is measured over the conduit bottom. The absolute pressure head (H) in meters of water can be obtained as $H = h + 10.33$.

3.3 Formulation of finite volume Godunov-type schemes

This method is based on writing the governing equations in integral form over an elementary control volume or cell, hence the general term of Finite Volume (FV) method. The computational grid or cell involves discretization of the spatial domain x into cells of length Δx_i and the temporal domain t into intervals of duration Δt. The ith cell is centered at node i and extends from $i-1/2$ to $i+1/2$. The flow variables (Ω and Q_m) are defined at the cell centers i and represent their average value within each cell. Fluxes, on the other hand are evaluated at the interfaces between cells ($i-1/2$ and $i+1/2$). For the ith cell, the integration of Eq. (3.1) with respect to x from control surface $i-1/2$ to control surface $i+1/2$ yields:

$$\mathbf{U}_i^{n+1} = \mathbf{U}_i^n - \frac{\Delta t}{\Delta x_i}(\mathbf{F}_{i+1/2}^{n+1/2} - \mathbf{F}_{i-1/2}^{n+1/2}) + \frac{\Delta t}{\Delta x_i}\int_{i-1/2}^{i+1/2} \mathbf{S} dx \tag{3.11}$$

where the superscripts n, $n+1/2$, and $n+1$ reflect the t, $t+\Delta t/2$, and $t+\Delta t$ time levels, respectively. In Eq. (3.11), the determination of $\mathbf{U}$ at the new time step $n+1$ requires the computation of the numerical flux ($\mathbf{F}_{i+1/2}^{n+1/2}$) at the cell interfaces and the evaluation of the source term. In the Godunov approach, the flux $\mathbf{F}_{i+1/2}^{n+1/2}$ is obtained by solving the Riemann problem with constant states $\mathbf{U}_i^n$ and $\mathbf{U}_{i+1}^n$. This way of computing the flux leads to a first-order accuracy of the numerical solution. To achieve second-order accuracy in space and time, the Monotone Upstream-centred Scheme for Conservation Laws (MUSCL)-Hancock method is used in this chapter, which is described in the next section.

3.3.1 The MUSCL-Hancock method

The first step of the MUSCL-Hancock method (e.g., Toro 2001) is the reconstruction of piece-wise constant data $\mathbf{U}_i^n$ into a piecewise linear distribution of the data $\mathbf{U}_i^n(x) = \mathbf{U}_i^n + (x - x_i)\Delta i/\Delta x$, where $x_i = (i-1/2)\Delta x$ is the center of the computing cells and Δi is a vector difference $[\Delta i = (\mathbf{U}_{i+1}^n - \mathbf{U}_{i-1}^n)/2]$, and then extrapolation of the data to the edges of each cell, yielding the extrapolated values $\mathbf{U}_L$ and $\mathbf{U}_R$. To avoid spurious oscillations near shock waves and other sharp flow features, a Total Variation Diminishing (TVD) constraint is enforced in the data reconstruction step by limiting Δ_i. The MINMOD pre-processing slope limiter is used in this chapter to enforce the TVD constraint.

The reader is referred to the book of Toro (2001) for a detailed description of the available limiters.

The second step consists in evolving the extrapolated values through a half time step according to

$$\widetilde{\mathbf{U}}_{L,R} = \mathbf{U}_{L,R} - \frac{1}{2}\frac{\Delta t}{\Delta x}\Big[\mathbf{F}(\mathbf{U}_R) - \mathbf{F}(\mathbf{U}_L)\Big]. \tag{3.12}$$

where $\mathbf{F}(\mathbf{U})$ indicates the flux of $\mathbf{U}$.

In the third step, a Riemann problem with initial data consisting of evolved boundary extrapolated values is solved. In what follows, efficient approximate Riemann solvers for two and single-phase water hammer flows that do not require iterations are proposed.

3.3.2 Riemann solver for two-phase water hammer flows

In contrast with single-phase water hammer flows, in two-phase flows the pressure-wave celerity may be reduced to very low values, in which case u is not necessarily negligible compared to a_m. However, u is still smaller than a_m and consequently the characteristics travel in opposite directions and the star region ($\star$), which is an intermediate region between the left and right states, contains the location of the initial discontinuity. Thus, the flow variables in the star region are used to compute the flux. Simple estimates for $\Omega_\star$ and $Qm_\star$ that do not require iterations can be obtained by solving the Riemann problem for the linearized hyperbolic system $\partial\mathbf{U}/\partial t + \partial\mathbf{F}(\mathbf{U})/\partial x = 0$ with $\mathbf{F}(\mathbf{U}) \equiv \overline{\mathbf{A}}\mathbf{U}$, $\overline{\mathbf{A}} = \mathbf{A}(\overline{\mathbf{U}})$ and $\overline{\mathbf{U}} \equiv (\mathbf{U}_L + \mathbf{U}_R)/2$. This is described next.

The two eigenvalues for the matrix $\overline{\mathbf{A}}$ are given by: $\overline{\lambda}_1 = \overline{u} - \overline{a}_m$ and $\overline{\lambda}_2 = \overline{u} + \overline{a}_m$, where $\bar{a}_m = (a_{m_L} + a_{m_R})/2$ and $\bar{u} = (u_L + u_R)/2$. The application of the Rankine-Hugoniot conditions across the two waves [$\overline{\lambda}_i$ $(i = 1, 2)$] gives:

$$Qm_\star - Qm_L = (\bar{u} - \bar{a}_m)\big(\Omega_\star - \Omega_L\big) \tag{3.13}$$

$$Qm_R - Qm_\star = (\bar{u} + \bar{a}_m)\big(\Omega_R - \Omega_\star\big) \tag{3.14}$$

From Eqs. (3.13) and (3.14) the following relations for $\Omega_\star$ and $Qm_\star$ are obtained.

$$\Omega_\star = \big(\frac{\Omega_L + \Omega_R}{2}\big)\left(1 + \frac{u_L - u_R}{2\bar{a}_m}\right) \tag{3.15}$$

$$Qm_\star = Qm_L + (\bar{u} - \bar{a}_m)(\Omega_\star - \Omega_L\big) \tag{3.16}$$

By using the estimated values of $\Omega_\star$ and $Qm_\star$, the flux is obtained from Eq. (3.2).

3.3.3 Riemann solver for single-phase water hammer flows

In this type of flows, the pressure-wave celerity is constant and the order of magnitude of u is much smaller than a, so the convective term in the governing equations can be neglected. With these simplifications, the analytical solution of the Riemann problem for the linearized hyperbolic system $\partial \mathbf{U}/\partial t + \partial \mathbf{F}(\mathbf{U})/\partial x = 0$ provides the following estimates for $\Omega_\star$ and $Qm_\star$

$$\Omega_\star = \frac{\Omega_L + \Omega_R}{2} + \frac{Qm_L - Qm_R}{2a} \tag{3.17}$$

$$Qm_\star = \frac{Qm_L + Qm_R}{2} + a\frac{\Omega_L - \Omega_R}{2} \tag{3.18}$$

which are used to compute the flux by using Eq. (3.2).

3.4 Second-order accurate boundary conditions

Since Eq. (3.11) is to be used for all the cells of the computational domain, it is necessary to compute the fluxes $\mathbf{F}_{1/2}^{n+1/2}$ (left-hand boundary) and $\mathbf{F}_{Nx+1/2}^{n+1/2}$ (right-hand boundary) in order to update the flow variables in the first and last cells. For the quality of the numerical solution to be preserved, it is necessary to use the same order of reconstruction in all the cells of the computational domain (e.g., LeVeque 2002, Guinot 2003). The MUSCL-Hancock scheme uses one cell on each side of the cell in which the profile is to be reconstructed. Therefore, one cell is missing when the profile is to be reconstructed within the first and last cells of the computational domain. The missing information at the boundaries is restored by adding one virtual cell at each end of the computational domain. The virtual cell on the left-hand side is numbered 0, while the cell on the right-hand side of the domain is numbered $Nx + 1$ (Fig. 3.1). The algorithm consists of the following steps: (1) determination of $\mathbf{U}$ at the boundaries $1/2$ and $Nx + 1/2$, and (2) determination of the average flow variables $\mathbf{U}$ over the virtual cells.

3.4.1 Determination of flow variables at boundaries

It is assumed that the average flow variables in the cells 0 to $Nx+1$ are known from the previous time step and that a second-order reconstruction has been carried out in the cells 1 and Nx (Fig. 3.1). The unknown boundary flow

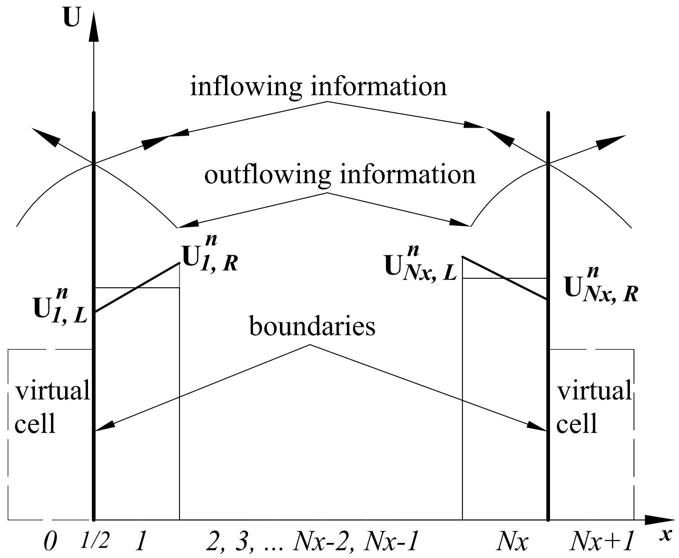

Figure 3.1: Second-order boundary conditions by adding virtual cells.

variables ($\mathbf{U}_b$) are determined using the theory of Riemann invariants. The reader is referred to the book of LeVeque (2002) for a deeper discussion on the theory of Riemann invariants. The generalized Riemann invariants for two-phase water hammer flows are given by (e.g., Guinot 2003):

$$\begin{cases} (a_m/\Omega)d\Omega + du = 0 \quad \text{along } dx/dt = u + a_m \\ (a_m/\Omega)d\Omega - du = 0 \quad \text{along } dx/dt = u - a_m \end{cases} \tag{3.19}$$

Due to space limitations, only the procedure to compute the flux at the left-hand boundary is provided in this section. However, the algorithm is very similar for the right-hand boundary. The left-hand boundary (b) is connected to the left of the first cell ($1, L$) along the characteristic $dx/dt = u - a_m$ (Fig. 3.2). Thus, for the left-hand boundary, the second relationship of Eq. (3.19) is integrated between b and $1, L$, which integration can be approximated according to the trapezoidal rule as follows:

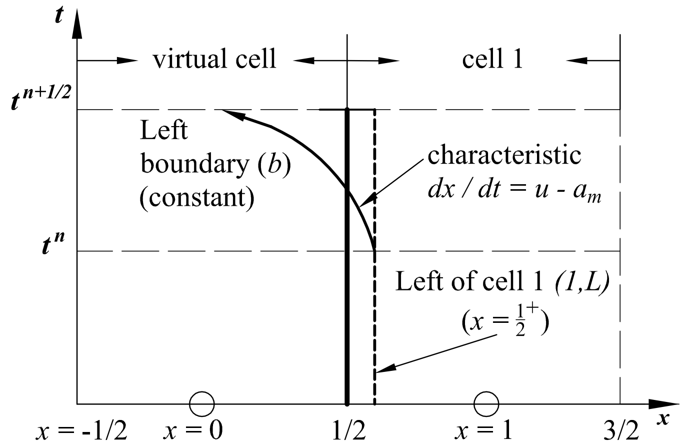

Figure 3.2: Path of integration at left-hand boundary.

$$\frac{a^n_{m1,L} + a^{n+1/2}_{m_b}}{2}(\Omega^{n+1/2}_b - \Omega^n_{1,L}) - \frac{\Omega^n_{1,L} + \Omega^{n+1/2}_b}{2}(u^{n+1/2}_b - u^n_{1,L}) = 0 \quad (3.20)$$

Another relationship is available from prescribing one flow variable or an equation that relates the two flow variables at the boundary. This relationship (ζ_b) may be expressed as:

$$\zeta_b(\Omega^{n+1/2}_b, Q^{n+1/2}_{m_b}) = 0 \quad (3.21)$$

Depending of the type of boundary condition imposed, it may or may not be necessary to use an iterative technique to solve the system of Eqs. (3.20) and (3.21). Following computation of the flow variables at the boundaries ($\mathbf{U}^{n+1/2}_b$), their fluxes can be computed by using the flux relation in Eq. (3.2).

For instance, let's consider that the pressure is prescribed at the left-hand boundary ($p^{n+1/2}_b$). This is equivalent to prescribing a mass per unit length $\Omega^{n+1/2}_b$, computed from Eq. (3.7).

$$\Omega_b = \Omega_{ref} + \frac{A_f}{a^2}\left[p_b - p_{ref} + (p_{ref}^{\frac{-1}{\beta}} - p_b^{\frac{-1}{\beta}})\beta\psi_{ref}\rho_{f\,ref}a^2 p_{ref}^{\frac{1}{\beta}}\right] \tag{3.22}$$

The value of $u_b^{n+1/2}$ is obtained from Eq. (3.20). This yields:

$$u_b^{n+1/2} = u_{1,L}^n + \frac{(a_{m_{1,L}}^n + a_{m_b}^{n+1/2})(\Omega_b^{n+1/2} - \Omega_{1,L}^n)}{\Omega_b^{n+1/2} + \Omega_{1,L}^n} \tag{3.23}$$

Since the pressure is prescribed at the boundary, $a_{m_b}^{n+1/2}$ is known from Eq. (3.4). Thus $u_b^{n+1/2}$ is the only unknown in Eq. (3.23). Once $u_b^{n+1/2}$ is determined, $Q_{m_b}^{n+1/2}$ can be calculated ($Q_{m_b}^{n+1/2} = \Omega_b^{n+1/2}u_b^{n+1/2}$). Once $\Omega_b^{n+1/2}$, $Q_{m_b}^{n+1/2}$, and $A_f p_b^{n+1/2}$ are known, the flux at the left-hand boundary $\mathbf{F}_b^{n+1/2} = \mathbf{F}_{1/2}^{n+1/2}$ can be computed by using the flux relation in Eq. (3.2).

Now, let's consider that the discharge is prescribed at the left-hand boundary ($Q_b^{n+1/2}$). Prescribing $Q_b^{n+1/2}$ is equivalent to prescribing a velocity $u_b^{n+1/2} = Q_b^{n+1/2}/A_f$. Eq. (3.20) can be solved for $\Omega_b^{n+1/2}$ as

$$\Omega_b^{n+1/2} = \left[1 + 2\frac{u_b^{n+1/2} - u_{1,L}^n}{a_{m_{1,L}}^n + a_{m_b}^{n+1/2} - u_b^{n+1/2} + u_{1,L}^n}\right]\Omega_{1,L}^n \tag{3.24}$$

in which $\Omega_b^{n+1/2}$ and $a_{m_b}^{n+1/2}$ are the unknowns. The solution is found iteratively. A first guess is made for $\Omega_b^{n+1/2}$ (for instance $\Omega_b^{n+1/2} = \Omega_{1,L}^n$) and this first guess is inserted into Eq. (3.22) to compute $p_b^{n+1/2}$. The computed value of $p_b^{n+1/2}$ in turn is inserted into Eq. (3.4) to compute $a_{m_b}^{n+1/2}$. This value is used in Eq. (3.24) to update $\Omega_b^{n+1/2}$, the new value of which is used to compute $a_{m_b}^{n+1/2}$. The procedure is repeated until convergence is achieved. Once $\Omega_b^{n+1/2}$ is determined, $p_b^{n+1/2}$ can be calculated from Eq. (3.22). Once $\Omega_b^{n+1/2}$, $A_f p_b^{n+1/2}$, and $Q_{m_b}^{n+1/2}(= \Omega_b^{n+1/2} u_b^{n+1/2})$ are known, $\mathbf{F}_{1/2}^{n+1/2}$ can be computed as in the previous case.

For single-phase flows, the fluxes at the boundaries can be also obtained from the generalized Riemann invariants. Since in single-phase water hammer flows the flow velocity is much smaller than the pressure-wave celerity, the convective term (Q_m^2/Ω) in the flux vector in Eq. (3.2) is neglected. In this case, if a pressure is prescribed at the left-hand boundary ($p_b^{n+1/2}$), the following relations are obtained for $\Omega_b^{n+1/2}$ and $Q_{m_b}^{n+1/2}$:

$$\Omega_b^{n+1/2} = \Omega_{ref} + \frac{A_f}{a^2}(p_b^{n+1/2} - p_{ref}) \tag{3.25}$$

$$Q_{m_b}^{n+1/2} = Q_{m_{1,L}}^n + a(\Omega_b^{n+1/2} - \Omega_{1,L}^n) \tag{3.26}$$

Because the convective term was neglected, only $A_f p_b^{n+1/2}$, and $Q_{m_b}^{n+1/2}$, are substituted into the flux vector $\mathbf{F}_{1/2}^{n+1/2}$ in Eq. (3.2).

Likewise, if a discharge is prescribed at the left-hand boundary ($Q_b^{n+1/2}$), the following relations are obtained for $\Omega_b^{n+1/2}$ and $Q_{m_b}^{n+1/2}$:

$$\Omega_b^{n+1/2} = \frac{Q_{m_{1,L}}^n - a\Omega_{1,L}^n}{Q_b^{n+1/2}/A_f - a} \tag{3.27}$$

$$Q_{m_b}^{n+1/2} = \frac{Q_b^{n+1/2}}{A_f}\Omega_b^{n+1/2} \tag{3.28}$$

The value of $\Omega_b^{n+1/2}$ can be substituted in Eq. (3.8) to determine $p_b^{n+1/2}$. Once $A_f p_b^{n+1/2}$, and $Q_{m_b}^{n+1/2}$ are known, $\mathbf{F}_{1/2}^{n+1/2}$ can be computed as in the previous case.

3.4.2 Determination of U in the virtual cells

Virtual cells are used only to achieve second-order accuracy in the first and last cells of the computational domain. Therefore, they should advect the same outflowing information as that at the boundaries and they should maintain the conservation property of the shock capturing scheme. The latter means that no unphysical perturbations into the computational domain may be introduced by the virtual cells. These constraints may be satisfied: (1) by assuming that the outflowing wave strengths in the virtual cells are the same as those at the boundaries, and (2) by adjusting the inflowing wave strengths in the virtual cells in such a way that the fluxes in these cells are the same as those at the respective boundaries. For the left hand boundary, a simple formulation that satisfies these two conditions is given by:

$$\begin{aligned} \Omega_0^{n+1} &= \Omega_{1/2}^{n+1/2} = \Omega_b^{n+1/2} \\ Q_{m_0}^{n+1} &= Q_{m_{1/2}}^{n+1/2} = Q_{m_b}^{n+1/2} \end{aligned} \tag{3.29}$$

Note in Eq. (3.29) that the vector flow variable at the left-hand boundary ($\mathbf{U}_{1/2}^{n+1/2}$) is adopted by the virtual cell "0" at the time level "$n+1$" that is used for the reconstruction of $\mathbf{U}$ in the cell "1" at this time level, unless monotonicity needs to be preserved in this cell. Note that the inflowing and outflowing fluxes in the cell 0 are the same, which means that no perturbations are introduced from the virtual cells into the computational domain when updating the solution. Notice also that with this formulation, the outflowing information advected by the virtual cells is the same as that at the boundaries.

3.5 Incorporation of source terms

In a similar way to Zhao and Ghidaoui (2004), the source terms $\mathbf{S}$ are introduced into the solution through time splitting using a second-order Runge-Kutta discretization which results in the following explicit procedure.

First step (pure advection):

$$\mathbf{U}_i^{n+1} = \mathbf{U}_i^n - \frac{\Delta t}{\Delta x}(\mathbf{F}_{i+1/2}^{n+1/2} - \mathbf{F}_{i-1/2}^{n+1/2}) \tag{3.30}$$

Second step (update with source term by $\Delta t/2$):

$$\overline{\mathbf{U}}_i^{n+1} = \mathbf{U}_i^{n+1} + \frac{\Delta t}{2}\mathbf{S}\big(\mathbf{U}_i^{n+1}\big) \tag{3.31}$$

Last step (re-update with source term by Δt):

$$\overline{\overline{\mathbf{U}}}_i^{n+1} = \mathbf{U}_i^{n+1} + \Delta t\mathbf{S}\big(\overline{\mathbf{U}}_i^{n+1}\big) \tag{3.32}$$

where $\mathbf{S}(\mathbf{U})$ indicates that $\mathbf{U}$ is used to evaluate the source term $\mathbf{S}$. The evaluation of $\mathbf{S}$ requires the definition of the grid bottom slope $(S_0)_i$ given by

$$(S_0)_i = -\frac{z_{i+1/2} - z_{i-1/2}}{x_{i+1/2} - x_{i-1/2}} = -\frac{\Delta z_i}{\Delta x_i} \tag{3.33}$$

and the grid energy line slope $(S_f)_i$ which may be expressed as $(S_f)_i = f u_i|u_i|/(2gd)$, where f is the Darcy-Weisbach friction factor.

3.6 Stability constraint

Since the explicit second-order Runge-Kutta discretization has been used for the incorporation of $\mathbf{S}$ into the solution, the stability constraint must include not only the Courant-Friedrichs-Lewy (CFL) criterion for the convective part, but also the constraint for the source terms. The CFL constraint is given by:

$$\Delta t_{\text{max, CFL}} = \text{Min}_{\ i=1,2,...Nx} \left[\frac{\Delta x_i}{|u_i^n| + |a_{m_i}^n|} \right] \tag{3.34}$$

and the constraint due to the explicit second-order Runge-Kutta discretization is given by (León et al. 2006a)

$$\Delta t_{max,\mathbf{S}} = \text{Min}_{\ i=1,2,...Nx} \left[-4 \frac{\mathbf{U}_i^{n+1}}{\mathbf{S}(\mathbf{U}_i^{n+1})}, -2 \frac{\mathbf{U}_i^{n+1}}{\mathbf{S}(\overline{\mathbf{U}}_i^{n+1})} \right] \tag{3.35}$$

Since the same time step Δt must be used for the convective part and the source term, $\mathbf{U}_i^n$ must be used instead of $\mathbf{U}_i^{n+1}$. Finally, the maximum permissible time step including the convective part and the source term will be given by:

$$\Delta t_{max} = \text{Min}_{\ i=1,2,...Nx} \left[\Delta t_{max,\mathbf{S}}, \ \ \Delta t_{\text{max, CFL}} \right] \tag{3.36}$$

3.7 Evaluation of the model

The purpose of this section is to asses the accuracy and numerical efficiency of the proposed scheme for modeling one and two-phase water hammer flows. For single-phase flows, the accuracy and numerical efficiency of the proposed scheme is compared against those of the fixed-grid MOC scheme with space-line interpolation and the second-order scheme of Zhao and Ghidaoui (2004). For two phase flows, the accuracy and numerical efficiency of the proposed scheme is compared to the fixed-grid MOC scheme with space-line interpolation. The proposed scheme is also used to reproduce a set of two-phase flow experiments reported in the literature. Four tests cases are considered in this section. These are:

1. Instantaneous downstream valve closure in a frictionless horizontal pipe (one-phase flow)
2. Gradual downstream valve closure in a frictionless horizontal pipe (one-phase flow)
3. Instantaneous downstream valve closure in a frictionless horizontal pipe (two-phase flow)
4. Comparison with two-phase flow experiments of Chaudhry et al. (1990)

The proposed approach is valid for pipes with and without friction. In the three first tests, frictionless pipes are used only because in such cases the physical dissipation is zero, so any dissipation or amplification in the results is solely due to the numerical scheme. In the following sections, the number of grids, grid size and Courant number used in each example are indicated in the relevant figures and thus will not be repeated in the text. The CPU times that are reported in this paper were averaged over three realizations and computed using a HP AMD Athlon (tm) 64 processor 3200 + 997 MHz, 512 MB of Ram notebook.

3.7.1 Test 1: Instantaneous downstream valve closure in a frictionless horizontal pipe (one-phase flow)

This test is used to compare the accuracy and numerical efficiency of the proposed scheme against the Zhao and Ghidaoui (2004) approach and the MOC scheme with space-line interpolation for single-phase flows under strong transient conditions. A strong transient refers to a transient phenomena in which the resulting flow presents discontinuities (sharp fronts). This type of transient is generated for instance after an instantaneous valve closure. On the other hand, a smooth transient refers to a transient phenomena in which the resulting flow doesn't present discontinuities. This transient is produced for instance after a gradual valve closure. The test considers one horizontal frictionless pipe connected to an upstream reservoir and a downstream valve. The length of the pipe is 10000 m and its diameter is 1.0 m, the pressure-wave celerity is 1000 m/s, the upstream reservoir constant head h_0 is 200 m, and the initial steady-state discharge is 2.0 m^3/s.

The transient flow is obtained after an instantaneous closure of the downstream valve. To investigate the performance of the schemes under consideration when using low Courant numbers, these schemes are used to reproduce the resulting transient using a coarse grid (to illustrate their performance better) and two low Courant numbers ($Cr = 0.5$ and $Cr = 0.1$). A portion of the simulated pressure traces are shown in Figs. 3.3(a) and 3.3(b). Additional simulations were performed using a $Cr = 1.0$. As expected, all schemes under consideration have reproduced the exact solution when $Cr = 1.0$ (results not shown). It is clear from Figs. 3.3(a) and 3.3(b) that the MOC is more dissipative than either the second-order scheme of Zhao and Ghidaoui or the proposed scheme for low Courant numbers. The results also show that the

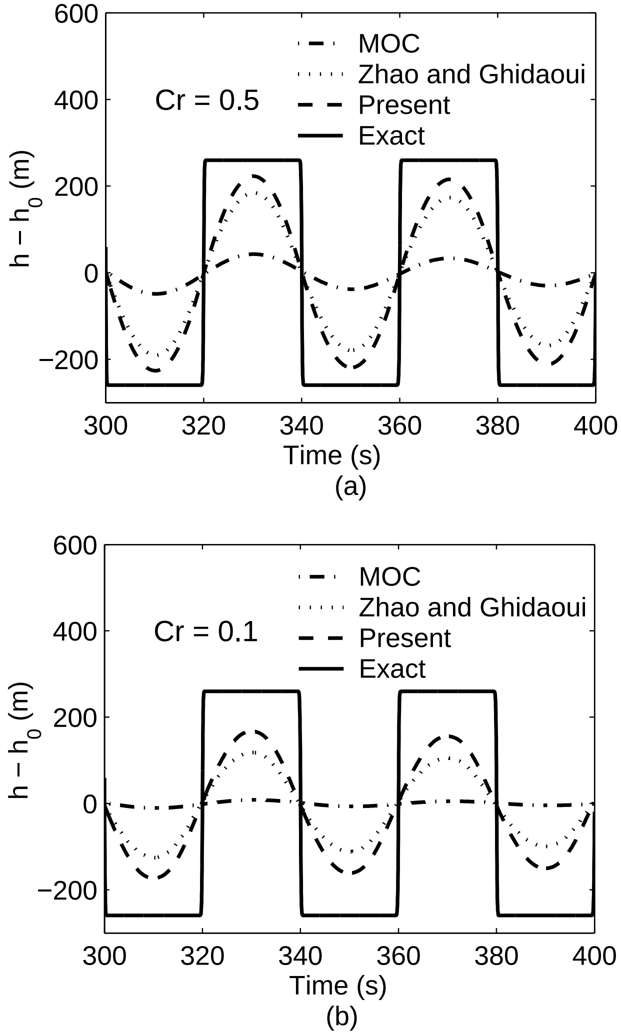

Figure 3.3: Pressure traces at downstream valve for test No 1 ($Nx = 10$ cells) using (a) $Cr = 0.5$, and (b) $Cr = 0.1$.

proposed scheme is less dissipative than the scheme of Zhao and Ghidaoui. The basic difference between the second-order scheme of Zhao and Ghidaoui and the proposed approach for single-phase flows is that only a first-order boundary condition is used in the former approach, and a second-order one in the latter.

In the previous simulations, the reader may question the low Courant numbers used. Although in real large-scale systems, whose pipes have different lengths and water hammer wavespeeds, it is impossible to achieve a Courant number of 1.0 when a coarse computational grid is chosen, it can be shown that by increasing the number of cells, a Cr close to 1.0 can be achieved. In the latter condition, a good performance of all schemes is expected. A realistic assessment of accuracy and numerical efficiency of the schemes has to take into account the variation of the Courant number with the number of grids (Nx). The variation of Cr versus Nx is not the same for different pipe systems. However, the trend of Cr vs Nx is similar for several scenarios tested (results not shown). The trend of Cr versus Nx adopted in this test case is presented in Fig. 3.4. This trend was obtained using the pipe system presented in Ghidaoui et al. (1998). This system consisted of two pipes in series where the length of the upstream pipe was 800 m and the length of the downstream one was 300 m. The pressure wave celerity for both pipes was 1000 m/s. The discretization strategy was based on the pipe that has the minimum wave travel time (Karney and Ghidaoui 1997). The approach of using at least one reach in the pipe that has the minimum wave travel time guarantees that the Courant number in the remaining pipes of the system is bounded by 0.5 and 1.0.

To obtain a quantitative measure of numerical dissipation, the energy equation of Karney (1990) can be used (Ghidaoui et al. 1998). The energy equation of Karney states that the total energy (sum of internal and kinetic) can only change as work is done on the conduit or as energy is dissipated from it. In this test the friction is set to zero, so the rate of total energy dissipation is zero. Moreover, because the downstream valve is closed instantaneously, no fluid is exchanged with the environment across a pressure difference; therefore the work produced at the downstream end of the pipe is also equal to zero (Ghidaoui et al. 1998). As an aside, the rate of change of internal energy (δU) given

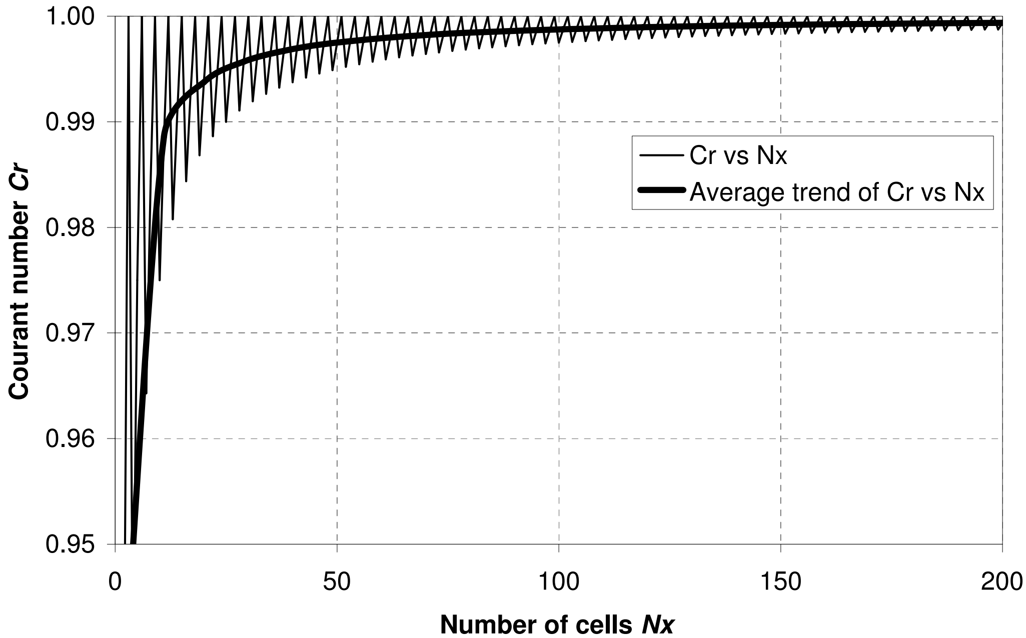

Figure 3.4: Courant number versus number of cells.

in Karney (1990) in our notation is given by $\delta U = d[(\rho_f L A_f g^2 (h_s - h)^2)/(2a^2)]$, where h_s is the head after the transient flow has reached steady state measured over the conduit bottom. By integrating this relation considering that $U = 0$ at $h = h_s$, the expression for the internal energy at any time can be written as: $U = (\rho_f A_f g^2)/(2a^2) \int (h_s - h)^2 dx$. Notice that in this test, the head h_s is the same as the head at the reservoir and thus, no work is produced at the upstream end of the pipe (see energy equation of Karney 1990). Therefore, the total energy (sum of kinetic and internal) in the pipe E is invariant with time (i.e., $E/E_0 = 1$).

Fig. 3.5 shows relative energy traces E/E_0 produced by the schemes under consideration for two coarse grids ($Nx = 10$ and 20 cells). The Courant number associated to each number of cells is obtained from Fig. 3.4 (average trend) and its values are presented together with the number of cells in Fig. 3.5 caption. Fig. 3.5 shows that, the numerical dissipation produced by the proposed scheme using 10 cells is smaller than that obtained by either the MOC scheme

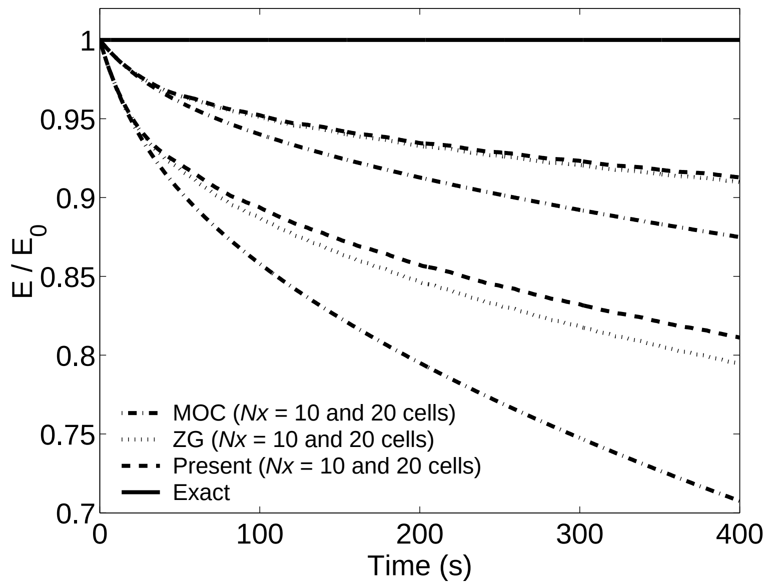

Figure 3.5: Energy traces for test No 1 ($Nx = 10$ cells, $Cr = 0.9829$; $Nx = 20$ cells, $Cr = 0.9938$).

or the Zhao and Ghidaoui approach for the same number of cells. For instance, after 400 s, 29% of the initial energy has been dissipated by the MOC scheme, 21% by the scheme of Zhao and Ghidaoui and 18% by the proposed scheme. The numerical dissipation results for all the schemes produced using 20 cells show a significant reduction compared to those using 10 cells. This reduction is not only due to the increase of cell numbers (10 to 20) but mainly due to the associated increase of the Courant number (0.9829 to 0.9938). So far, it has been shown that, for coarse grids, the proposed scheme is more accurate than either the MOC scheme or the approach of Zhao and Ghidaoui. However, an objective comparison requires measuring the CPU time needed by each of the schemes to achieve the same level of accuracy (e.g., Zhao and Ghidaoui 2004, León et al. 2006).

To compare the numerical efficiency of the schemes, the numerical dissipation (numerical error) is plotted against the number of grids on log-log scale (Fig. 3.6). As shown in Fig. 3.6, for coarse grids, the accuracy of the proposed scheme is almost the same as Zhao and Ghidaoui and slightly superior than the MOC scheme. For relatively fine grids ($Nx > 1000$), the accuracy of the three schemes is almost the same. For comparison of CPU times, five levels of numerical error were selected (0.1% - 10%). The number of grids needed by each scheme to achieve the five numerical error levels were obtained from Fig. 3.6. These number of grids in turn were used to determine their associated Courant numbers (Fig. 3.4) and the CPU times. Fig. 3.7 shows the plot of the numerical error against the CPU time on log-log scale. The CPU time results show that, to achieve the same degree of accuracy, the proposed scheme has a similar numerical efficiency as the Zhao and Ghidaoui scheme. The results also show that the MOC is more efficient numerically than the proposed scheme and the Zhao and Ghidaoui approach despite the fact that, for a given level of accuracy, the MOC scheme requires a finer grid than the proposed scheme and the Zhao and Ghidaoui approach. For the conditions presented in Fig. 3.7, it is found that the MOC scheme is about 2 to 5 times faster to execute than the proposed scheme and the Zhao and Ghidaoui approach.

3.7.2 Test 2: Gradual downstream valve closure in a frictionless horizontal pipe (one-phase flow)

This test is used to compare the accuracy and numerical efficiency of the proposed scheme against the Zhao and Ghidaoui (2004) approach and the MOC scheme with space-line interpolation for single-phase flows under smooth transient conditions (no discontinuities). The test rig used is adapted from Wylie and Streeter (1983). This test rig considers one horizontal frictionless pipe connected to an upstream reservoir and a downstream valve. The length of the pipe is 600 m and its diameter is 0.5 m, the pressure-wave celerity is 1200

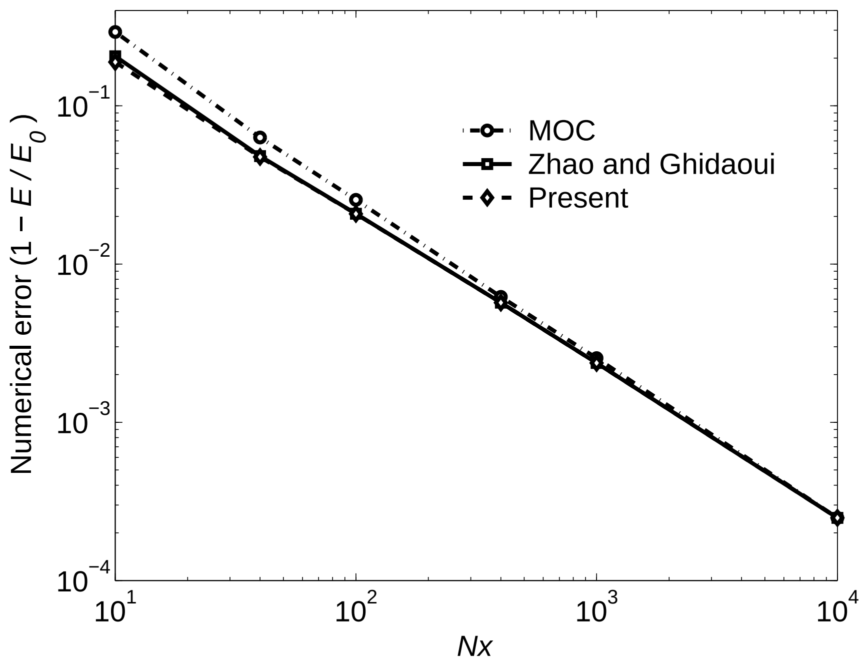

Figure 3.6: Numerical error versus number of grids for test No 1 ($t = 400\ s$).

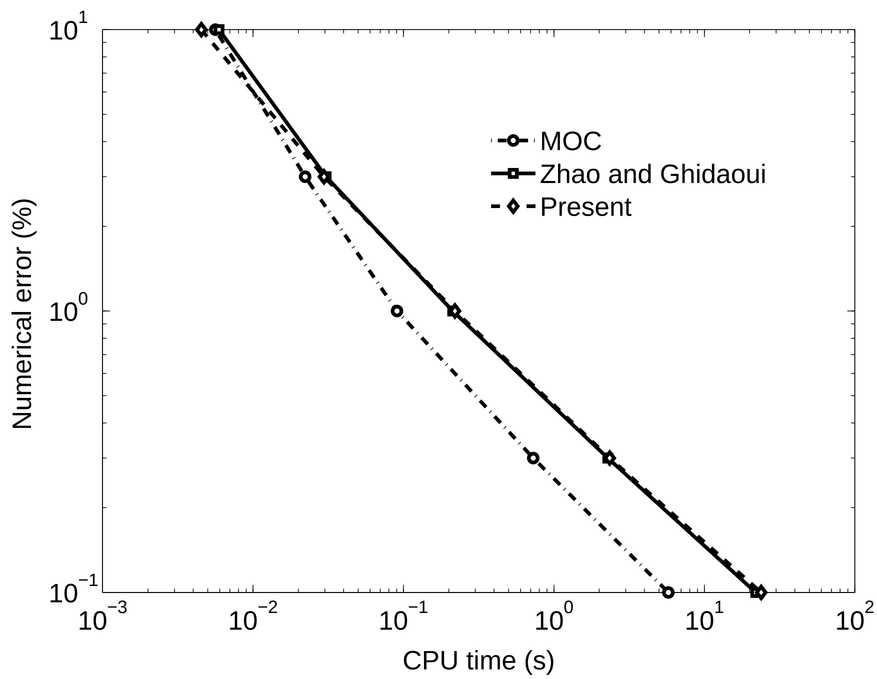

Figure 3.7: Relation between level of accuracy and CPU time for test No 1 ($t = 400\ s$).

m/s, the upstream reservoir constant head h_0 is 150 m, and the initial steady-state discharge is 0.4882 m^3/s. The transient flow in this test is obtained after a gradual closure of the downstream valve. The valve closure relationship is given by $\tau = (1 - t/t_c)^{1.5}$ where t_c is the time of valve closure, which has been assumed to be 2.1 s.

In the previous test, it was shown that when Cr is very close to 1.0 ($>$ 0.99), the MOC scheme is slightly less accurate than the proposed scheme and the Zhao and Ghidaoui approach, but it can be more efficient than these schemes. The same occurs in smooth transient conditions for single-phase flows. Due to space limitations, results are not shown. As is shown in Fig. 3.4, although the Courant number average trend tends 1.0 when Nx is increased, the Courant number has a periodic variation with the number of grids. Thus, a Cr very close to 1.0 cannot be guaranteed in all the pipes. To investigate the performance of the schemes for Courant numbers slightly less than 1.0, a $Cr =$ 0.95 is considered in this test. Fig. 3.8 shows simulated pressure traces at the downstream valve using this Courant number and $Nx = 40$ cells. The "Near exact" solution is also presented in this figure. The "Near exact" solution is obtained by grid refinement until convergence is achieved. As is shown in this figure, the MOC is more dissipative than either the second-order scheme of Zhao and Ghidaoui or the proposed scheme. The results also show that the proposed scheme is less dissipative than the scheme of Zhao and Ghidaoui.

To obtain a quantitative measure of numerical dissipation, the energy equation of Karney (1990) is also used here. In this test, work is produced at the downstream boundary while fluid is exchanged with the environment across a pressure difference. Thus, the total energy (sum of kinetic and internal) is not invariant with time while the valve is being closed. After the valve is closed,

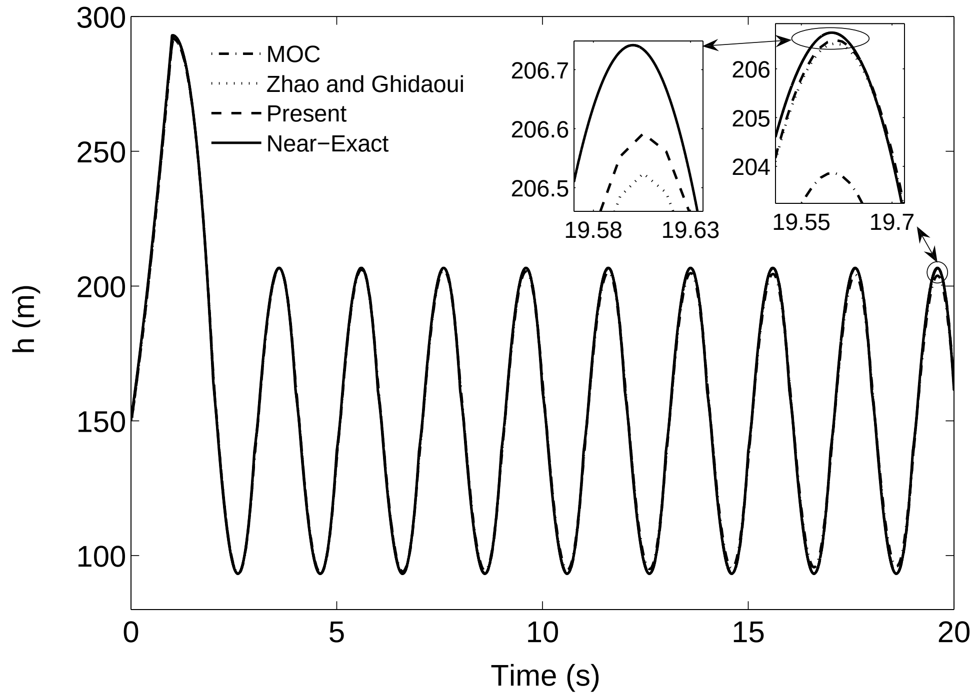

Figure 3.8: Pressure traces at downstream valve for test No 2 ($Nx = 40$ cells, $Cr = 0.95$).

no work is done or energy is dissipated on the conduit, and therefore the total energy is invariant with time. Fig. 3.9 shows relative energy traces produced by the schemes under consideration for $Cr = 0.95$ and $Nx = 40$ cells. The relative energy is expressed as E/E_c, where E_c is the total energy after the valve is totally closed, and E is the total energy at time t. Fig. 3.9 shows a reduction in the relative energy until the valve is totally closed ($t = 2.1s$). For $t > 2.1s$, the relative energy is constant and equal to 1.0. Since all numerical schemes are dissipative, the relative energy traces achieved by the schemes (after the valve is closed) are smaller than 1.0 (Fig. 3.9).

Fig. 3.10 shows the plot of the numerical error against the number of grids on log-log scale. As shown in this figure, to achieve a given level of accuracy, the MOC scheme requires a much finer grid than the proposed scheme and the Zhao and Ghidaoui approach. For comparison of CPU times, five levels of

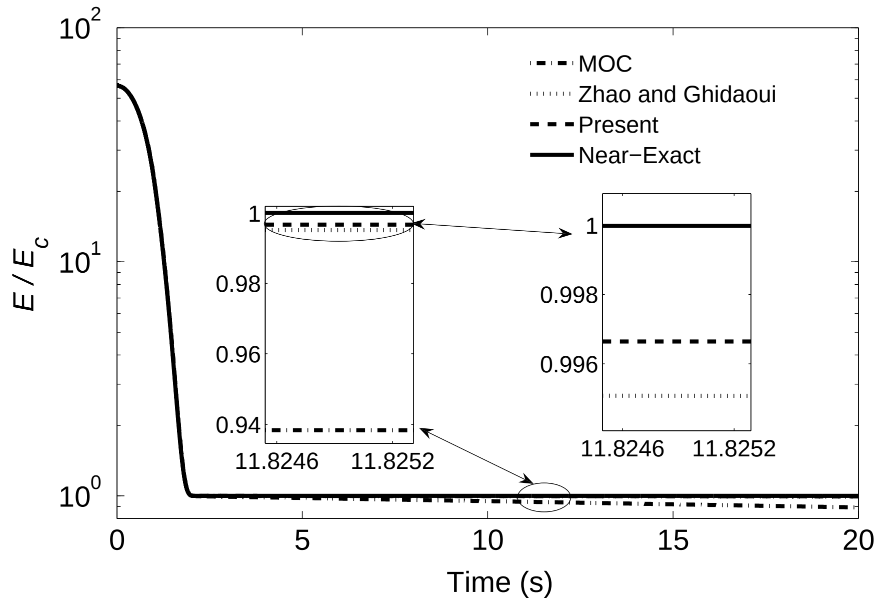

Figure 3.9: Energy traces for test No 2 ($Nx = 40$ cells, $Cr = 0.95$).

numerical error were selected (0.1% - 10%). The number of grids needed by each of the schemes to achieve the five levels of numerical error, were obtained from Fig. 3.10. These number of grids in turn were used to compute the CPU times. The numerical error is plotted as a function of CPU time in Fig. 3.11. This figure shows that, to achieve the same degree of accuracy, the proposed scheme requires less CPU time than either the MOC scheme or the Zhao and Ghidaoui approach. For instance, for a numerical error of 1%, the CPU time required by the proposed scheme is about 0.04 and 0.71 times of those required by the MOC scheme and the Zhao and Ghidaoui approach, respectively. For the CPU time results presented in Fig. 3.11, it is found that, the proposed scheme is about 7 to 249 times faster to execute than the MOC scheme, and 34% to 67% faster than the scheme of Zhao and Ghidaoui.

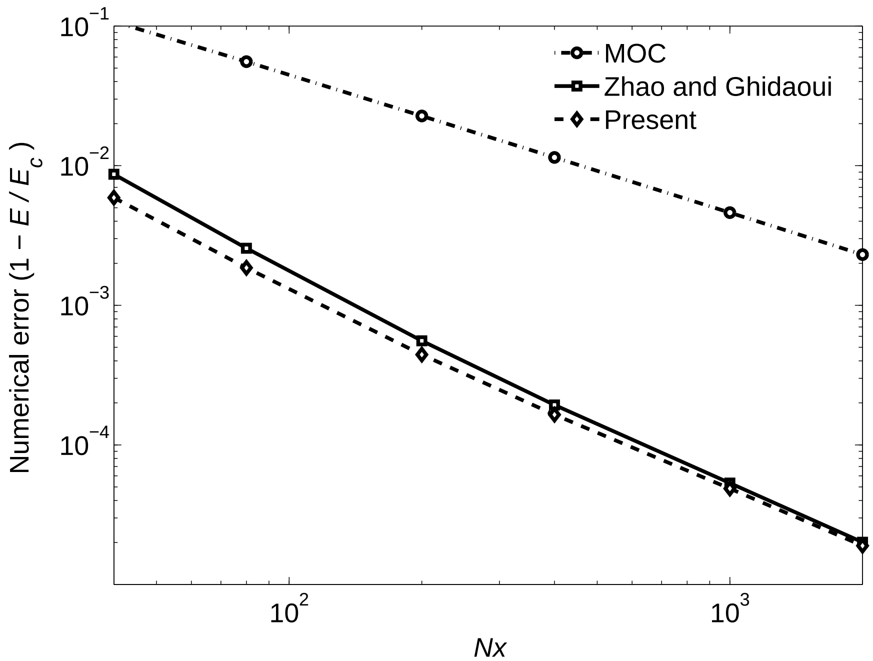

Figure 3.10: Numerical error versus number of grids for test No 2 ($t = 20$ s, $Cr = 0.95$).

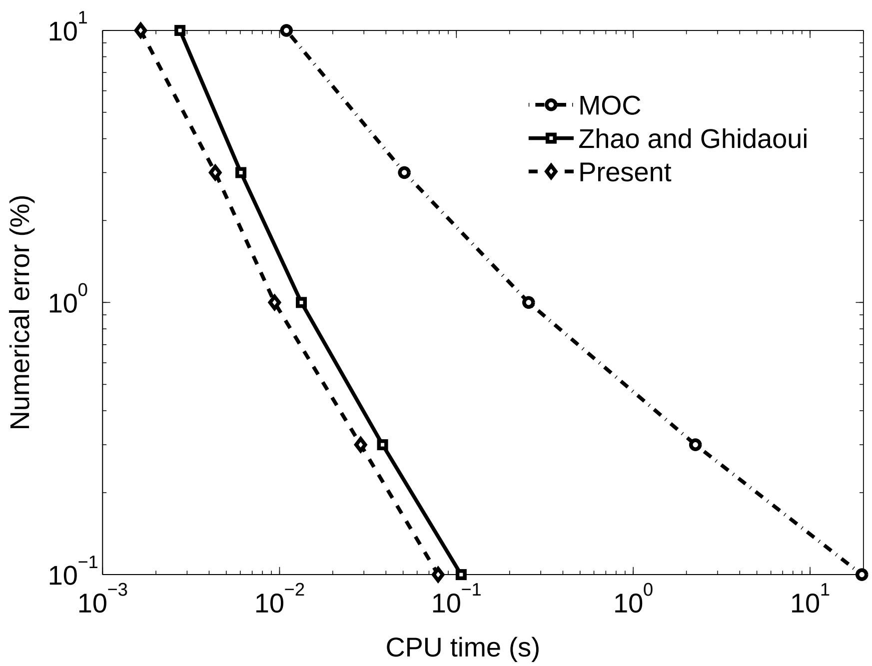

Figure 3.11: Relation between level of accuracy and CPU time for test No 2 ($t = 20$ s, $Cr = 0.95$).

3.7.3 Test 3: Instantaneous downstream valve closure in a frictionless horizontal pipe (two-phase flow)

This test is used to compare the accuracy and numerical efficiency of the proposed scheme against the fixed-grid MOC scheme for two-phase flows. The two-phase homogeneous mathematical model presented in Martin (1993) is solved when using the MOC scheme. In this case, if shocks are present, the Rankine-Hugoniot conditions are enforced across the shock. The test rig is the same as test 1, except that the fluid is an air-water mixture. The void ratio at the reference pressure (101325 Pa) is assumed to be 0.002 (0.2%). The instantaneous closure of the downstream valve results in the appearance of a shock wave at the downstream end of the pipe. This wave propagates upstream until on reflection against the left boundary, it becomes a rarefaction wave. Fig. 3.12 shows the pressure profiles at 140 s computed using the MOC scheme and the proposed approach assuming isothermal conditions ($\beta = 1.0$) for two different number of grids. The "Near exact" profile is also presented in this figure. In this test case, all the simulations were carried out using a maximum Courant number of 0.95 to avoid numerical instability problems. It should be noted that in two phase flows, the air content and pressure wave celerity are continuously changing (Eqs. 3.4 and 3.5). When using an explicit scheme (as used here) for simulating these flows, it is possible to exceed $Cr = 1.0$ if a Cr close to 1.0 is specified at the beginning of the time step. As shown in Fig. 3.12, for the same number of grids and maximum Courant number, the timing and magnitude of the shock wave simulated by the proposed scheme is in better agreement with the "Near exact" solution than the MOC scheme.

Fig. 3.13 displays the simulated pressure traces at the middle of the pipe for two different number of grids. As can be observed in this figure, the

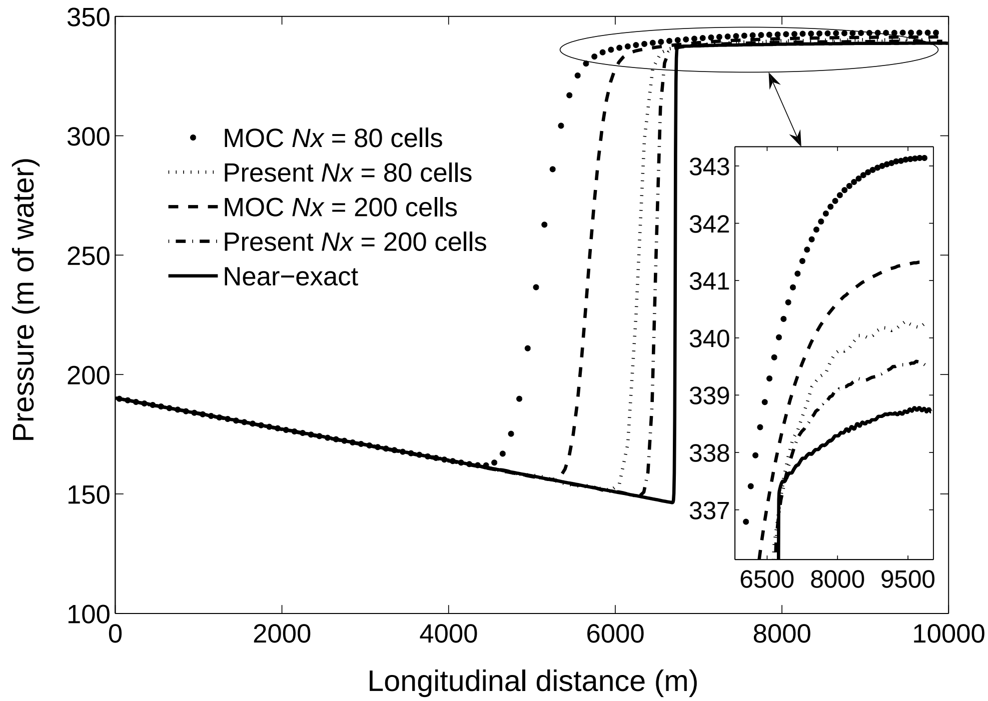

Figure 3.12: Pressure head versus longitudinal distance for test No 3 ($\beta = 1.0$, $t = 140$ s and $Cr_{max} = 0.95$).

MOC is more dissipative than the proposed scheme. The results presented in Figs. 3.12 and 3.13 show that, for the same discretization, the proposed scheme is more accurate than the MOC scheme. A more conclusive comparison requires measurement of the CPU time needed by each scheme to achieve a given level of accuracy. The accuracy of a scheme can be measured using the following error norm (e.g., Liang et al. 2007):

$$\text{ABSERROR} = \frac{\Sigma_{i=1}^{Nx}|e_i|}{\Sigma_{i=1}^{Nx}|\phi_i^{\text{exact}}|} \tag{3.37}$$

where $e_i = \phi_i^{\text{numerical}} - \phi_i^{\text{exact}}$ = difference between the numerical and exact solution at node i, ϕ = dependent variable such as the pressure head or flow velocity, ABSERROR = absolute error, and Nx = number of grids. The absolute error is a measure of the difference between the numerical and exact

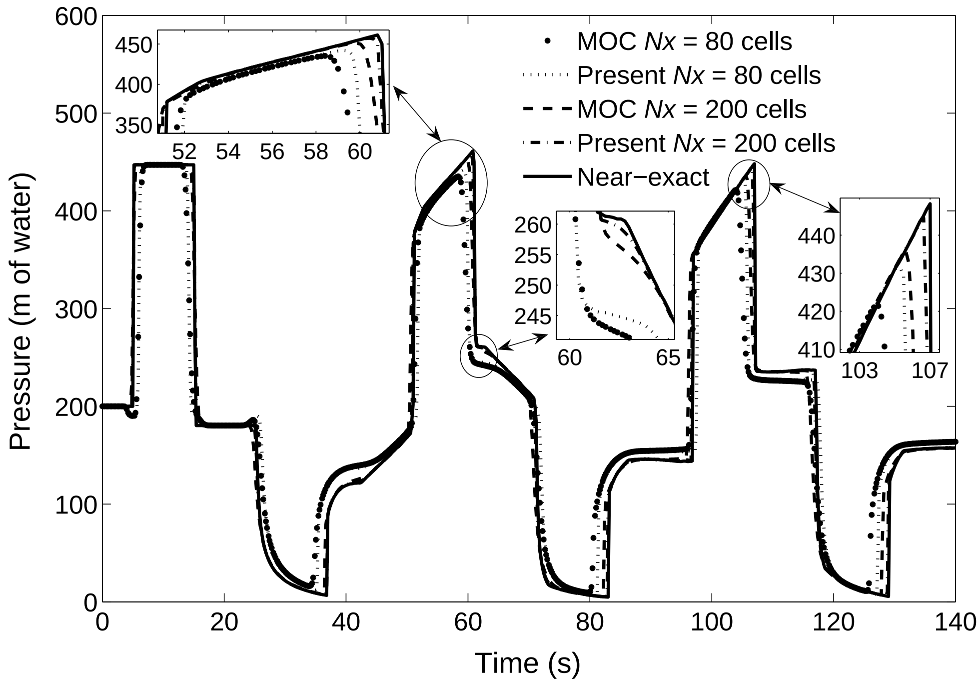

Figure 3.13: Pressure traces at the middle of the pipe for test No 3 ($\beta = 1.0$ and $Cr_{max} = 0.95$).

solution for either the pressure head or flow velocity.

Fig. 3.14 shows the plot of the absolute error for the pressure head against the number of grids on log-log scale. As shown in this figure, to achieve a given level of accuracy, the MOC scheme requires a finer grid than the proposed scheme, or, for the same number of grids, the proposed scheme is more accurate than the MOC scheme. For comparison of CPU times, four levels of absolute error were selected (0.4% - 10%). The number of grids needed by each of the schemes to achieve the four absolute error levels, were obtained from Fig. 3.14. These number of grids in turn were used to compute the CPU times, which results are shown in Fig. 3.15. The CPU time results show that the proposed scheme is about 3 to 130 times faster to execute than the MOC scheme. The numerical efficiency of the proposed scheme compared to the MOC approach increases as the absolute error decreases.

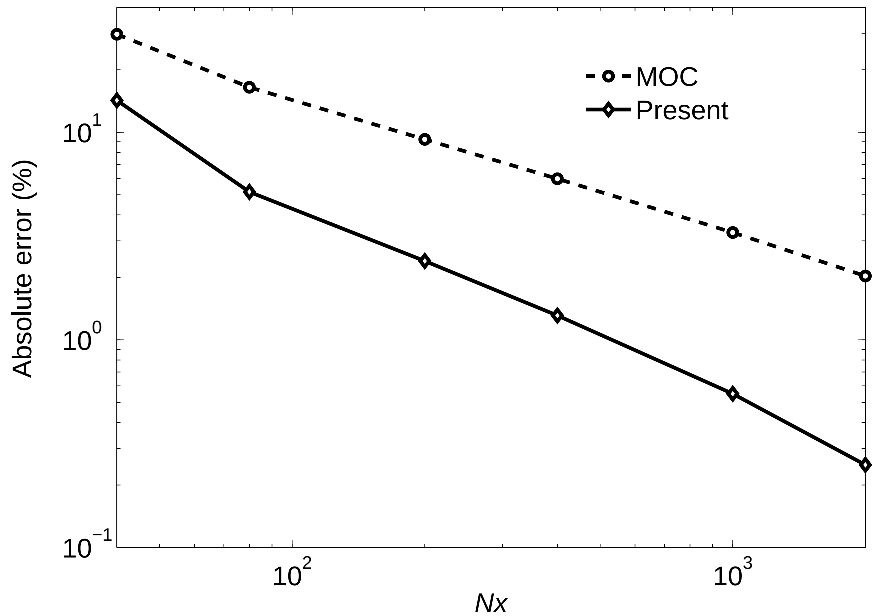

Figure 3.14: Absolute error for the pressure head versus number of grids for test No 3 ($\beta = 1.0$, $t = 140\ s$ and $Cr_{max} = 0.95$).

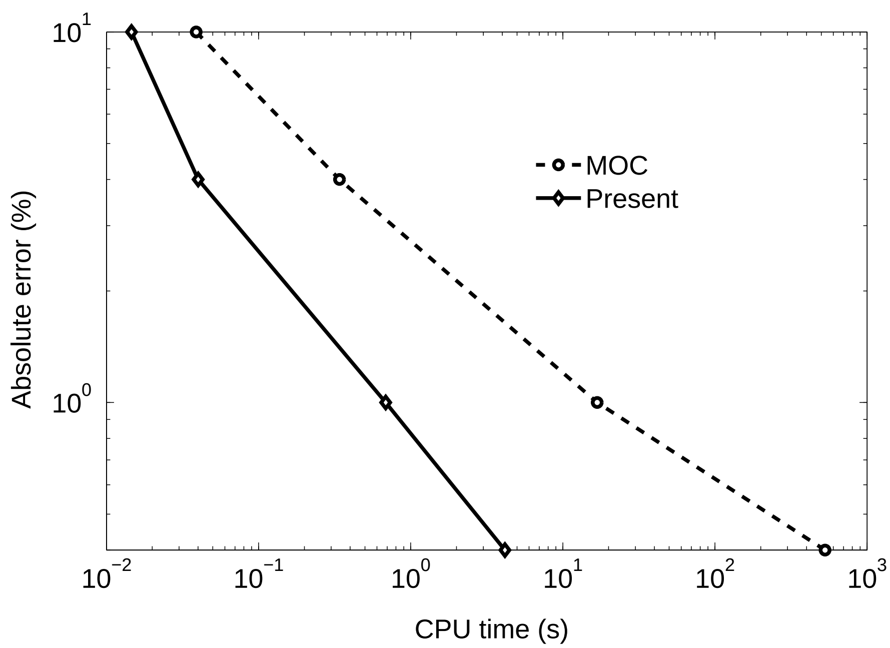

Figure 3.15: Absolute error for the pressure head versus CPU time for test No 3 ($\beta = 1.0$, $t = 140\ s$ and $Cr_{max} = 0.95$).

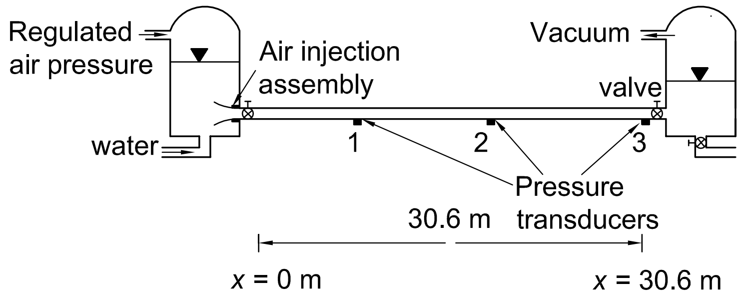

Figure 3.16: Schematic of experiment Chaudhry et al. (1990).

3.7.4 Test 4: Comparison with two-phase flow experiments of Chaudhry et al. (1990)

In this test, the fixed-grid MOC and the proposed scheme are used to reproduce the second set of experiments reported in Chaudhry et al. (1990). The writers are indebted to one of the authors of this paper, namely Professor C. Samuel Martin, who kindly provided us the data for this set of experiments. The schematic of the test facility is shown in Fig. 3.16. The conditions for the second set of experiments reported in Chaudhry et al. (1990) are reproduced in Table 3.1.

The test procedure was as follows: A steady state flow of an air-water mixture was established in the test pipe by controlling the exit valves and the pressure of the injected air at the inlet. The flow velocity of the air-water mixture was maintained at a high enough rate so that slug flow could be avoided by limiting the rate of air injection. Transient flow was created by a rapid valve closure at the downstream end of the pipe. Transient-state pressures were monitored by high-frequency-response pressure transducers at three locations (1, 2 and 3), as shown in Fig. 3.16. The three stations were located at $x = 8\ m$, $21.1\ m$ and $30.6\ m$, respectively, from the upstream end.

The upstream boundary was a constant-level reservoir while the downstream boundary was the recorded pressure history at station 3 ($x = 30.6\ m$).

Table 3.1: Experimental conditions for second set of experiments reported in Chaudhry et al. (1990).

Description	**Values**
Length L (m)	30.600
Diameter d (m)	0.026
Bed slope S_0 (m/m)	0.000
Upst. reserv. press. H_0 (m of water absol.)	21.700
Steady flow velocity u_0 (m/s)	2.940
Darcy-Weisbach friction factor f_q	0.0195
Pressure-wave celerity a (m/s)	715.000
Steady air mass flow rate (kg/s)	1.15x10^{-5}
Downstream void ratio ψ_{ref}	0.0053

A flow discharge boundary condition was not used at the downstream end because the rate of closure of the exit valve was not reported in Chaudhry et al. (1990). They suggested instead to use the recorded pressure history at station 3 as downstream boundary condition because the measurement of the rate of closure of a valve and, consequently the measurement of velocity are very difficult. The recorded pressure trace at station 3 is shown in Fig. 3.17.

The simulated pressure traces at stations 1 and 2, assuming isothermal ($\beta =$ 1.0) and adiabatic ($\beta = 1.4$) conditions, are presented with the corresponding experimental observations in Figs. 3.18 - 3.21. As shown in these figures, the simulated pressure traces using the MOC and the proposed scheme are very similar for isothermal and adiabatic conditions. Figs. 3.18 - 3.21 also show that the simulated peak pressures (MOC and proposed) are higher than those in the experiments for both conditions. In addition, the results show that the

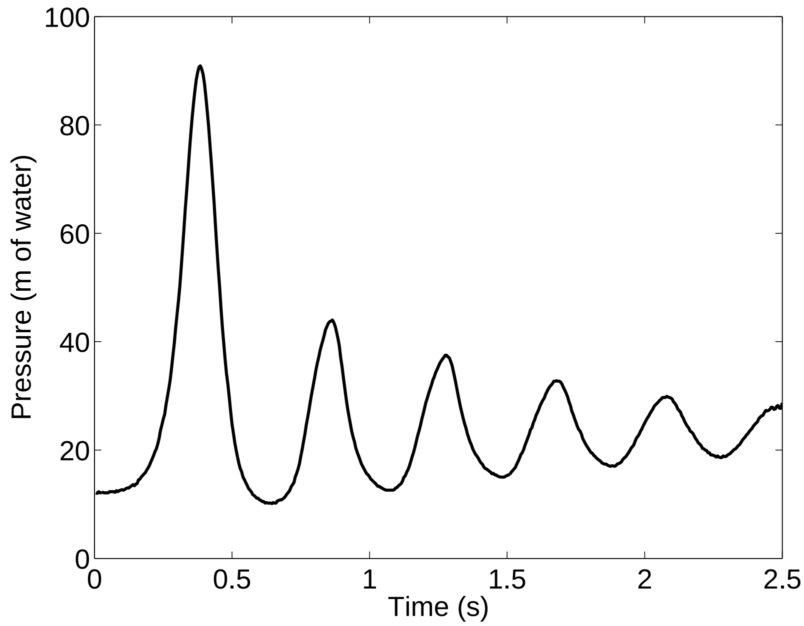

Figure 3.17: Experimental absolute pressure trace at downstream end ($x = 30.6\ m$).

simulated pressure traces agree with the experiments better when isothermal conditions (Figs. 3.18 - 3.19) were assumed than when adiabatic conditions (Figs. 3.20 - 3.21) were assumed. As an aside, a transient phenomena takes place in isothermal conditions when there is no change of temperature during the transient. Likewise, a transient phenomena develops in adiabatic conditions when no heat enters or leaves the system during the transient. In the experiments reported in Chaudhry et al. (1990), neither isothermal nor adiabatic conditions seem to have prevailed. This is believed because the time scale seems too fast for isothermal conditions to prevail. Also, the conductivity of a stainless steel pipe, which is the material of the pipe used in the experiments, is not very low for adiabatic conditions to hold.

By comparing the simulated results using the MOC and the proposed scheme, it can be seen that the pressure traces computed using the MOC are lower than the proposed scheme for all the simulations. This means that

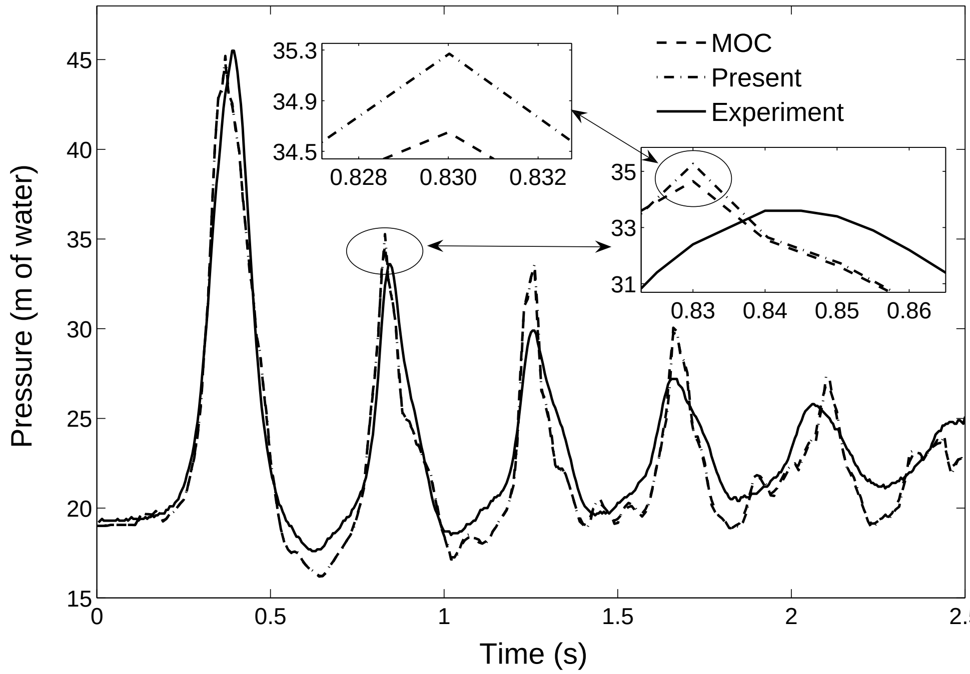

Figure 3.18: Computed and experimental absolute pressure traces at $x = 8$ m ($Nx = 100$ cells and $Cr_{max} = 0.95$). The computed pressure traces were performed under isothermal conditions ($\beta = 1.0$).

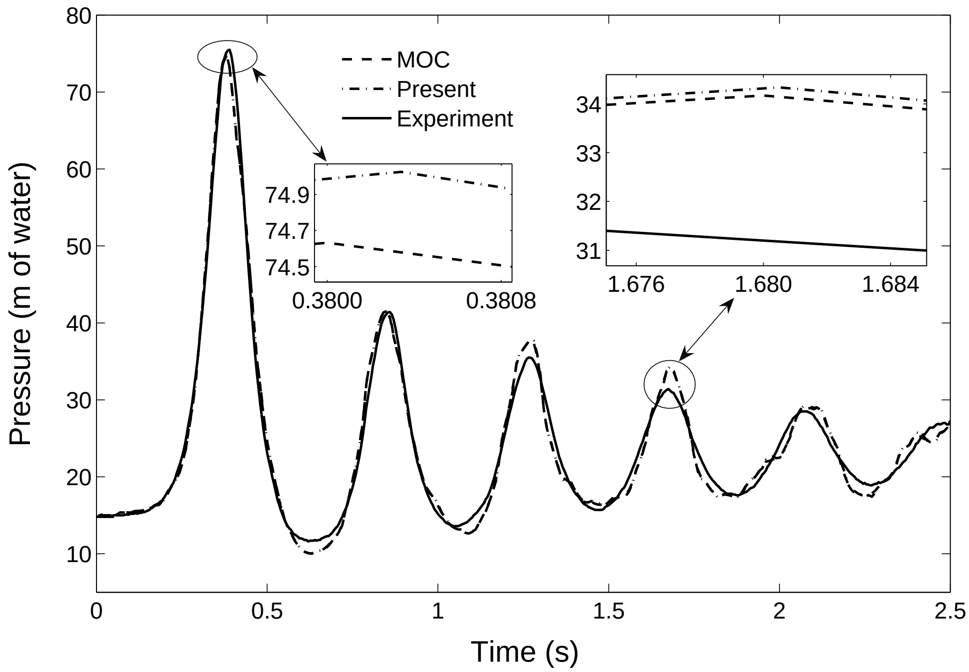

Figure 3.19: Computed and experimental absolute pressure traces at $x = 21.1$ m ($Nx = 100$ cells and $Cr_{max} = 0.95$). The computed pressure traces were performed under isothermal conditions ($\beta = 1.0$).

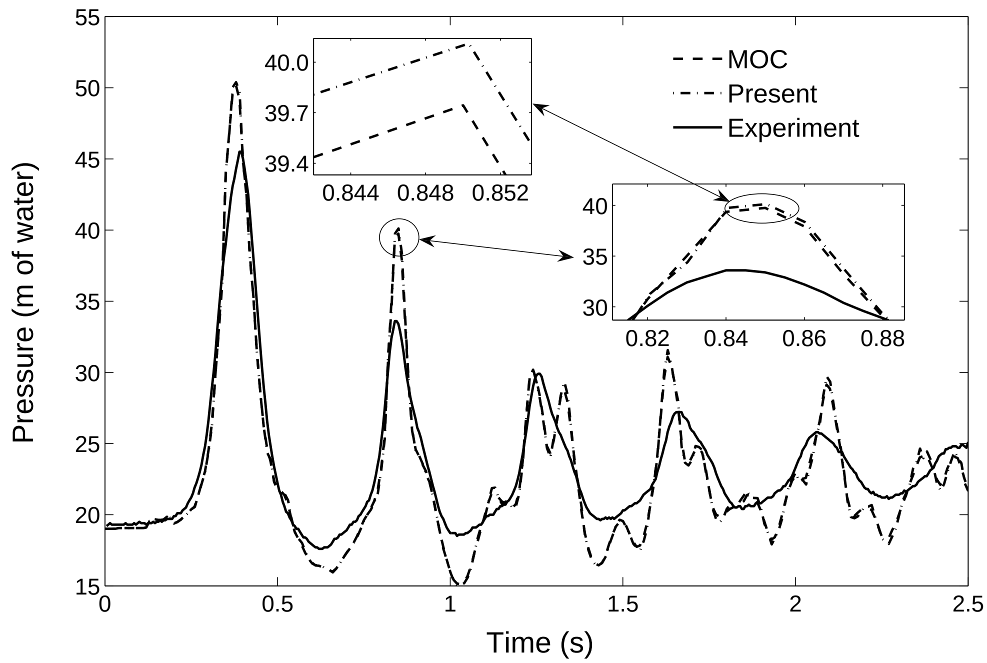

Figure 3.20: Computed and experimental absolute pressure traces at $x = 8$ m ($Nx = 100$ cells and $Cr_{max} = 0.95$). The computed pressure traces were performed under adiabatic conditions ($\beta = 1.4$).

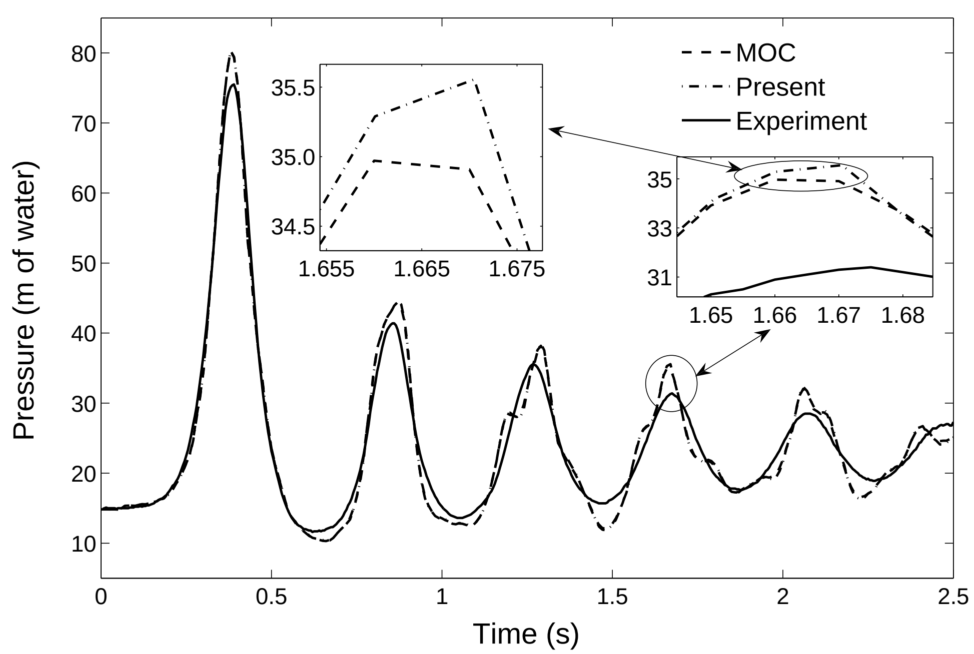

Figure 3.21: Computed and experimental absolute pressure traces at $x = 21.1$ m ($Nx = 100$ cells and $Cr_{max} = 0.95$). The computed pressure traces were performed under adiabatic conditions ($\beta = 1.4$).

the MOC is more dissipative than the proposed scheme. However, the MOC agrees with the experiments slightly better than the proposed scheme. This may be confusing because one can conclude that the MOC is more accurate than the proposed scheme. The apparent advantage of the MOC over the proposed scheme is because, as usually is the case, the physical dissipation can not be estimated with good accuracy and it is often underestimated. The last is especially true when the physical dissipation is estimated using only a steady friction formulation (as used here). Even though there are formulations to estimate unsteady friction (e.g., Pezzinga 2000), the physical dissipation often cannot be determined with good accuracy, especially in complex flows such as two-phase flows. As suggested by Cannizzaro and Pezzinga (2005), in two-phase flows, the physical dissipation is not only associated to the wall shear stress but also to thermodynamic processes (e.g., thermic exchange between the gaseous phase and the surrounding liquid and gas release). In general, it is very difficult and it may be misleading to compare the accuracy of numerical schemes using experiments. The discrepancies between simulated and observed values may be attributed to experimental uncertainty, to neglecting unsteady friction and thermodynamic processes when computing the physical dissipation, and due to the fact that the thermodynamic conditions during the experiments were neither isothermal nor adiabatic as was considered in the simulations.

Chapter 4

Single-phase mixed flows

4.1 Introduction

Single-phase models ignore the air phase and its interactions with the water phase. As a result, such models are unable to reproduce any flow behavior associated with the air phase such as pressure oscillation induced by the Helmholtz instability, the pre-bore motion or the counter flow motion associated with poor venting, the pressure oscillation due to air entrapment caused by the geometric instability, to name a few only (e.g., Schmidt et al. 2005).

The Helmholtz instability is developed at the air-water interface inside a conduit line, causing entrapment of air cavities and large pressure oscillations. This instability occurs in regions where there is large difference between the speed of the air layer and the speed of the water layer. Differences in velocity between the air layer and the water layer underneath it can, for example, occur when there is a shock front, which pushes the air in front in the direction opposite to the water layer. A counter current can also be set up when the water level at the downstream boundary drops suddenly below the pipe crown, causing the water to move out of the pipe while air rushes into the pipe to fill the void left by the water. The velocity differential at the air-water interface, along with the inevitable presence of surface water waves, causes the air pressure to be lowest near the crests of the perturbed interface and highest near its troughs. This pressure difference pushes the crest of the wave upward while the gravity force pulls the crest downward. The instability sets in when the pressure difference is larger than gravitational force (e.g., Kordyban 1977, Hamam and McCorquodale 1982). The amplitude of the water waves can become sufficiently large to reach the roof of the pipe causing the air column to be bridged by water. As a result, air becomes trapped between successive water columns. The Helmholtz instability at the interface of two fluids with different speeds is a classical problem in fluid mechanics and its treatment can be found in numerous books, papers and monographs. However, these studies are often performed under geometrical and dynamic conditions that are very different from those in pipe flows.

It is important to note that much of the complex dynamics in unsteady pipe flows is due to the air phase (e.g., Hamam and McCorquodale 1982, Cardle et al. 1988, Li and McCorquodale 1999, Vasconcelos and Wright 2003). The stability of the flow and the magnitude and frequency of pressures in a pipe system are highly affected by the initial volume of air in the pipe, by the rates of inflow and outflow of air into the pipe during the transient and by the pressure and velocity field in the air phase. Single phase models are unable to reproduce any flow behavior associated with the air phase. Therefore, single phase models are expected to be reasonable only when there is an unrestricted air supply into and out of the system and when the velocity is not large enough to produce any flow instability.

Single-phase mixed flows are traditionally simulated by one of two general approaches (e.g., Li and McCorquodale 1999, León et al. 2006d): (a) simulation of pressurized flows as free surface flows using a hypothetical narrow open-top slot ("Preissmann slot"); and (b) separate simulation of free surface and pressurized flows. Recently the Decoupled Pressure Approach (DPA) was introduced by Vasconcelos et al. (2006). An overview of these approaches is presented next.

4.1.1 Preissmann slot approach

The Preissmann approach, first applied by Cunge and Wegner (1964), assumes that the top of the pipe is connected to a slot, which is open to the atmosphere, and applies the SaintVenant equations to the pipe-slot open-channel. The hypothetical slot is ideally chosen so that the speed of gravity waves in the slot is equal to the water hammer wavespeed and the water level in the slot is equal to the water hammer head. Essentially, this approach exploits the similarity between the wave equations which describe free surface and pressurized flows. The wave nature of free surface flows comes from the ability of open channels to store mass by a change in water elevation. The wave nature of water hammer flows comes from the ability of a full pipe to store mass by a change in pipe area and fluid density. Clearly, the storage ability of free surface flows is much larger than water hammer flows. Therefore, forcing equivalence between the free surface and water hammer equations requires that the hypothetical slot stores as much fluid as a full pipe would through a change in pipe area and fluid density. This results in a slot with very high water level and extremely small width.

The combination of large water level and small width results in numerical instabilities (e.g., Yen 1986). Such instabilities can be removed by making the slot wider. However, changing the width of the slot destroys the equivalence between the water hammer and the free surface flow equations and results in incorrect wavespeeds and pressure heads. It seems there is a general confusion regarding the selection of the slot width. Papers devoted to numerical schemes for the simultaneous modeling of free surface and pressurized flows show that the size of the slot doesn't have a significant influence on the results for pressure heads (e.g., Trajkovic et al. 1999). Some authors even used a slot width as large as 10% of the pipe diameter (e.g., Trajkovic et al. 1999) and even so reported numerical instabilities. The small influence of the slot width on the resulting pressure heads when simulating mixed flows led to the incorrect conclusion that the Preissmann model with a wide slot can be used to model accurately free surface flows, pressurized flows and the simultaneous occurrence of free surface and pressurized flows. There are even commercial models intended for simulating all these flows in storm-sewer systems using the Preissmann slot approach with wide slots. The effect of the slot width when simulating open channel-pressurized flow interfaces is insignificant, but it is significant when modeling pure pressurized flows (flow in slot). The velocity of propagation of an open channel-pressurized flow interface is not greatly influenced by the wavespeed at each side of the interface but by the conservation of mass and momentum across the interface. In pure pressurized flows, however, the water hammer wavespeed determines how fast the pressure transients are propagated. The only way of reproducing the correct propagation and interaction of pressurized transients is by using a slot width that achieves a gravity wavespeed in the slot equal to the water hammer wavespeed.

Notwithstanding the problems associated with the size of the slot, the generic equivalence between the water hammer and the free surface flow equations does not imply that both flows are identical. The use of water level to represent the water hammer head prohibits the formation of sub-atmospheric pressures and the emergence of vapor cavities, which would occur in a water hammer flow when the pressure drops below vapor pressure. Whenever the head drops below the slot, the pressure produced by the Preissmann model is equivalent to the water depth in the pipe and the magnitude of the wavespeed drops from the water hammer wavespeed to the open-channel wavespeed. In reality, however, sub-atmospheric water hammer pressures could form during depressurization and the speed of these pressures is the same as the water hammer wavespeed. Therefore, Preissmann slot models cannot simulate sub-atmospheric pressures, and the results of these models after, as well as during, depressurization must be treated with caution.

The advantages of the Preissmann slot models are summarized in Yen (1986). They avoid any switching between free surface flow and pressurized flow equations, so there is no need to define a surcharging criteria or to track the interface between the open-channel and the surcharged portions of a pipe. In addition, Preissmann slot models avoid the special treatment at the flow boundaries and the numerical complexities that would be required to model the pressurized portion by the water hammer theory and the open-channel portion by the surface water theory.

4.1.2 Separate simulation of free surface and pressurized flows

The separate simulation of free surface and pressurized flows is more complex; however the methods based on this approach are able to simulate sub-atmospheric pressures in the pressurized flow regime. Current models based on this approach can not address some complex flow features well, such as open-channel surges, negative open channel-pressurized flow interfaces, and interface reversals. In this approach, the location of the moving interface between the two flow types is tracked and treated as an internal interface. This is often referred to as the “shock-fitting” method (e.g., Guo and Song 1990, Fuamba 2002). In this approach, the pressurized flow is treated using rigid water hammer theory (e.g., Wiggert 1972) or elastic water hammer theory (e.g., Cardle 1984).

The model of Wiggert (1972) is an example of a model that uses the Saint-Venant equation for the open-channel part and the rigid water hammer theory for the surcharged part. The rigid water hammer theory ignores any mass storage due to fluid compressibility and pipe elasticity. This theory precludes the computation of water hammer waves in the pressurized portion of the conduit; this is reasonable as long as the time scale of flow change exceeds the wave travel time through a pipe. This is often the case when the transient is generated by an inflow hydrograph, a controlled stoppage or start of a pump, gradual closures of gates and valves and uncontrolled failures of pumps which have high inertia. When the flow changes very quickly compared to the wave travel time, the elastic water hammer theory should be used.

The model of Song et al. (1984) is an example of a model that uses the Saint-Venant equation for the open-channel part and the elastic water hammer theory for the surcharged part. This model is suitable for sudden transient events such as sudden gate closures and the uncontrolled failure of a pump with low inertia and for long pipe lines. When using the model of Song et al. (1984), open-channel surges cannot be modeled and negative interfaces are not adequately addressed. Furthermore, the flow variables at each side of the free surface-pressurized flow interface are extrapolated from the respective adjacent cells, which may lead to mass and momentum conservation problems.

4.1.3 Decoupled pressure approach

Recently, Vasconcelos et al. (2006) introduced a Decoupled Pressure Approach (DPA), which is formulated by modifying the open-channel Saint-Venant equations to allow for overpressurization, assuming that elastic behavior of the pipe walls will account for the gain in pipe storage. One of the limitations of this approach is the presence of what these authors call "post-shock oscillations" near open channel-pressurized flow interfaces. To keep these oscillations small, lower values for the pressure wave celerity may be used, but this may compromise the accuracy of the simulation if pressurized transients are simulated.

4.2 Numerical schemes for modeling single-phase mixed flows

The Preissmann slot and the DPA approach use the free surface flow equations to simulate mixed flows. In the other hand, the shock-fitting approach treats free surface and pressurized flows separately. In the latter case, the same or a different numerical scheme may be used to simulate free surface and pressurized flows. Thus, to address the limitations and advantages of numerical schemes for the modeling of mixed flows, it is necessary to review the schemes available for modeling free surface and pressurized flows independently. A review of current numerical schemes available for modeling free surface and pressurized flows is presented in Chapters 2 and 3, respectively.

As can be seen in Chapters 2 and 3, most of the models developed primarily to examine the formation and propagation of hydraulic transients in free surface and pressurized flows are based on the Method of Characteristics (MOC), usually, the fixed-grid MOC scheme with space-line interpolation. León et al. (2006a, 2006b, 2006c) showed that, GTS schemes are superior to the fixed-grid MOC scheme with space-line interpolation for both free surface and pressurized flows. Thus, in this thesis, GTS schemes are chosen for simulating free surface, pressurized and mixed flows.

In this thesis, two fully-conservative, computationally efficient and robust models are formulated for simulating mixed flows. In the first model, which was implemented numerically for complex networks, pressurized flows are simulated as free surface flows using a hypothetical narrow open-top slot ("Preissmann slot"). In the second model, which was implemented numerically only for one single pipe, free surface and pressurized flows are treated independently while interacting through a moving interface.

In the first model, a gradual transition between the pipe and the slot is introduced and an explicit Finite Volume (FV) GTS scheme with a slope limiter is used to solve the governing equations (free surface flow). This model is called the *modified Preissmann model* and is able to produce stable results for strong (rapid) transients.

In the second model, both free surface and pressurized flows are handled using shock-capturing methods to which the GTS belong. Open channel-pressurized flow interfaces are treated using a shock-tracking-capturing approach. In this approach, cell boundaries are introduced at the location of open channel-pressurized flow interfaces, subdividing some regular cells into two subcells, resulting in a variable mesh arrangement that varies from one time step to the next. However, the vast majority of grid cells do not vary.

By having a cell boundary at each open channel-pressurized flow interface, we avoid the smearing and loss of accuracy that is inevitable when the discontinuity falls within a grid cell and the discrete solution must be averaged over the cell.

The formulated models for simulating mixed flows are presented in the next two sections. Each of these sections is organized as follows: (1) the governing equations in conservative form are presented; (2) a Riemann solver for the flux computation is presented; and (3) a brief overview for the formulation of boundary conditions is presented. Finally, the models are tested using experiments reported in the literature.

4.3 Modified Preissmann slot model

4.3.1 Governing equations

The one-dimensional open-channel flow continuity and momentum equations for prismatic conduits may be written in their vector conservative form as follows:

$$\frac{\partial \mathbf{U}}{\partial t} + \frac{\partial \mathbf{F}}{\partial x} = \mathbf{S} \tag{4.1}$$

where the vector variable $\mathbf{U}$, the flux vector $\mathbf{F}$ and the source term vector $\mathbf{S}$ may be written as (e.g., Guinot 2003, León et al. 2006a):

$$\mathbf{U} = \begin{bmatrix} A \\ Q \end{bmatrix}, \; \mathbf{F} = \begin{bmatrix} Q \\ \frac{Q^2}{A} + \frac{A\overline{p}}{\rho} \end{bmatrix} \text{ and } \mathbf{S} = \begin{bmatrix} 0 \\ (S_0 - S_f)gA \end{bmatrix} \tag{4.2}$$

where A = cross-sectional area of the flow; Q = flow discharge; $\overline{p}$ = average pressure of the water column over the cross sectional area; ρ = liquid density that is assumed to be constant (incompressible flow); g = gravitational acceleration; S_0 = slope of the bottom channel; and S_f = slope of the energy line. The model proposed in this section is applicable to any prismatic conduit, however in the rest of this section, only a circular cross-section conduit is considered.

When using the Preissmann approach for the treatment of pressurized flows, four main problems associated with the approach itself and with the numerical scheme used to solve the governing equations may be found: First, the inability of the Preissmann slot approach to describe sub-atmospheric full-pipe flows; Second, mass and momentum balance problems associated with the width of the slot; Third, instability problems associated with the poor performance of the numerical scheme when the flow changes rapidly from the pipe to the slot; and Fourth, inaccuracies in the propagation of pressurized transients (flow in slot) associated with the width of the slot.

When using the Preissmann approach nothing can be done to address the first problem, however the last three problems can be minimized. To address the second problem, a narrow slot can be used. The third problem (instability) is much more important in modeling strong (rapid) transient flows when the flow changes rapidly from the pipe to the slot, which may cause the computer simulation to abort. To address the fourth problem, a slot width that achieves a gravity wavespeed in the slot equal to the water hammer wavespeed can be used. This slot width (T_s) is given by

$$T_s = \frac{gA_f}{a^2} \tag{4.3}$$

where A_f is the full cross-sectional area of the pipe and a is the water hammer wavespeed.

In the proposed approach (called the *modified Preissmann model*), the fourth problem is addressed by using a slot width that achieves a gravity wavespeed in the slot equal to the water hammer wavespeed. This results in narrow slots minimizing mass and momentum balance problems (second problem). The third problem (instability) is addressed by: (1) using a slope limiter (MINMOD) in the Monotone Upstream-centred Scheme for Conservation Laws (MUSCL)-Hancock method (see Chapter 3) such that the monotonicity of the solution is preserved, and (2) introducing a gradual transition between the pipe and the slot [Fig. 4.1 (b)] such that the transition between free surface and pressurized flows occurs gradually. Differences between results produced by simulations that included and ignored the area of the slot and the pressure force over the slot area were negligibly small. Thus, these parameters were ignored.

4.3.2 Formulation of finite volume Godunov-type schemes

The formulation of FV Godunov-type schemes is described in Chapters 2 and 3. In the Godunov approach, the fluxes at the cell interfaces are evaluated by solving the Riemann problem. In the proposed model (both frameworks), the Riemann problem is solved using the HLL Riemann solver that is described in Chapters 2 and 3. For this Riemann solver the wavespeeds need to be determined. Following, an estimate for wavespeeds using the two-shock wave approximation is derived.

Figs. 4.2(a) and 4.2(b) illustrate the physical space and phase space for the two-shock wave approximation, respectively. In order to facilitate the ap-

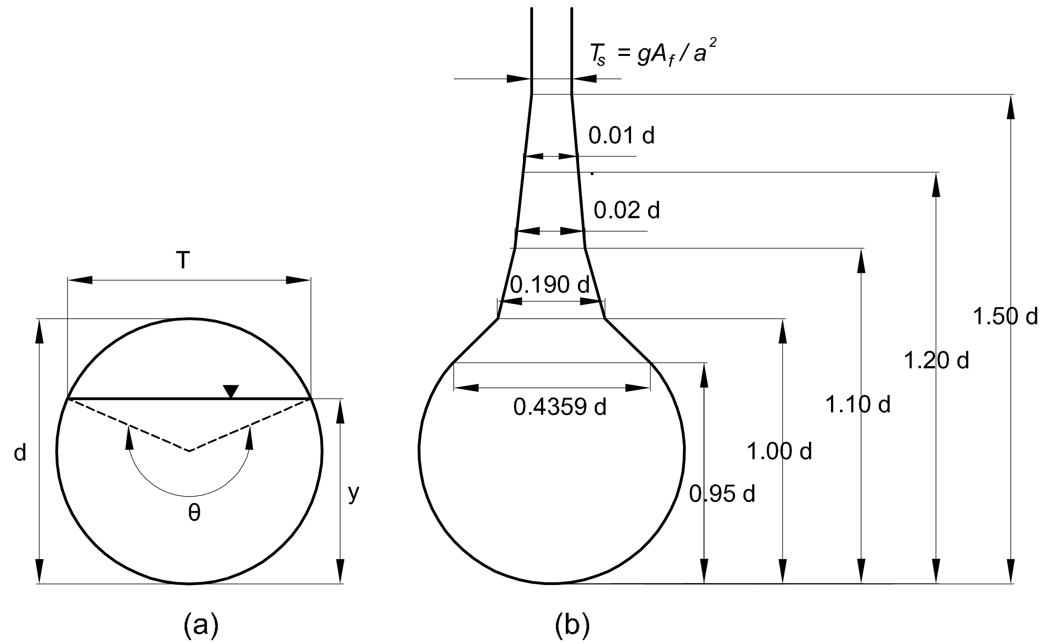

Figure 4.1: (a) Definition of variables in circular cross-sections. (b) Preissmann slot geometry ($y \geq 0.95d$). The drawing is not in scale.

plication of the Rankine-Hugoniot condition to the continuity and momentum equations, these equations are transformed to a frame of reference moving with the left or right wavespeed, depending on the case to be analyzed [Figs. 4.2(c) and 4.2(d)]. By convention, the wavespeed is positive if the wave is traveling downstream and negative otherwise.

The application of the Rankine-Hugoniot condition to the continuity and momentum equations across the left shock, respectively gives

$$M_L = \alpha_\star(u_\star - s_L) = \alpha_L(u_L - s_L) \tag{4.4}$$

$$\alpha_L(u_L - s_L)^2 - \alpha_\star(u_\star - s_L)^2 = \eta_\star - \eta_L \tag{4.5}$$

where $\alpha = \rho A$ and $\eta = A\overline{p}$. Use of M_L [Eq. (4.4)] in Eq. (4.5) gives

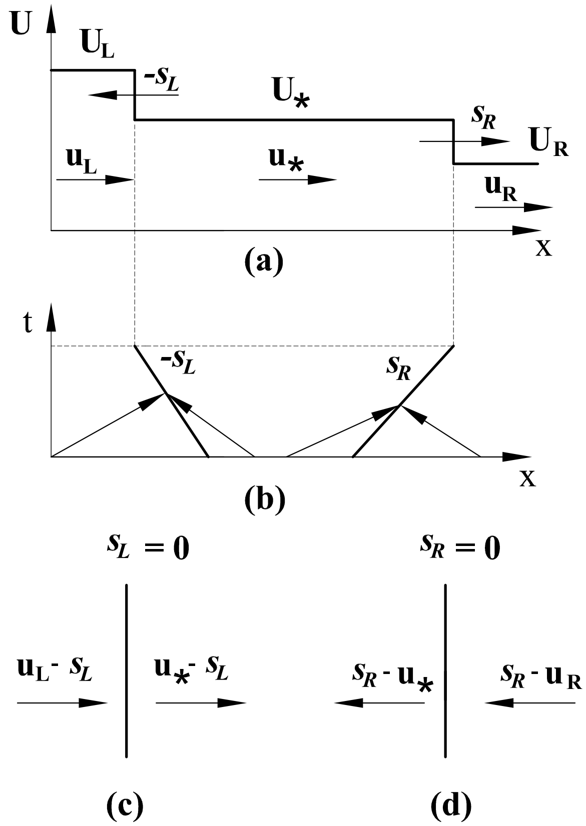

Figure 4.2: (a) Physical space and (b) phase space for the two-shock wave approximation. (c) and (d) transformed frame of references for the left and right shock waves, respectively.

$$M_L = -\frac{\eta_\star - \eta_L}{u_\star - u_L} \tag{4.6}$$

From Eq. (4.4), it is obtained

$$u_\star - u_L = -M_L \frac{\alpha_\star - \alpha_L}{\alpha_\star \alpha_L} \tag{4.7}$$

which can be substituted into Eq. (4.6) to give

$$M_L = \pm\sqrt{\frac{(\eta_\star - \eta_L)\alpha_\star \alpha_L}{\alpha_\star - \alpha_L}} \tag{4.8}$$

To select the root sign of M_L, note in Eq. (4.4) [continuity] that if α_L is greater than $\alpha_\star$, $u_\star$ has to be greater than u_L. Otherwise, $u_\star$ has to be smaller than u_L. Thus, to satisfy Eq. (4.7), the positive root of M_L [Eq. (4.8)] has to be selected. Finally, by plugging the expression for M_L into Eq. (4.4), the following relation for the left shock wavespeed s_L is obtained

$$s_L = u_L - \frac{M_L}{\alpha_L} = u_L - \sqrt{\frac{(\eta_\star - \eta_L)\alpha_\star}{(\alpha_\star - \alpha_L)\alpha_L}} \tag{4.9}$$

A similar expression is obtained for the right shock wavespeed (s_R). The left and right shock wavespeeds are summarized as follows:

$$s_L = u_L - \Omega_L \tag{4.10}$$

$$s_R = u_R + \Omega_R \tag{4.11}$$

where Ω_K $(K = L, R)$ is given by

$$\Omega_K = \sqrt{\frac{(\eta_\star - \eta_K)\alpha_\star}{(\alpha_\star - \alpha_K)\alpha_K}} \tag{4.12}$$

Notice that $\eta_\star (= A_\star \overline{p}_\star)$ is a function of $\alpha_\star$ or viceversa. Thus, only one variable ($\alpha_\star$ or $\eta_\star$) is needed to estimate Ω_K. When $\alpha_\star$ is less or equal than α_K $(K = L, R)$, it is suggested to replace Ω_K $(K = L,\ R)$ with the gravity wave celerity c_K $(K = L, R)$ [see León et al. 2006a]. Following, several estimates for $\alpha_\star$ or equivalently $A_\star$ based on the two-shock wave approximation, the two-rarefaction wave approximation, the linearization of the governing equations, and the depth positivity condition are provided.

Two-shock wave approximation

Eq. (4.7) relates the velocity in the star region $u_\star$ with the velocity in the left region u_L. Another similar equation relates $u_\star$ with the velocity in the right region u_R. These equations may be written as follows:

$$u_\star = u_L - f_L(\alpha_\star, \eta_\star, \alpha_L, \eta_L) \tag{4.13}$$

$$u_\star = u_R + f_R(\alpha_\star, \eta_\star, \alpha_R, \eta_R) \tag{4.14}$$

where f_K $(K = L, R)$ is given by

$$f_K = (\alpha_\star - \alpha_K)\sqrt{\frac{\eta_\star - \eta_K}{(\alpha_\star - \alpha_K)\alpha_\star\alpha_K}} \tag{4.15}$$

By eliminating $u_\star$ from Eqs. (4.13) and (4.14), the following equation, which is a function of one unknown ($\alpha_\star$ is a function of $\eta_\star$ or viceversa), is obtained

$$f(\alpha_\star, \eta_\star) = f_L(\alpha_\star, \eta_\star, \alpha_L, \eta_L) + f_R(\alpha_\star, \eta_\star, \alpha_R, \eta_R) + u_R - u_L = 0 \tag{4.16}$$

In Eq. (4.16), it is more convenient to solve for $y_\star$ than $\alpha_\star$ because both, $\alpha_\star$ and $\eta_\star$ are a function of $y_\star$.

Two-rarefaction wave approximation

Assuming the two-rarefaction wave approximation, the following estimates for the exact solution of $A_\star$ (or $\phi_\star$) and $u_\star$ are obtained:

For $y < 0.95d$ (for derivation details see Chapter 2):

$$u_\star = \frac{u_L + u_R}{2} + \frac{\phi_L - \phi_R}{2} \tag{4.17}$$

$$\phi_\star = \frac{\phi_L + \phi_R}{2} + \frac{u_L - u_R}{2} \tag{4.18}$$

where ϕ is given by (see Chapter 2):

$$\phi = \sqrt{g\frac{d}{8}}\left[\sqrt{3}\,\theta - \frac{\sqrt{3}}{80}\,\theta^3 + \frac{19\sqrt{3}}{448000}\,\theta^5 + \frac{\sqrt{3}}{10035200}\,\theta^7 + \frac{491\sqrt{3}}{27 \times 7064780800}\,\theta^9 + ...\right] \tag{4.19}$$

For $y \geq 0.95d$, the estimates for $A_\star$ and $u_\star$ can be obtained by integrating the differential relationships provided by the generalized Riemann invariants across the two rarefaction waves using the trapezoidal rule. This provides the two following equations that need to be solved by iteration to obtain the estimates of $A_\star$ and $u_\star$:

$$u_L - u_\star + \frac{(c_L + c_\star)(A_L - A_\star)}{A_L + A_\star} = 0 \tag{4.20}$$

$$u_\star - u_R - \frac{(c_\star + c_R)(A_\star - A_R)}{A_\star + A_R} = 0 \tag{4.21}$$

Linearization of governing equations

In this approach, $A_\star$ is obtained by solving the Riemann problem for the linearized hyperbolic system $\partial\mathbf{U}/\partial t + \partial\mathbf{F}(\mathbf{U})/\partial x = 0$ with $\mathbf{F}(\mathbf{U}) \equiv \overline{\mathbf{A}}\mathbf{U}$, $\overline{\mathbf{A}} = \mathbf{A}(\overline{\mathbf{U}})$ and $\overline{\mathbf{U}} \equiv (\mathbf{U}_L + \mathbf{U}_R)/2$. This yields (for derivation details see Chapter 2):

$$A_\star = \frac{A_R + A_L}{2} + \frac{\bar{A}}{2\bar{c}}(u_L - u_R) \tag{4.22}$$

where $\bar{A} = (A_R + A_L)/2$ and $\bar{c} = (c_R + c_L)/2$.

Unlike in the case of the two-rarefaction wave approximation, in the Riemann solver based on the linearization of the governing equations (Eq. 4.22) no iteration is required to estimate $A_\star$.

Depth positivity condition

Another estimate for $A_\star$ that preserves the simplicity of Eq. (4.22) while adding two important new properties may be obtained based on the depth positivity condition (flow depth is greater than or equal to zero). The added properties are (Toro 2001): (1) it can handle situations involving very shallow water well; and (2) unlike the Riemann solver given in Eq. (4.22), the Riemann solver based on the depth positivity condition is found to be very robust in dealing with shock waves. Using this approach, the following estimate for $A_\star$ is obtained that is valid for $y < 0.95d$ (for derivation details see Chapter 2):

$$A_\star = \frac{A_R + A_L}{2}\left(1 + \frac{u_L - u_R}{\phi_R + \phi_L}\right) \tag{4.23}$$

In the *modified Preissmann model*, for $y < 0.20d$, the Riemann solver based on the depth positivity condition is used. For $0.20d \leq y < 0.80d$, the two-shock wave approximation is applied, and for $y \geq 0.80d$, the Riemann solver based on linearization of the governing equations is utilized.

The incorporation of source terms into the solution and the stability constraints for the *modified Preissmann model* are the same as free surface flows (see Chapter 2).

4.3.3 Boundary conditions

In this section, a single set of equations (free surface flow) is used for the modeling of free surface and pressurized flows. Thus, the boundary conditions used are equivalent to those used in free surface flows.

In the Godunov approach, for the order of accuracy of the numerical solution to be preserved, it is necessary to use the same order of reconstruction of the flow variables in all the cells. Since common procedures of reconstruction such as MUSCL use one or more cells on each side of the cell to be reconstructed, generally one or more cells are missing within the first and last cells of the computational domain. In the model proposed in this thesis (both frameworks), second-order accurate boundary conditions are implemented using ghost cells outside of the boundaries (see Chapter 3 for implementation details).

In a typical storm-sewer system, various types of boundaries are present. These may include dropshafts, reservoirs, junctions, dead ends, control gates, pumping stations, etc. In this section, only a three-way junction is described. Several boundaries are special cases of the three-way junction boundary. For instance, a dropshaft boundary is a special case of the three-way junction boundary with no inflow pipes. A downstream reservoir boundary also is a special case of the three-way junction boundary with one inflow pipe and no outflow pipe.

Three-way junction boundary

In this type of boundary (Fig. 4.3), seven variables are unknown, namely, the water depth and the flow velocity at each pipe boundary, and the flow depth at the dropshaft pond. Thus, seven equations are needed in order to determine the unknown variables. The three first equations can be obtained by applying the Rankine-Hugoniot conditions between each pipe boundary and the first cell of the corresponding pipe adjacent to the dropshaft. This formulation is intrinsically conservative (mass and momentum are conserved), and no special treatment in presence of shocks at the boundary is required. This yields:

$$(u_{b_1}^{n+1} - u_1^n)^2 - \frac{(\eta_{b_1}^{n+1} - \eta_1^n)}{\rho} \frac{(A_{b_1}^{n+1} - A_1^n)}{A_{b_1}^{n+1} A_1^n} = 0 \tag{4.24}$$

$$(u_{b_2}^{n+1} - u_2^n)^2 - \frac{(\eta_{b_2}^{n+1} - \eta_2^n)}{\rho} \frac{(A_{b_2}^{n+1} - A_2^n)}{A_{b_2}^{n+1} A_2^n} = 0 \tag{4.25}$$

$$(u_{b_3}^{n+1} - u_3^n)^2 - \frac{(\eta_{b_3}^{n+1} - \eta_3^n)}{\rho} \frac{(A_{b_3}^{n+1} - A_3^n)}{A_{b_3}^{n+1} A_3^n} = 0 \tag{4.26}$$

where the subscript b_k ($b_k = b_1$, b_2 and b_3) refers to the pipe boundary, and the subscript j (j = 1, 2 and 3) refers to the corresponding adjacent cell to the boundary. When the flow at the junction changes smoothly and no shocks are present, the theory of Riemann invariants (see León et al. 2006a) is used instead of the Rankine-Hugoniot conditions for numerical stability reasons. The fourth equation can be obtained from the mass balance at the dropshaft,

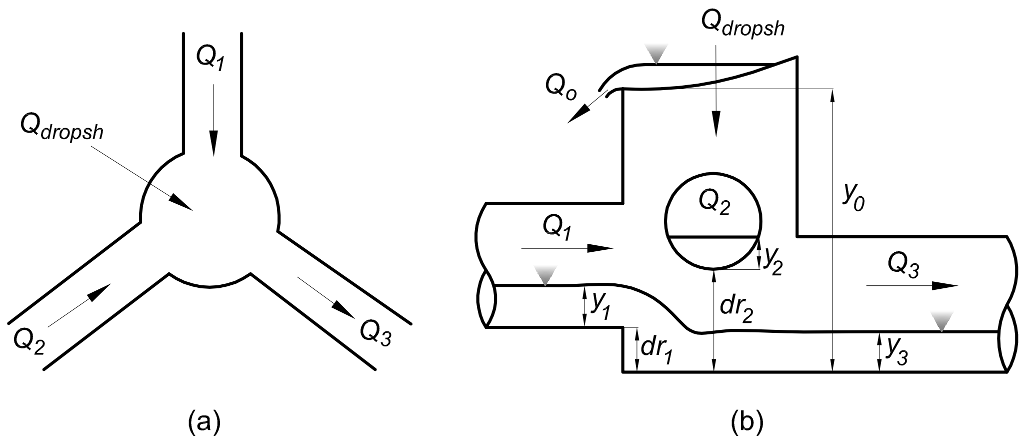

Figure 4.3: Schematic of reservoir junction with overflow structure. (a) Plan view, (b) Profile.

$$\frac{(Q^{n+1}_{dropsh} + Q^{n}_{dropsh})}{2} - \frac{(Q^{n+1}_{0} + Q^{n}_{0})}{2} + \frac{(Q^{n+1}_{b_1} + Q^{n}_{b_1})}{2} + \frac{(Q^{n+1}_{b_2} + Q^{n}_{b_2})}{2} - \frac{(Q^{n+1}_{b_3} + Q^{n}_{b_3})}{2} = A_{dropsh}\frac{dE_3}{dt} \quad (4.27)$$

where E_3 is the specific energy of the outflow and Q_0 is the overflow discharge. If the dropshaft has a relatively small storage capacity in comparison to the flow, the right-side of Eq. (4.27) can be omitted. The specific energy of the outflow is given by

$$E_3 = y_3 + \frac{u^2_{b_3}}{2g} \quad (4.28)$$

The overflow discharge can be obtained as follows: $Q_0 = 0$, if $ydropsh \leq y_0$, and $Q_0 = CB(ydropsh - y_0)^{3/2}$, if $ydropsh > y_0$, in which C = weir discharge coefficient and B = weir length.

The fifth and sixth equations can be obtained by replacing the energy equations by the "kinematic compatibility condition" for the depths (e.g., Pagliara and Yen 1997, Yen 1986, 2001):

For subcritical flow:

$$\begin{aligned} y_j &= y_{c_j} && \text{if } dr_j + y_{c_j} > y_3 \\ dr_j + y_j &= y_3 && \text{otherwise} \end{aligned} \tag{4.29}$$

for $j = 1, 2$, where y_{c_j} is the critical depth.

For supercritical flow:

$$\begin{aligned} y_j &= y_{u_j} && \text{if } dr_j + y_{u_j} > y_3 \\ dr_j + y_j &= y_3 && \text{otherwise} \end{aligned} \tag{4.30}$$

for $j = 1, 2$, where y_{u_j} is the uniform flow depth corresponding to the instantaneous flow discharge Q_j.

The seventh equation is obtained by applying the energy equation between the dropshaft and the outflow pipe (pipe 3). This yields:

$$y_{dropsh}^{n+1} = y_{b_3}^{n+1} + (1 + K_u)\frac{u_{b_3}^2}{2g} \tag{4.31}$$

where K_u is the loss coefficient.

4.4 Shock-tracking-capturing model

4.4.1 Governing equations

The one-dimensional open-channel and compressible water hammer flow continuity and momentum equations for prismatic conduits may be written in their vector conservative form and in a compatible format as follows:

$$\frac{\partial \mathbf{U}}{\partial t} + \frac{\partial \mathbf{F}}{\partial x} = \mathbf{S} \tag{4.32}$$

where the vector variable $\mathbf{U}$, the flux vector $\mathbf{F}$ and the source term vector $\mathbf{S}$ for open-channel flows may be written as (e.g., León et al. 2006a):

$$\mathbf{U} = \begin{bmatrix} \rho A \\ \rho Q \end{bmatrix}, \mathbf{F} = \begin{bmatrix} \rho Q \\ \rho \frac{Q^2}{A} + A\overline{p} \end{bmatrix} \text{ and } \mathbf{S} = \begin{bmatrix} 0 \\ (S_0 - S_f)\rho g A \end{bmatrix} \tag{4.33}$$

and for compressible water hammer flows as (e.g., Guinot 2003):

$$\mathbf{U} = \begin{bmatrix} \mu \\ Q_m \end{bmatrix}, \mathbf{F} = \begin{bmatrix} Q_m \\ \frac{Q_m^2}{\mu} + A_f p \end{bmatrix} \text{ and } \mathbf{S} = \begin{bmatrix} 0 \\ (S_0 - S_f)\rho_f g A_f \end{bmatrix} \tag{4.34}$$

where the variables for the free surface flow are: $A =$ cross-sectional area of the flow; $Q =$ flow discharge; $\overline{p} =$ average pressure of the water column over the cross sectional area; $\rho =$ liquid density that for free surface flows is assumed to be constant but not for pressurized flows; $g =$ gravitational acceleration; $S_0 =$ slope of the bottom channel; and $S_f =$ slope of the energy line, which may be estimated using the Manning's formula, the Darcy-Weisbach equation or any other formulation. The approach proposed in this section is applicable to any prismatic conduit, however in the rest of this section, only a circular cross-section conduit is considered.

The variables for the compressible water hammer flow are: $A_f =$ full cross-sectional area of the conduit, $p =$ pressure acting on the center of gravity of the full cross-sectional area of the conduit, $Q_m =$ mass discharge and $\mu =$ mass of fluid per unit length of conduit. Denoting the fluid density for compressible water hammer flows by ρ_f, the mass per unit length can be expressed as $\mu = \rho_f A_f$ and the mass discharge as $Q_m = \mu u = \rho_f A_f u$. As in the case of open-channel flows, the slope of the energy line S_f may be estimated using the Manning's formula, the Darcy-Weisbach equation or any other formulation.

The Eq. (4.32) for waterhammer flows does not form a closed system in that the flow is described using three variables: μ, p and Q_m. However, it is possible to eliminate the pressure variable by introducing the definition of the pressure wave celerity a, which relates p and μ:

$$a = \left[\frac{d(A_f p)}{d\mu}\right]^{1/2} \tag{4.35}$$

In Eq. (4.35), a is constant (single-phase flow) and is assumed to be known. This variable can be computed using the following relation that is derived from classical structural mechanics (e.g., Wylie and Streeter 1993):

$$a = \left[\frac{k_f/\rho_f}{1 + \frac{k_f}{E}\frac{d}{e}}\right]^{1/2} \tag{4.36}$$

where d is the pipe diameter, e is its thickness, E is Young's modulus of elasticity of the pipe material and k_f is the compressibility of the fluid in the pipe.

Integrating the differentials $d\mu$ and dp (A_f is assumed to be constant) in Eq. (4.35) leads to the following equation that relates p and μ:

$$A_f p = A_f p_{ref} + a^2(\mu - \mu_{ref}) \tag{4.37}$$

where p_{ref} is the reference pressure, and $\mu_{ref} = A_f \rho_{ref}$. The pressure as a function of μ is readily obtained from Eq. (4.37).

In free surface flows, the gravity wavespeed c is given by $c = \sqrt{gA/T}$ where T is the topwidth of the flow. According to this relation, the gravity wavespeed is unbounded as the water depth approaches the crown of the conduit. When the water depth approaches the crown of the conduit; the pressure wave and not the gravity wave should become the primary mode of propagation of a disturbance. Therefore, a small length, ϵ, as proposed by Song et al. (1984) is introduced such that the phase change from free surface to pressurized flow is considered to occur when the depth exceeds $d-\epsilon$. At this threshold condition ($y = d - \epsilon$), the fluid density, the hydraulic area and the average pressure in both open-channel and pressurized flow regime have to be the same. This threshold state is selected as the reference condition for the pressurized flow variables in Eq. (4.37). At the threshold state, the reference area (A_{ref}) is the hydraulic area below $y = d - \epsilon$ so that A_f in the previous equations is replaced with A_{ref}. In the proposed model ϵ is chosen to be 2% of the pipe diameter, which results in a reduction of the hydraulic area of less than 1%. The reference density considered ρ_{ref} is 1000 kg/m^3 that corresponds to clean water at a temperature of 4 degrees Celsius.

4.4.2 Differences between free surface and pressurized flows and their implications for modeling mixed flows

Although the governing equations from free surface and pressurized flows are similar, the characteristics of these type of flows have a marked difference.

One important distinction between these flows is the ability of pressurized flows to sustain sub-atmospheric pressures. After a given node has been pressurized, free surface flow is not necessarily generated at this node when its head drops below the pipe crown. The additional and necessary condition to depressurize this node is that at least one of the surrounding nodes is in free surface flow regime. When a pipe system has been fully pressurized, the only way to start the depressurization process is through ventilated boundaries (e.g., dropshafts, reservoirs, etc.).

Another important difference is that in pressurized flows a disturbance is propagated at a speed that is two orders of magnitude faster than in free surface flows. A moving interfacial boundary separates the two flow regimes. Cardle (1984) defined an open channel-pressurized flow interface as positive if it is moving towards the open-channel flow (Fig. 4.4), and negative or retreating if it is moving towards the region of pressurized flow (Fig. 4.5). The change in direction of the interface from positive to negative or vice versa is called "*interface reversal*" (Fig. 4.6).

4.4.3 Formulation of finite volume Godunov-type schemes

The proposed shock-tracking-capturing approach is incorporated within a finite volume framework that is described in Chapters 2 and 3. As mentioned in the previous section, the Riemann problem is solved using the HLL Riemann solver that is also described in Chapters 2 and 3. For this Riemann solver the wavespeeds need to be determined. Following, an estimate for wavespeeds using the two-shock wave approximation is derived.

Define:

$$\alpha = \begin{cases} \rho A & \text{for open-channel flows} \\ \mu = \rho_f A_f & \text{for pressurized flows} \end{cases} \tag{4.38}$$

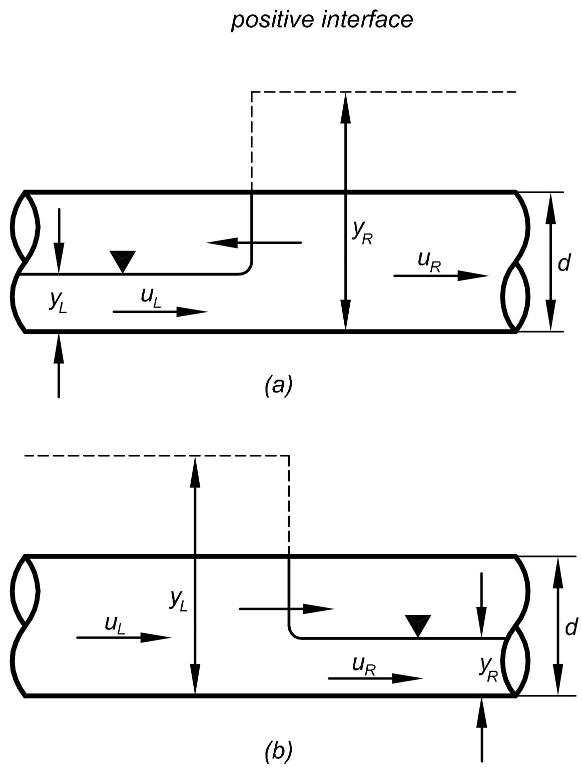

Figure 4.4: Positive interfaces (a) moving in the upstream direction (e.g., generated by sudden total closure of a gate downstream) (b) moving in the downstream direction (e.g., created when the inflow rate exceeds the capacity of the pipe or tunnel somewhere upstream).

and

$$\eta = \begin{cases} A\overline{p} & \text{for open-channel flows} \\ A_f p & \text{for pressurized flows} \end{cases} \tag{4.39}$$

where α and η represent the mass of fluid per unit length of pipe and the pressure force over the cross sectional area, respectively.

Figs. 4.2(a) and 4.2(b) illustrate the physical space and phase space for the two-shock wave approximation, respectively. In order to facilitate the application of the Rankine-Hugoniot condition to the continuity and momentum equations, these equations are transformed to a frame of reference moving with the left or right wavespeed, depending on the case to be analyzed [Figs. 4.2(c)

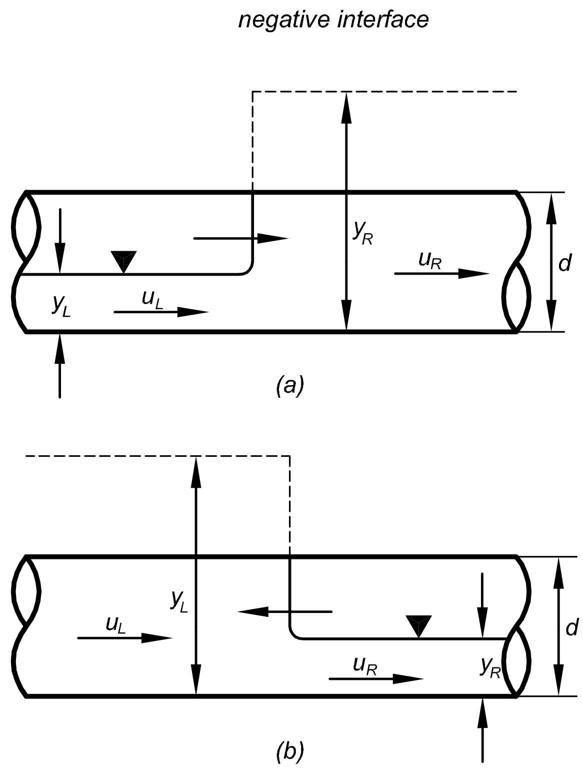

Figure 4.5: Negative interfaces (a) moving in the downstream direction (e.g., generated by the sudden partial closure of a gate (from above) somewhere upstream) (b) moving in the upstream direction (e.g., generated by depressurization at the downstream end of the system).

and 4.2(d)]. By convention, the wavespeed is positive if the wave is traveling downstream and negative otherwise.

The application of the Rankine-Hugoniot condition to the continuity and momentum equations across the left shock, respectively gives

$$M_L = \alpha_\star(u_\star - s_L) = \alpha_L(u_L - s_L) \tag{4.40}$$

$$\alpha_L(u_L - s_L)^2 - \alpha_\star(u_\star - s_L)^2 = \eta_\star - \eta_L \tag{4.41}$$

Use of M_L (Eq. 4.40) in Eq. (4.41) gives

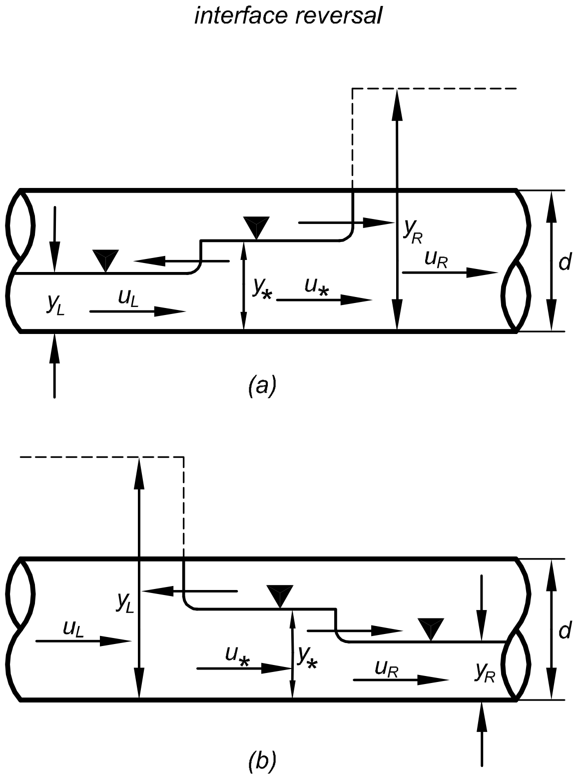

Figure 4.6: Interface reversal (a) positive interface moving upstream transformed into an open-channel surge and a negative interface (b) positive interface moving downstream transformed into an open-channel surge and a negative interface.

$$M_L = -\frac{\eta_\star - \eta_L}{u_\star - u_L} \tag{4.42}$$

From Eq. (4.40), it is obtained

$$u_\star - u_L = -M_L \frac{\alpha_\star - \alpha_L}{\alpha_\star \alpha_L} \tag{4.43}$$

which can be substituted into Eq. (4.42) to give

$$M_L = \pm \sqrt{\frac{[\eta_\star - \eta_L][\alpha_\star \alpha_L]}{\alpha_\star - \alpha_L}} \tag{4.44}$$

The left shock wavespeed s_L can be obtained from Eq. (4.40) that gives

$$s_L = u_L - \frac{M_L}{\alpha_L} \tag{4.45}$$

Note that the positive root of M_L in Eq. (4.44) has to be chosen to satisfy Eq. (4.43). A similar expression is obtained for the right shock wavespeed (s_R).

The left and right shock wavespeeds are summarized as follows:

$$s_L = u_L - \Omega_L \tag{4.46}$$

$$s_R = u_R + \Omega_R \tag{4.47}$$

where Ω_K $(K = L, R)$ is given by

$$\Omega_K = \sqrt{\frac{[\eta_\star - \eta_K][\alpha_\star]}{[\alpha_\star - \alpha_K][\alpha_K]}} \tag{4.48}$$

Notice that $\eta_\star$ is a function of $\alpha_\star$ or viceversa. Thus, only one variable ($\alpha_\star$ or $\eta_\star$) is needed to estimate Ω_K in Eq. (4.48). Following, an estimate for $\alpha_\star$ based on the two-shock wave approximation is derived.

Eq. (4.43) relates the velocity in the star region $u_\star$ with the velocity in the left region u_L. Another similar equation relates $u_\star$ with the velocity in the right region u_R. These equations may be written as follows:

$$u_\star = u_L - f_L(\alpha_\star, \eta_\star, \alpha_L, \eta_L) \tag{4.49}$$

$$u_\star = u_R + f_R(\alpha_\star, \eta_\star, \alpha_R, \eta_R) \tag{4.50}$$

where f_K $(K = L, R)$ is given by

$$f_K = (\alpha_\star - \alpha_K)\sqrt{\frac{\eta_\star - \eta_K}{(\alpha_\star - \alpha_K)\alpha_\star\alpha_K}} \tag{4.51}$$

By eliminating $u_\star$ from Eqs. (4.49) and (4.50), the following equation, which is a function of one unknown ($\alpha_\star$ is a function of $\eta_\star$ or viceversa), is obtained

$$f(\alpha_\star, \eta_\star) = f_L(\alpha_\star, \eta_\star, \alpha_L, \eta_L) + f_R(\alpha_\star, \eta_\star, \alpha_R, \eta_R) + u_R - u_L = 0 \tag{4.52}$$

The star region may be in either open-channel or pressurized flow regime. For the case when the star region is in open-channel flow regime, it is more convenient to solve for $y_\star$ than $\alpha_\star$ because both, $\alpha_\star$ and $\eta_\star$ are a function of $y_\star$.

The HLL Riemann solver allows all possible open channel-pressurized flow interfaces, including interface reversals to be handled automatically. This is a remarkable advantage of Riemann-based methods over other approaches such as the shock-fitting model of Song et al. (1984), in which a different set of equations needs to be formulated and solved for each type of open channel-pressurized flow interface.

4.4.4 Boundary conditions

For the shock-tracking-capturing framework, solely boundary conditions for a single pipe are implemented in this thesis. In this case, two variables are unknown at each boundary of the pipe, namely, the water depth (or hydraulic area) and the flow velocity (or flow discharge). One of the variables is specified and the other is computed using the Rankine-Hugoniot conditions (Eq. 4.24). The Rankine-Hugoniot conditions can be applied indistinctively to free surface or pressurized flows.

4.4.5 Shock-tracking-capturing method for open channel pressurized flow interfaces

The approach we pursue herein is in some degree similar to the approach proposed by LeVeque and Shyue (1995) and Langseth (1996). These authors applied shock-tracking in conjunction with shock capturing methods to solve several problems in gas dynamics with good success.

As was mentioned earlier, in this framework, both free surface and pressurized flows are handled using shock-capturing methods. These methods were described in Chapters 2 and 3. Open channel-pressurized flow interfaces are treated using a shock-tracking-capturing approach. In this approach, cell boundaries are introduced at the location of open channel-pressurized flow interfaces, subdividing some regular cells into two subcells, resulting in a mesh arrangement that varies from one time step to the next. However, the vast majority of grid cells do not vary.

In a finite volume representation, the value of each grid cell represents the average value of the solution over that grid cell. By having a cell boundary at each open channel-pressurized flow interface, we avoid the smearing and loss of accuracy that is inevitable when the discontinuity falls within a grid cell and the discrete solution must be averaged over the cell. The Riemann solution gives, in particular, information about the propagation speed of the tracked interfaces that is used to determine the grid at the next time step. Once the new grid has been determined, the shock-capturing method takes essentially the same form on both regular and irregular cells. An apparent difficulty with this approach is the fact that the discontinuity may fall close to a cell boundary of the underlying grid. This is handled by eliminating some regular cell boundaries to maintain a lower bound on the cell size. Also the tracked interface may pass more than one cell if the neighboring cells are small. This also may be handled by eliminating cell boundaries that fall within the location of the tracked interfaces at the old and new time step.

When two open channel-pressurized flow interfaces are going to interact, the time step is adjusted in such a way that the collision of these interfaces occurs exactly at the end of the time step. Following, the procedure for the treatment of open channel-pressurized flow interfaces is described. This procedure is also presented in the form of a flow chart, which is shown in Fig. 4.7.

1. The approach begins by solving the Riemann problem at each open channel-pressurized flow interface. This allows the computation of the speeds of the waves to be tracked (two if the initial interface is within the limits of the star region and one otherwise). If two waves arise after solving the Riemann problem, the intermediate state may be in open-channel or pressurized flow regime. In any case, this means that only one open channel-pressurized flow interface can be generated after the solution of the Riemann problem. If there is a second wave (which will not be an open channel-pressurized flow discontinuity), there is no necessity of tracking this wave because the shock-capturing scheme, which is used for free surface and pressurized flows alone, will capture this wave automatically.

2. The time step for the simulation is obtained using the Courant num-

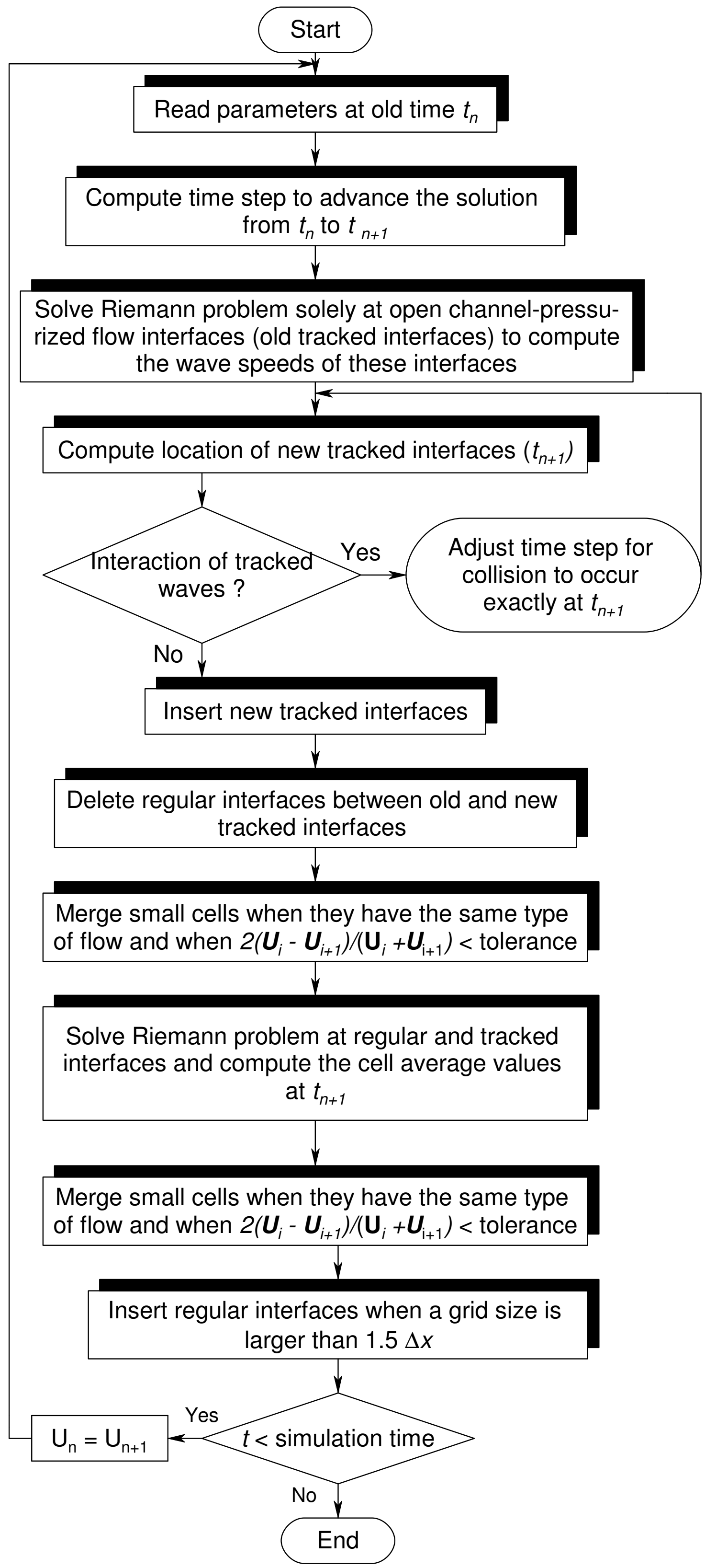

Figure 4.7: Flow chart for the proposed shock tracking-capturing algorithm.

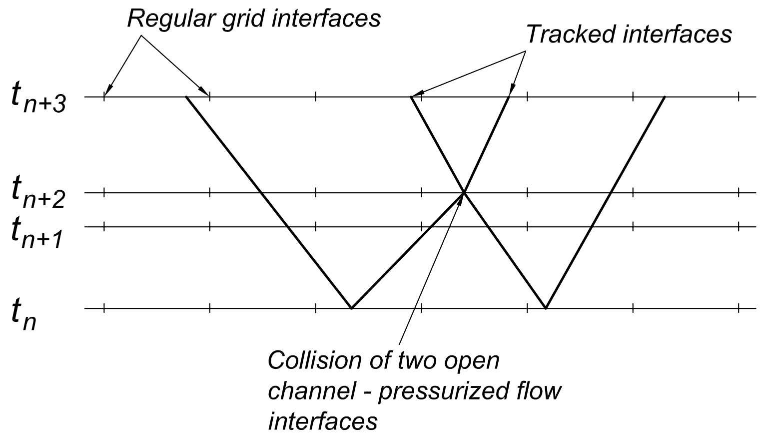

Figure 4.8: Phase space of tracked interfaces.

ber criteria for the open-channel and pressurized flow. In order to avoid the interaction of tracked waves, the time step is adjusted if needed. It will be adjusted in such a way that the collision of two tracked waves occurs exactly at the end of the time step (Fig. 4.8). This can be accomplished by selecting the minimum of the collision times of all tracked waves.

3. After determining the time step Δt, the locations of each tracked wave at the end of the time step are computed. Some of these locations may coincide if two waves collide or if the new locations are exactly at the old grid interfaces. For each distinct wave location in the domain, a new cell interface is inserted into the old grid. Each new interface subdivides some cells into two subcells. A cell value must be assigned to each of these subcells. The simplest approach is to assign the previous cell value to each subcell.

4. Once the new grid is constructed, the cell average values U are then updated by using Eq. (2.5). Since the new grid has been chosen carefully so that all open channel-pressurized flow interfaces are propagated exactly to cell boundaries, there is no smearing of the tracked waves during the averaging process. The tracked waves may propagate through one or more regular cells making necessary temporary deletion of some regular interfaces.

5. In the new grid, small cells are merged if the following criteria is satisfied: (a) the flow regime of the cells to be merged is the same (free surface or pressurized flow); (b) the absolute value of the relative difference of a given characteristic variable of the flow is less than a specified tolerance (for instance TOL $\leq 5\%$). For free surface flows, if the hydraulic area is considered as the characteristic variable, the following additional relation have to be satisfied to merge two adjacent small cells

$$\left\| \frac{2(A_i - A_{i+1})}{A_i + A_{i+1}} \right\| \leq \text{TOL} \tag{4.53}$$

Likewise, in pressurized flows, if the equivalent height of water, given by $h = p/(\rho g) + d/2$ is used as the characteristic variable, the following additional condition have to be satisfied to merge two small cells

$$\left\| \frac{\frac{a^2}{A_f}(\mu_i - \mu_{i+1})}{\frac{\rho g d}{2} + p_{ref} - \frac{a^2}{A_f}\mu_{ref} + \frac{a^2}{2A_f}(\mu_i + \mu_{i+1})} \right\| \leq \text{TOL} \tag{4.54}$$

The cell value in the combined cell is calculated by the weighted combination of the merged subcells to maintain the correct cell average. For instance, in Fig. 4.9, the old tracked interface located at x_ξ is deleted from the new grid (t_{n+1}) that results in the following cell value for the ith combined cell:

$$U_i^{n+1} = \frac{x_\xi - x_a}{x_b - x_a} U_{i_a}^{n+1} + \frac{x_b - x_\xi}{x_b - x_a} U_{i_b}^{n+1} \tag{4.55}$$

where $U_{i_a}^{n+1}$ and $U_{i_b}^{n+1}$ are the cell averages in the first and second subcell of the ith cell respectively, and $x_b - x_a$ is the underlying fixed mesh size.

Conversely to the merging of small cells, when the grid size is larger than

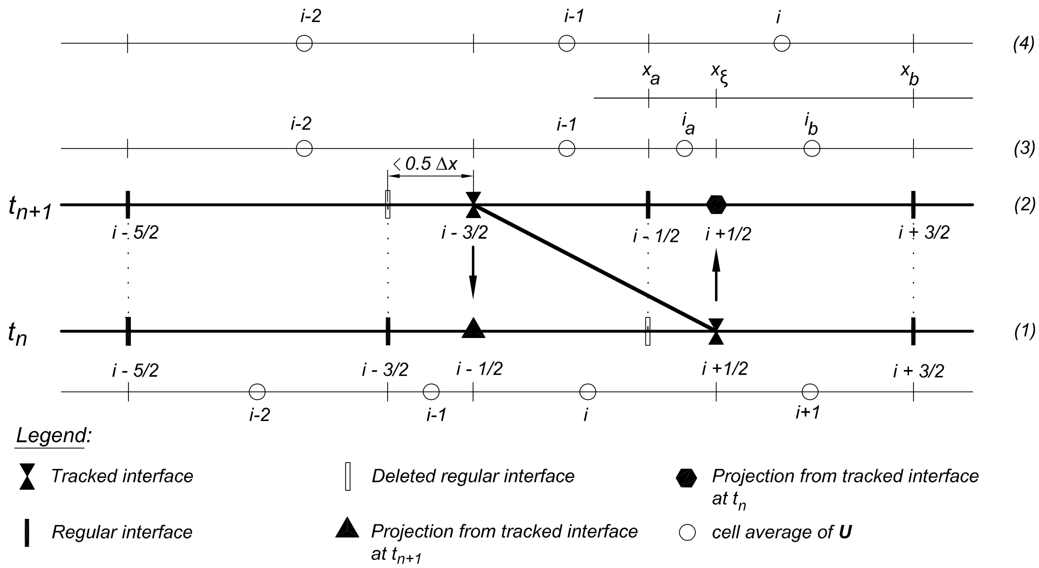

Figure 4.9: Elimination of old tracked interfaces and merging of cells. (1) and (2) location of interfaces at old and new time, respectively, (3) and (4) cells at new time before and after deleting the old tracked interface, respectively.

1.5 times the regular grid size, regular interfaces are inserted within the larger grids.

6. Repeat the process until the specified time of simulation is achieved.

4.5 Treatment of dry bed flows

The HLL approach offers a simple way of dealing with dry fronts. This Riemann solver has numerical flux as given by Eq. (2.18), which in turn requires wavespeed estimates s_L and s_R. If a dry bed exists upstream or downstream of a cell interface, the governing equations are not strictly hyperbolic and the two eigenvalues of the Jacobian matrix of $\mathbf{F}$ with respect to $\mathbf{U}$ collapse into one (e.g., Zoppou and Roberts 2003). Under these circumstances, no shock exists and s_L and s_R represents the speed of the head or toe of the rarefaction wave, depending if the dry bed is present upstream ($y_L = 0$) or downstream ($y_R = 0$). In this case, the wavespeeds may be determined exactly, yielding for the case of sewers (the derivation of the wavespeeds for the case of sewers is similar to the presented by Toro 2001 for rectangular cross-sections):

If $y_L = 0$:

$$\begin{aligned} s_L &= u_R - \phi_R \\ s_R &= u_R + c_R \end{aligned} \tag{4.56}$$

If $y_R = 0$:

$$\begin{aligned} s_L &= u_L - c_L \\ s_R &= u_L + \phi_L \end{aligned} \tag{4.57}$$

where c is the gravity wave celerity.

4.6 Evaluation of the model

The purpose of this section is to evaluate the accuracy, numerical efficiency and robustness of the formulated models in modeling transient mixed flows in storm-sewers. The first two test cases compare simulation results to laboratory measurements of transient mixed flows. The third test case compare simulation results to "Near-exact solutions" of transient mixed flows at field scale. The last test case in this section is designed to investigate the ability of the formulated models in simulating pressurized flow transients. This last test compare simulation results to "Near-exact solutions" of pressurized flow transients at field scale.

4.6.1 Experiments type A of Trajkovic et al. (1999)

In this test case, the proposed schemes are used to reproduce a set of experiments conducted at the Hydraulics Laboratory of University of Calabria by

Trajkovic et al. (1999). The experimental setup consisted of a perspex pipe ($n_m = 0.008$) about 10 m long, having an inner diameter of 10 cm. Upstream and downstream tanks were connected to the pipe with automatic sluice gates. The experimental investigations evaluated the effect of rapid changes in the opening or closing of the sluice gates. Acknowledging the possible interference of the air phase in case the pipe became pressurized, several vents were placed at the top of the pipe.

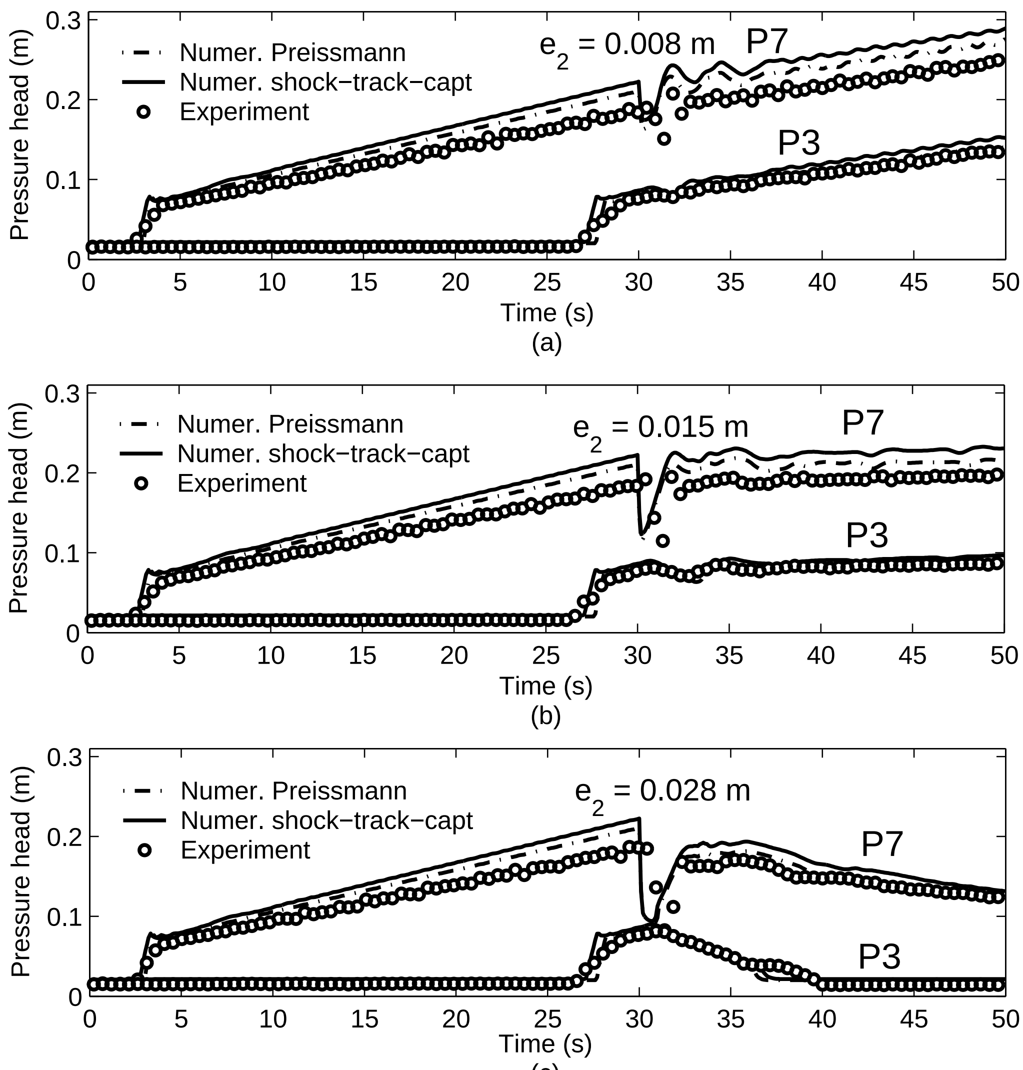

Figure 4.10: Measured and computed piezometric levels in sections P3 and P7 for three different downstream valve reopenings (e_2). (a) $e_2 = 0.008m$, (b) $e_2 = 0.015m$, (c) $e_2 = 0.028m$.

In this test case, the type A set of experiments of Trajkovic et al. (1999) is considered. The initial conditions for this set of experiments were inflow rate constant at 0.0013 m^3/s, the bed slope at 2.7%, the upstream sluice gate opened $e_1 = 0.014$ m, and the downstream sluice gate totally opened. The transient flow was generated after a rapid (but not instantaneous) closure of the downstream sluice gate that caused the formation of a filling bore moving upstream. After 30 seconds of the gate closure, the gate was partially reopened, producing another transient phenomena. Different values for the reopening (e_2) were tested. In this test case, three values for the reopening are considered: $e_2 = 0.008$ m, $e_2 = 0.015$ m, and $e_2 = 0.028$ m. Simulated and measured pressure traces in sections P3 and P7 for the three reopenings are shown in Fig. 4.10. The sections P3 and P7 were located 4.6 m and 0.6 m upstream from the downstream sluice gate, respectively. The simulated pressure traces were generated using 80 cells and a $Cr = 0.40$ for the *modified Preissmann model*. For the shock-tracking-capturing model, the initial number of cells and Courant number used were the same as the *modified Preissmann model*. However, at the end of the simulation (50 s), the number of cells in the mesh was 82. This is because in the shock-tracking-capturing model, the mesh arrangement may vary from one time step to the next.

As can be observed in Figs. 4.10 (a), 4.10 (b), and 4.10 (c), the simulated pressure traces have a good agreement with the experimental measurements. In particular, the formation of the filling bore and its velocity of propagation are accurately reproduced. However, all the computed shock fronts (both models) are steeper than the measured ones. This is because in the experiments the closing and partial reopening of the gate was very rapid, but not instantaneous, as was assumed in the simulations. The instantaneous gate closure assumption in the simulations also caused slightly higher pressure heads as compared to the experimental results. These figures also show that the pressure traces simulated using the *modified Preissmann model* are slightly smaller than those produced using the shock-tracking-capturing model. This may be because the pipe-slot has more capacity to store mass (due to the gradual transition between the pipe and the slot) than the shock-tracking-capturing model.

As is shown in Figs. 4.10 (a), 4.10 (b), and 4.10 (c), almost immediately after the reopening of the downstream gate ($t = 30\ s$), a small drop in the pressure head was observed and computed. For a reopening of 0.008 m [Fig. 4.10 (a)], after a small drop in the pressure head, the pressure head continuously increased in all sections. This is because the outflow from the pipe was smaller than the inflow. For a reopening of 0.015 m [Fig. 4.10 (b)], a stationary hydraulic jump was observed and computed in the pipe after the drop in the pressure head. For the reopening of 0.028 m [Fig. 4.10 (c)], the hydraulic jump traveled downstream, because the outflow was greater than the inflow.

It is interesting to note that Trajkovic et al. (1999), using the Preissmann approach and solving the governing equations utilizing a shock-capturing scheme, as used in our *modified Preissmann model*, reported numerical instabilities in their simulations when the reopening was 0.015 m or greater. Numerical instabilities were reported by these authors even though the slot width they used was as large as 10% of the pipe diameter. When using the Preissmann approach, as the ratio between the slot width and the diameter increases, the mass and momentum conservation errors also increases. Furthermore, as is shown in the last test case of this chapter, when using a wide slot there is no hope that pressurized transients are well simulated. The only way of reproducing the correct propagation and interaction of pressurized transients is by choosing a slot width so that the speed of gravity waves in the slot is equal to the water hammer wavespeed. This criteria is used in the *modified Preissmann model* to determine the slot width. Although this criteria results in very small slot widths, no stability problems were observed when using the *modified Preissmann model*.

The most important differences between our *modified Preissmann model* and that of Trajkovic et al. (1999) are: (1) unlike the Trajkovic model, in our model, a slope limiter (MINMOD) is used to preserve the monotonicity of the solution and to control oscillations that may be present around open channel-pressurized flow shock interfaces, and (2) in contrast to the Trajkovic model, in our model, a gradual transition between the pipe and the slot is introduced. Thus, it seems that the advantage of our *modified Preissmann model* with respect to that of Trajkovic et al. (1999) is because of these two considerations.

4.6.2 Trial J of Cardle (1984)

In this test case, the ability of the proposed models to simulate a positive shock interface (an interface is defined to be positive when it is moving from the pressurized flow region toward the open-channel flow region, and negative otherwise) reversing direction and becoming a negative interface is tested, by comparing the results of the proposed models against experimental measurements conducted at the St. Anthony Falls Laboratory of the University of Minnesota. These experiments were reported in a number of publications including Cardle (1984), which was used in the preparation of this chapter. The experimental setup consisted of a 48.77 m long clear PVC pipe, having an inner diameter of 16.26 cm. An upstream head tank and a downstream reservoir were connected to the pipe with automatic sluice gates. Many different flow conditions could be established in this system by manipulation of the gates and inflow valve.

In this test case, the trial J experiment of Cardle (1984) is considered. The initial conditions for this experiment were inflow rate constant at 0.005097 m^3/s, the bed slope at 0.05%, the initial downstream reservoir depth at 0.1372 m, and the initial flow depth 30.48 m from downstream end at 0.1372 m. The Manning roughness value suggested by Cardle (1984) and used in our simulations was 0.011. The transient flow was produced after a rapid closure of the downstream gate, that created a positive interface moving upstream. When this interface advanced 24.4 m, the gate was instantly reopened. This caused the interface to reverse direction and retreat back downstream. When the gate was reopened, a second negative interface formed at the downstream end of the system and moved upstream.

The simulated and measured pressure heads at transducer P1, which is located at 9.14 m upstream from the downstream end, are presented in Fig. 4.11. The simulated pressure trace was generated using 100 cells and a $Cr = 0.50$ for the *modified Preissmann model*. For the shock-tracking-capturing model, the initial number of cells and Courant number used were the same as the *modified Preissmann model*. In the former model, at the end of the simulation (50 s), the number of cells in the mesh was 105. In the simulations, the downstream gate was instantaneously reopened at 15 s after the gate was closed. After the gate was reopened, the positive interface continued to move upstream propelled by its own inertia. Meanwhile, a negative interface was formed at the downstream boundary and started to move upstream.

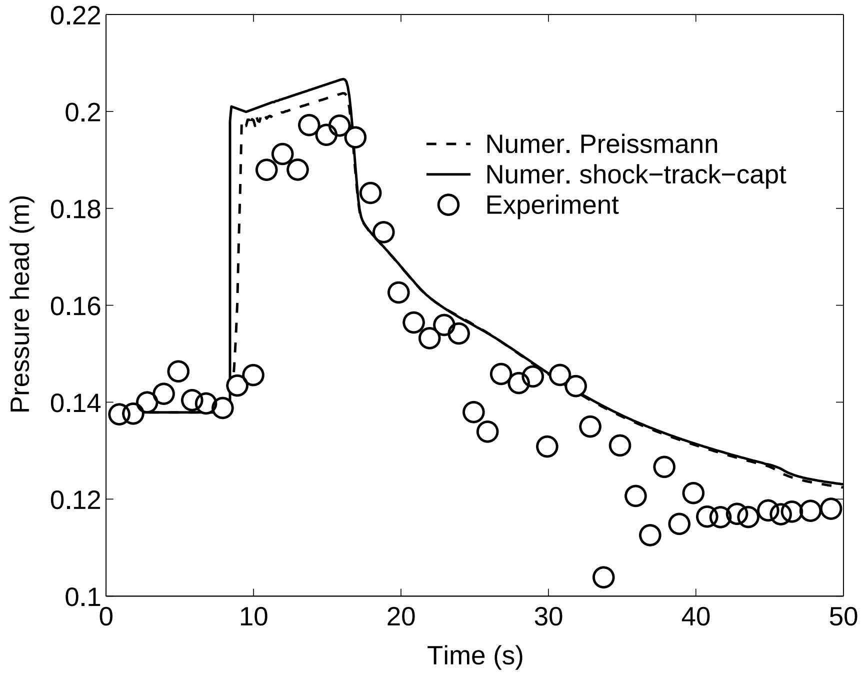

Figure 4.11: Measured and computed pressure heads at transducer P1 for trial J experiment of Cardle (1984).

As can be observed in Fig. 4.11, the simulated results have a good agreement with the experimental measurements. In particular, the arrival of the positive and negative interfaces to the location of transducer P1 is accurately simulated. However, as in the first test case, the computed shock fronts (both models) are steeper than the measured ones. Again, this is because in the experiments the closing and reopening of the gate was very rapid, but not instantaneous, as was assumed in the simulations. The instantaneous gate closure assumption in the simulations also caused slightly higher pressure heads as compared to the experimental results. As in the previous test case, the pressure traces generated using the shock tracking-capturing model are slightly higher than the *modified Preissmann model*. In Fig. 4.11, notice also that the open channel-pressurized flow shock fronts produced using the shock tracking-capturing model are steeper than the *modified Preissmann model*. This is because in the former model, open channel-pressurized flow interfaces are tracked to avoid smearing and loss of accuracy that is inevitable when the interface falls within a grid cell and the discrete solution must be averaged over the cell. The oscillations in the measured pressure heads, after the gate was reopened ($t = 15s$), may be in part due to the presence of air bubbles near the pipe crown in the experiment.

4.6.3 Hypothetical positive shock interface

The previous test cases investigated the ability of the proposed models in simulating complex flow features including positive shock interfaces. These test cases were laboratory experiments, in which the achieved pressure heads were very small. Since the proposed models are intended to be used in field applications and due to the lack of experimental data in these situations, this section and the next present hypothetical tests in order to investigate the capability of the proposed models in simulating strong transients at field scale.

The hypothetical test presented in this section considers a sloped tunnel connected to a downstream valve. The length of the tunnel is 10000 m and its diameter is 10 m, the tunnel slope is 1%, the Manning's roughness coefficient is 0.015, the initial steady-state flow discharge is 1000 m^3/s, and the waterhammer wavespeed is 1000 m/s. Notice that in the *modified Preissmann model* [Fig. 4.1 (b)], the gravity wave speed in the slot for $y > 1.50\ d$ is very close to 1000 m/s. The uniform flow depth for the initial conditions is 8.57 m that gives a supercritical flow with a Froude number of 1.40.

The transient flow is obtained after an instantaneous closure of the downstream valve at time $t = 0$. The gate closure created a strong positive shock interface moving upstream. The simulated pressure heads 50, 100, 150, and 200 s after the gate closure for both models and the 'Near exact" solution are

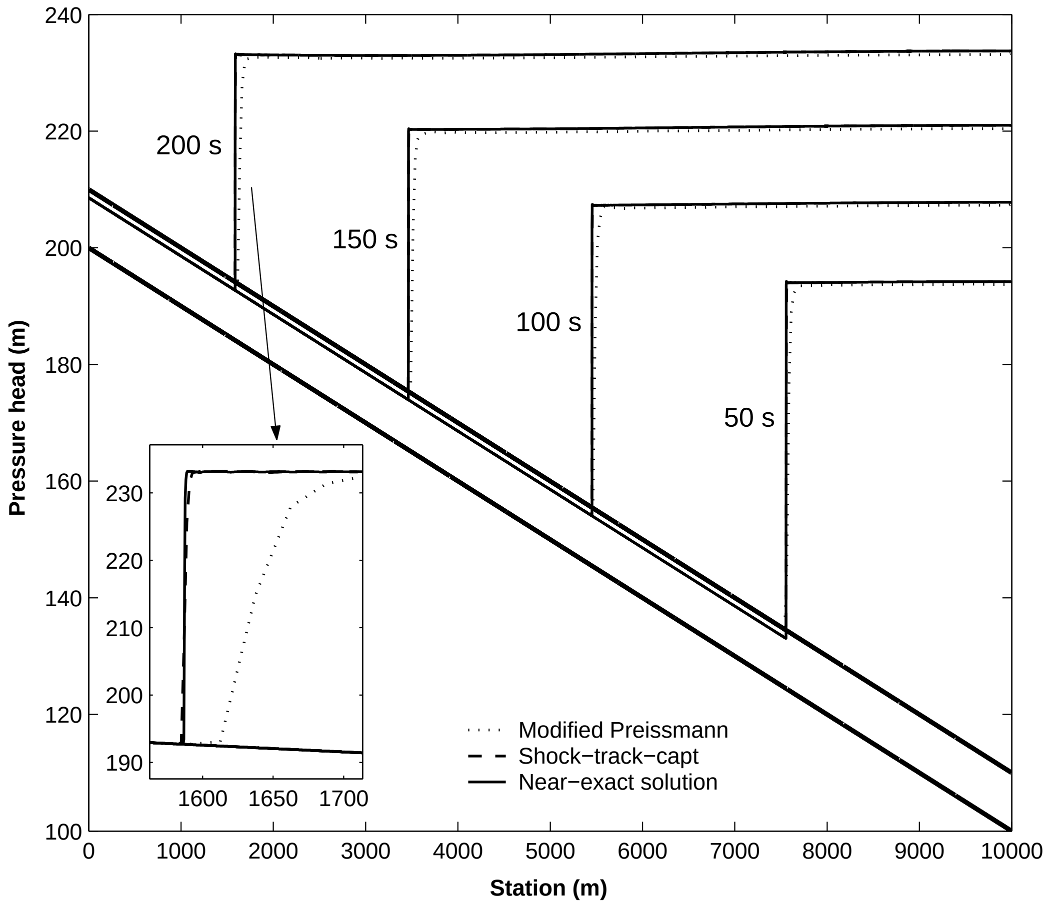

Figure 4.12: Simulated pressure heads for strong transient mixed flows.

shown in Fig. 4.12. The “Near exact” solution is obtained by grid refinement until convergence is achieved using the shock-tracking-capturing model. For both models, the simulated pressure heads were obtained using initially 400 cells and a maximum Courant number of 0.6. In the shock-tracking-capturing model, 200 s after the gate closure, the number of cells in the mesh was 402. As can be observed in Fig. 4.12, the “Near exact” shock interfaces are well resolved by both models. By contrasting both models, it can be noticed that the *modified Preissmann model* is more dissipative than the shock-tracking-capturing model.

In the *modified Preissmann model*, the slot width is chosen so that the gravity wavespeed in the slot is equal to the water hammer wavespeed (Eq. 4.3).

This results in a slot width of about 0.77 mm (0.0077% d) for the present test case. When using greater slot width sizes, such as 1% d, 2% d and 5% d, the results were not significantly influenced (results not shown). This explains why researchers using wide slots (to avoid numerical instability) obtained good agreement with experiments when simulating open channel-pressurized flow interfaces. The velocity of propagation of an open channel-pressurized flow interface is not greatly influenced by the wavespeed at each side of the interface but by the conservation of mass and momentum across the interface. Wide slots may be used with good accuracy when simulating open channel-pressurized flow interfaces. However, as is shown in the next test case, when simulating pure pressurized flows (flow in slot), only a slot width that is obtained by making the gravity wavespeed in the slot equal to the water hammer wavespeed gives accurate information on the propagation of pressurized transients. Unlike other Preissmann models that report numerical instabilities even when a slot width as large as 10% of the pipe diameter is used, when using the *modified Preissmann model* (slot width is about 0.0077% d for this test case), no instabilities were found even though strong transients at field scale are simulated.

The results in Fig. 4.12 show that for the same discretization the shock-tracking-capturing model is more accurate than the *modified Preissmann model*. A more conclusive comparison requires measurement of the CPU time needed by each scheme to achieve a given level of accuracy. The accuracy of a scheme can be measured using the following error norms (e.g., Liang et al. 2007):

$$\text{ABSERROR} = \frac{\Sigma_{i=1}^{Nx}|e_i|}{\Sigma_{i=1}^{Nx}|\phi_i^{\text{exact}}|} \tag{4.58}$$

$$\text{WAVINESS} = \frac{\Sigma_{i=1}^{Nx}|e_{i+1} - e_i|}{\Sigma_{i=1}^{Nx}|\phi_i^{\text{exact}}|} \tag{4.59}$$

where $e_i = \phi_i^{\text{numerical}} - \phi_i^{\text{exact}}$ = difference between the numerical and exact solution at node i, ϕ = dependent variable such as the pressure head or flow velocity, ABSERROR = absolute error, WAVINESS = waviness error, and Nx = number of grids. The absolute error is a measure of the difference between the numerical and exact solution for either the pressure head or flow velocity. The waviness error is a measure of the difference between the gradient of the exact and numerical solution and quantifies the magnitude of the spurious oscillation by a numerical scheme (Leonard 1991).

Figs. 4.13 and 4.14 depict the absolute and waviness error as a function of CPU time for both models. With reference to the absolute error, the shock-tracking-capturing model is between 20% to 100% more efficient than the *modified Preissmann model*. As of the waviness error, the *modified Preissmann model* presents much more spurious oscillation than the shock-tracking-capturing model.

4.6.4 Pressurized flow transients

The purpose of this section is to test the ability of the proposed models in simulating pressurized flow transients. The test considers a horizontal frictionless tunnel connected to an upstream reservoir and a downstream valve. The length of the tunnel is 10000 m and its diameter is 10 m, the upstream reservoir constant head h_0 is 200 m, the initial steady-state flow velocity is 2.0 m/s, and the water hammer wavespeed is 1000 m/s.

The transient flow is obtained after an instantaneous closure of the down-

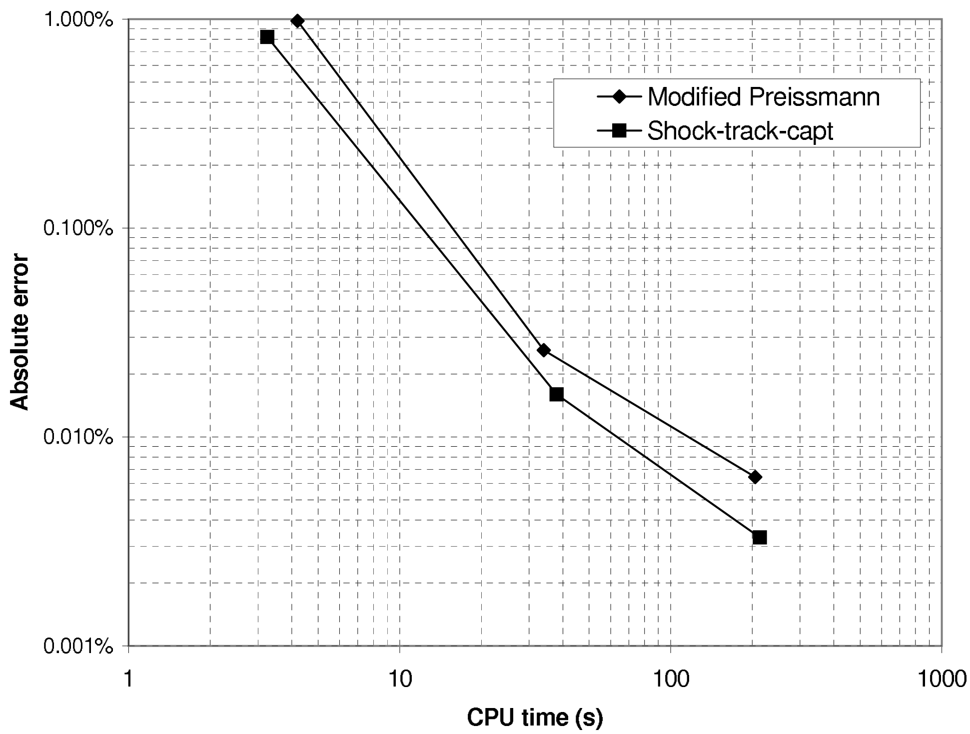

Figure 4.13: Absolute error for the pressure head versus CPU time ($t = 200$ s, $Cr = 0.6$).

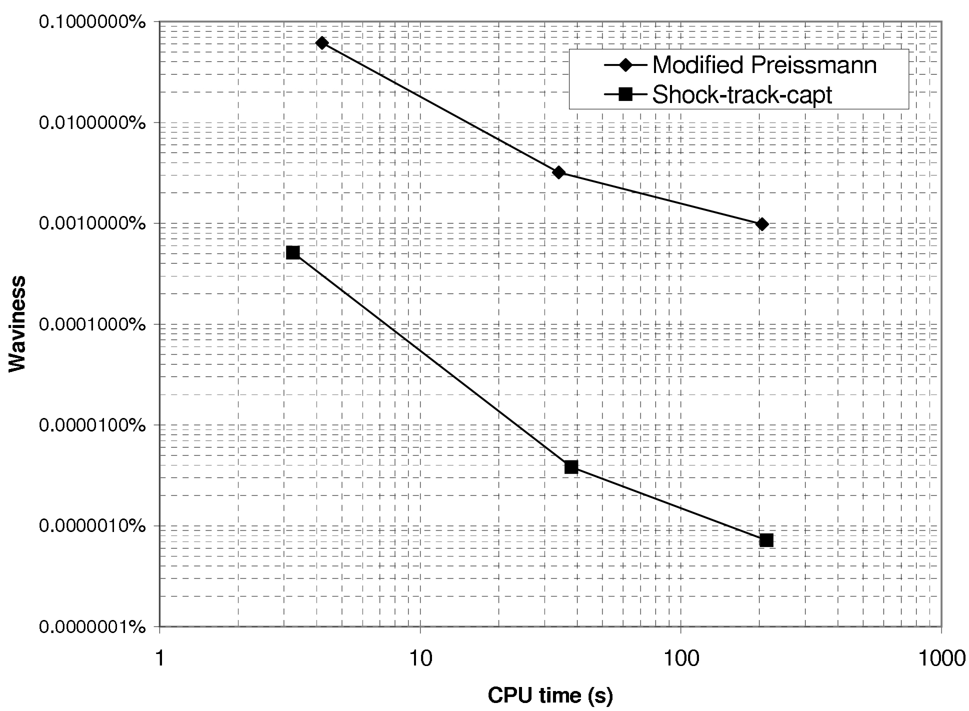

Figure 4.14: Waviness error for the pressure head versus CPU time ($t = 200$ s, $Cr = 0.6$).

stream valve. The simulated pressure heads 3, 6 and 9 s after the gate closure for both models and the ‘Near exact” solution are shown in Fig. 4.15. The “Near exact” solution is obtained by grid refinement until convergence is achieved using the shock-tracking-capturing model. For both models, the simulated pressure heads were obtained using 500 cells and a maximum Courant number of 0.8. In pure free surface or pure pressurized flows, the shock-tracking-capturing model becomes a shock-capturing model because no open channel-pressurized flow interface is present. It is recalled that in the shock tracking-capturing model, only open channel-pressurized flow interfaces are tracked.

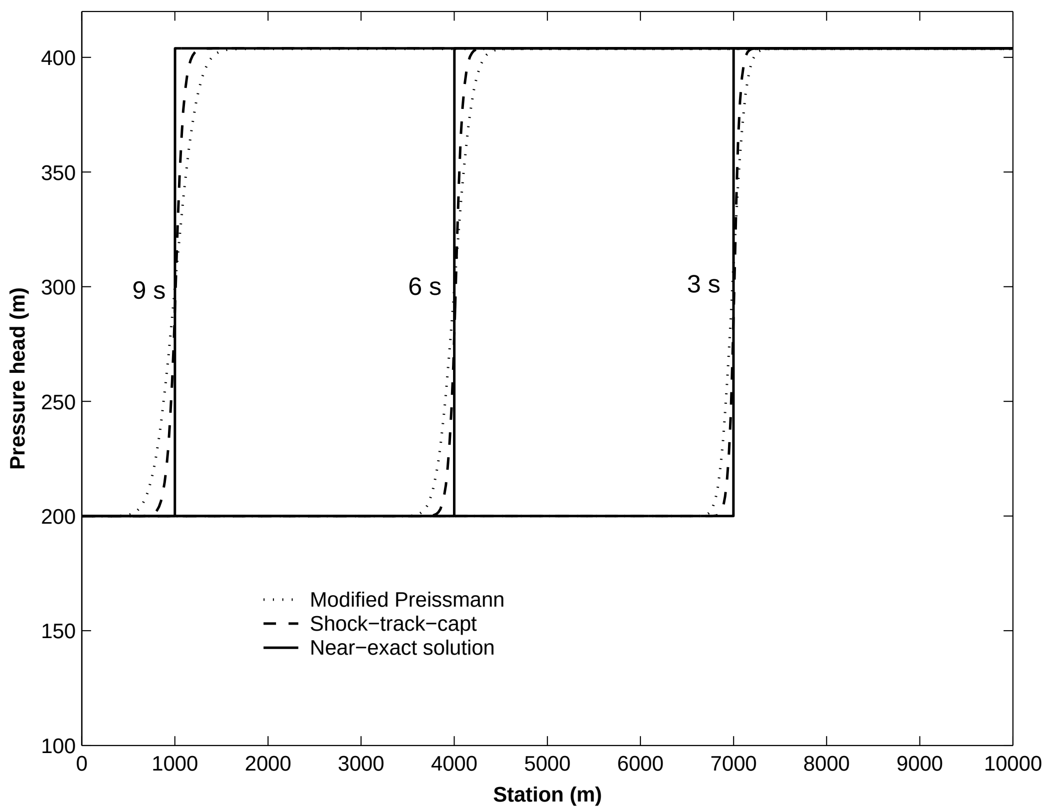

Figure 4.15: Simulated pressure heads for pressurized flow transients. For the *modified Preissmann model*, a slot width of 0.77 mm is used.

As can be observed in Fig. 4.15, the “Near exact” pressure heads are well resolved by both models. By contrasting both models, it can be noticed that the modified Preissmann model is more dissipative than the shock-tracking-capturing model. Additional simulations using the *modified Preissmann model* were carried out to investigate the influence of using wide slots for simulating the propagation of pressurized transients. The results for a slot width of only 1% d are presented in Fig. 4.16. As can be observed in this figure, the simulated results for the modified Preissmann model using a slot width of 1% d are not even close to the “Near exact” solutions. This is because the gravity wavespeed in the slot (87.8 m/s) is much smaller than the water hammer wavespeed used in the shock-tracking-capturing model (1000 m/s). It must be recalled that in pure pressurized flows, the water hammer wavespeed determines how fast the pressure transients are propagated. Evidently, the only way of reproducing the correct propagation and interaction of pressurized transients is by using a slot width that achieves a gravity wavespeed in the slot equal to the water hammer wavespeed.

As was mentioned earlier, notwithstanding the problems associated with the size of the slot in the Preissmann model, the generic equivalence between the water hammer and the free surface flow equations does not imply that both flows are identical. The use of water level in the Preissmann model to represent the water hammer head prohibits the formation of sub-atmospheric pressures and the emergence of vapor cavities, which would occur in a water hammer flow when the pressure drops below vapor pressure. Whenever the head drops below the slot, the pressure produced by the Preissmann model is equivalent to the water depth in the pipe and the magnitude of the wavespeed drops from the water hammer wavespeed to the open-channel wavespeed. In reality, however, sub-atmospheric water hammer pressures could form during depressurization and the speed of these pressures is the same as the water

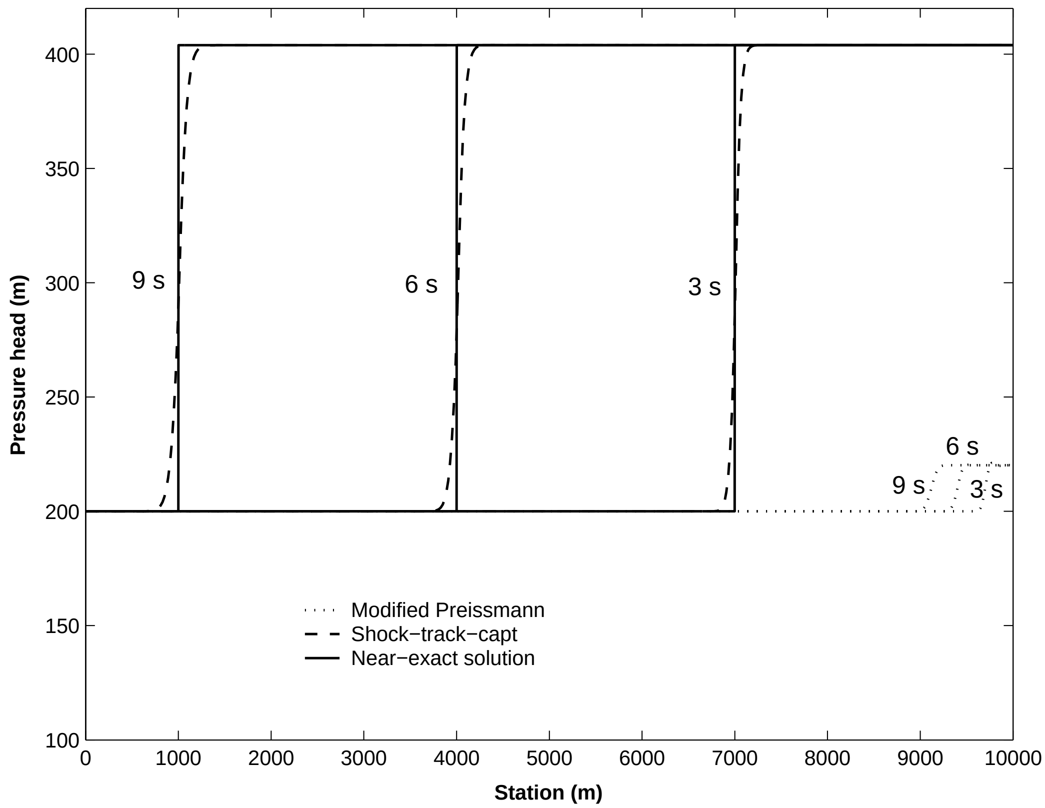

Figure 4.16: Simulated pressure heads for pressurized flow transients. For the *modified Preissmann model*, a slot width of 1% d is used.

hammer wavespeed. Therefore, Preissmann slot models cannot simulate sub-atmospheric pressures, and the results of these models after, as well as during, depressurization must be treated with caution.

Chapter 5

Applications to the Chicago TARP system

5.1 Introduction

The objective of this chapter is only intended to illustrate the capability of the modified Preissmann model in simulating the formation and propagation of hydraulic transients in complex hydraulic systems. The Tunnel and Reservoir Plan (TARP) Calumet system located in Chicago is used as the test case. The reason why only the modified Preissmann model was implemented for complex networks is because the implementation of this model is much simpler than that based on a shock capturing-tracking approach. For the latter approach, major work not only numerically but also analytically is needed especially for the treatment of boundary conditions.

In this thesis, no major details about the computer model developed (modified Preissmann model) named "Illinois Transient" are provided. A user's manual of this computer program is in preparation. This chapter is organized as follows: (1) a brief description of the TARP system is provided; (2) the parameters for the simulations are presented; and (3) the simulation results are presented and discussed.

5.2 Description of the TARP Calumet system

The TARP Project, more commonly known as the Deep Tunnel Project or the Chicago Deep Tunnel, is one of the largest civil engineering projects ever undertaken in terms of scope, money and timeframe. The schematic of the TARP Project is shown in Fig. 5.1. The goal of this project is to reduce flooding in the metropolitan Chicagoland area, and to reduce the harmful effects of flushing raw sewage into Lake Michigan by diverting storm and sewage water into temporary holding reservoirs. The project is managed by the Metropolitan Water Reclamation District of Greater Chicago.

The project was commissioned in the mid 1970s. Full completion of the system is not anticipated until 2019, but substantial portions of the system have already opened and are currently operational. Across 30 years of construction, over 3 billion dollars has been spent on the project (Sanders 2005). TARP consists of 109 miles (175 km) of deep tunnel, bored in rock and lined with concrete. The tunnels range from 9 to 33 ft (2.7 to 10 m) in diameter and are located 200 to 350 ft (61 to 106 m) below ground. The 109 miles of tunnels were recently (2006) completed and are in service. The system also includes reservoirs, drop shafts, connecting structures, pumping stations, and other appurtenances for the capture and storage of Combined Sewer Overflows (CSOs) and for conveying the stored CSOs to water reclamation plants for treatment. Fig. 5.2 shows the schematic for the capture, storage and treatment of CSOs. All 450 CSOs in the 375 square mile (971 km^2) service area are diverted to the deep tunnel system (Ven Te Chow Hydrosystems Lab. 2006). Reservoirs are

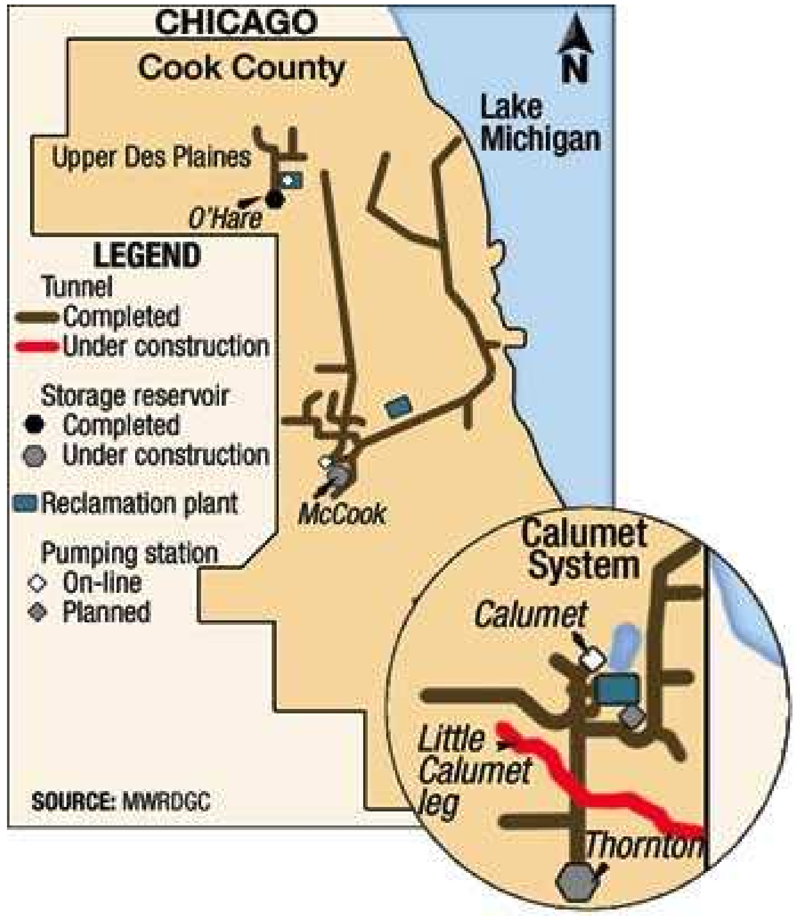

Figure 5.1: TARP schematic.

located at the downstream ends of the tunnels to provide additional storage capacity for CSOs, and consist of the Thornton Reservoir (24,200 Acre-Feet [29 850 000 m^3]), the McCook Reservoir (32,000 Acre-Feet [39 471 000 m^3]), and the O'Hare Reservoir (1,050 Acre-Feet [1 295 000 m^3]).

The TARP Project has 3 major tunnel systems namely, Calumet, Des Plaines, and Mainstream. In this thesis, the Calumet system is used as the test case. The major additional structures for the Calumet system include the future Thornton reservoir and the Calumet wastewater reclamation plant. Following, photos of some structures for the Calumet system that are finished or under construction are shown.

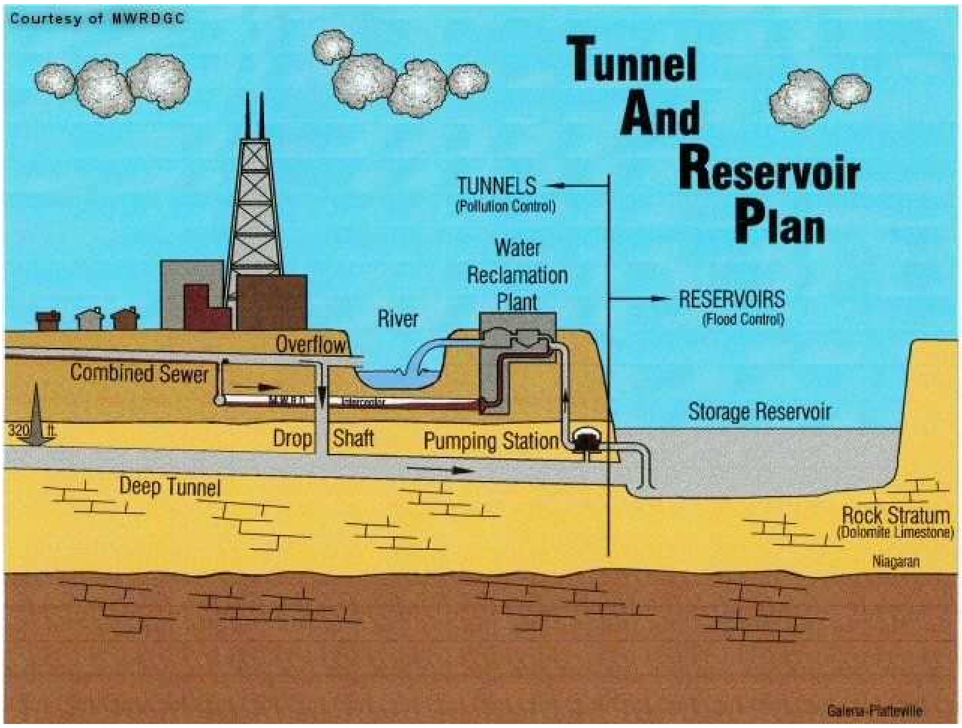

Figure 5.2: Combined sewer overflow/Interceptor Schematic.

Figure 5.3: Thornton reservoir under construction.

Figure 5.4: The Calumet Wastewater Reclamation Plant, located adjacent to Lake Calumet, Chicago, Illinois.

Figure 5.5: Tunnel boring machine penetrating through terminal construction shaft.

Figure 5.6: 27 ft. tunnel boring machine used on one of the contracts for the TARP Project.

5.3 Parameters for the simulations

The layout of the actual Calumet system is shown in Fig. 5.7. The simplified layout of this system adopted in the simulations is shown in Fig. 5.8. The simplified system (Fig. 5.8) consists of 39 tunnel segments, 5 three-way junctions, 28 two-way junctions and 19 dropshafts/junctions with inflow hydrographs. All the junctions and dropshafts are assumed to have a cylindrical shape with a diameter of 10 m and infinite height to avoid overflows. The physical characteristics of the tunnel segments are listed in Table 5.1.

In Table 5.1, the first column indicates the identification number (Id) of each tunnel segment (pipe). The second and third columns designate the Id's of upstream tunnel segments to which a downstream tunnel segment is connected. For instance, the first row of Table 5.1 specifies that the upstream end of pipe 1 is connected to pipes 2 and 16. The fourth and fifth columns spec-

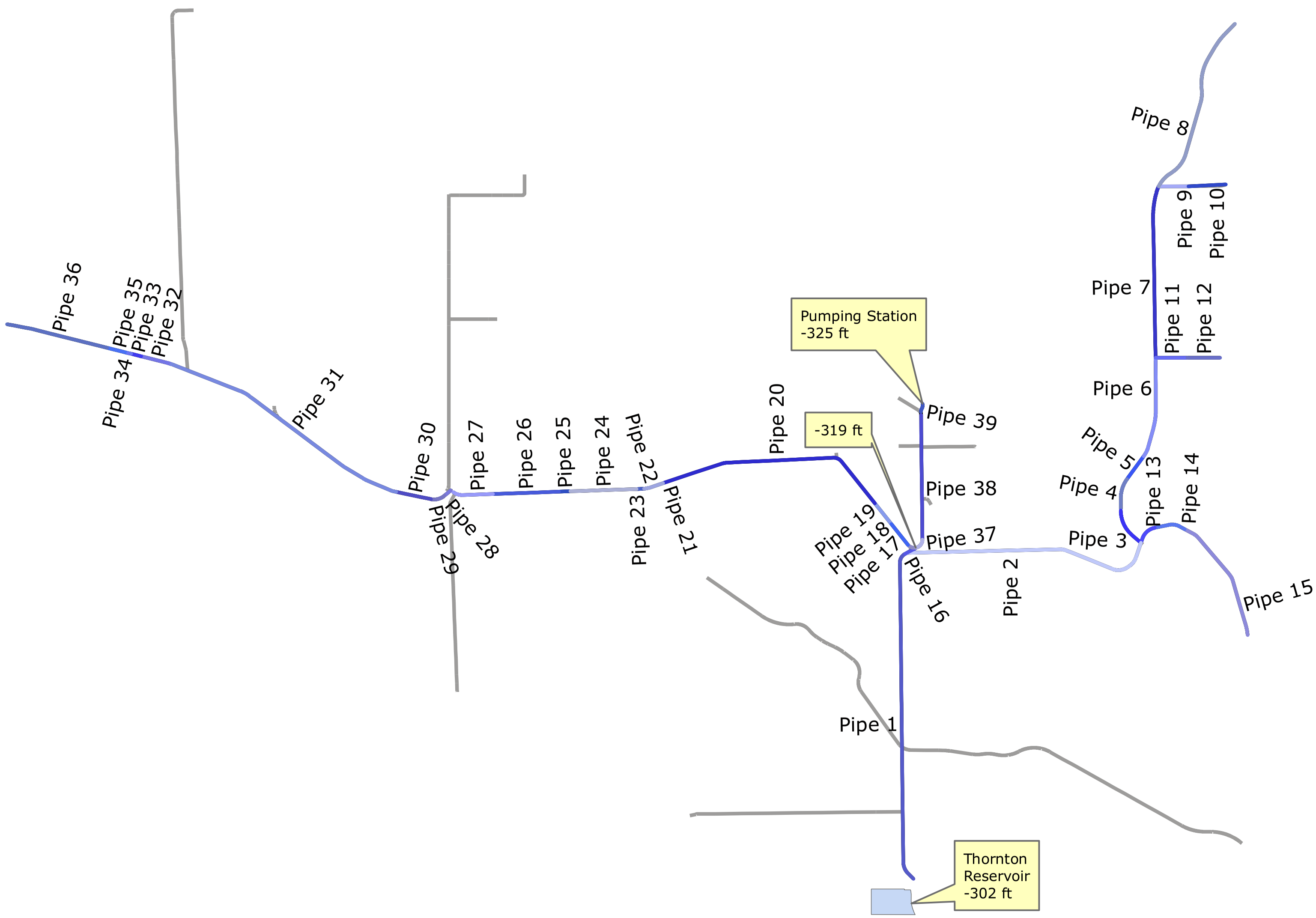

Figure 5.7: Actual layout of the Calumet system.

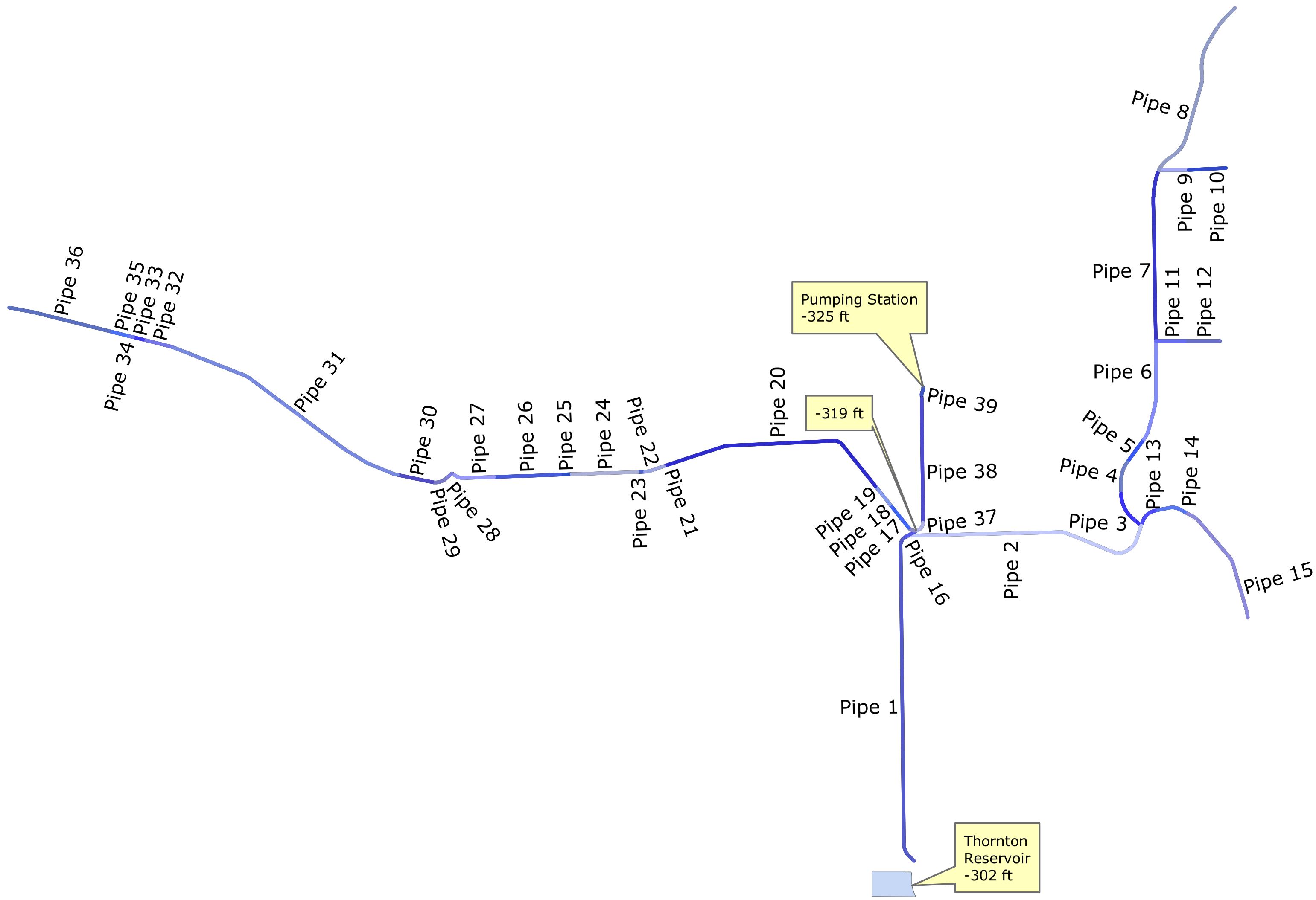

Figure 5.8: Simplified layout of the Calumet system used in the simulations.

Table 5.1: Physical characteristics for the simplified Calumet combined sewer system.

Pipe ID	Upst. pipe ID 1	Upst. pipe ID 2	Inv. elev. upst. (m)	Inv. elev. downst. (m)	Length (m)	Diam. (m)	n	bound. ID (upst.)	Hydrog. ID (upst.)
1	2	16	-97.262	-92.037	6210	9.19	0.015	7	3
2	3	13	-93.064	-97.262	4809	9.19	0.015	7	2
3	4	0	-91.303	-91.489	258	7.62	0.015	8	0
4	5	0	-90.163	-91.303	1111	7.62	0.015	8	0
5	6	0	-89.489	-90.163	536	7.62	0.015	8	0
6	7	11	-87.603	-89.489	1888	7.62	0.015	7	7
7	8	9	-84.367	-87.603	3233	7.62	0.015	7	9
8	0	0	-80.879	-84.367	3493	7.62	0.015	4	10
9	10	0	-80.220	-81.319	1106	4.57	0.015	8	0
10	0	0	-80.089	-80.220	156	4.57	0.015	4	11
11	12	0	-83.390	-84.555	1166	4.57	0.015	8	0
12	0	0	-83.372	-83.390	47	4.57	0.015	4	8
13	14	0	-92.711	-93.064	404	9.19	0.015	8	4
14	15	0	-88.000	-88.139	584	4.62	0.015	8	5
15	0	0	-87.500	-88.000	2119	4.62	0.015	4	6
16	17	37	-94.500	-94.544	240	6.48	0.015	7	0
17	18	0	-94.400	-94.500	173	6.48	0.015	8	0
18	19	0	-94.300	-94.400	499	6.48	0.015	8	0
19	20	0	-94.200	-94.300	499	6.48	0.015	8	12
20	21	0	-80.958	-94.200	4408	6.48	0.015	8	13
21	22	0	-80.921	-80.958	33	6.48	0.015	8	14
22	23	0	-79.736	-80.921	375	6.48	0.015	8	0
23	24	0	-79.382	-79.736	139	6.48	0.015	8	15
24	25	0	-75.578	-79.382	1247	6.48	0.015	8	16
25	26	0	-74.899	-75.578	215	6.48	0.015	8	17
26	27	0	-71.223	-74.899	1241	6.48	0.015	8	18

Table 5.1 (Cont.): Physical characteristics for the simplified Calumet combined sewer system.

Pipe ID	**Upst. pipe ID 1**	**Upst. pipe ID 2**	**Inv. elev. upst. (m)**	**Inv. elev. downst. (m)**	**Length (m)**	**Diam. (m)**	n	**bound. ID (upst.)**	**Hydrog. ID (upst.)**
27	28	0	-68.765	-71.223	782	6.48	0.015	8	0
28	29	0	-64.000	-64.878	154	2.59	0.015	8	0
29	30	0	-63.246	-64.000	268	2.59	0.015	8	0
30	31	0	-58.089	-63.246	669	2.59	0.015	8	0
31	32	0	-44.846	-58.089	4899	2.59	0.015	8	0
32	33	0	-42.962	-44.846	585	2.59	0.015	8	0
33	34	0	-42.748	-42.962	192	2.59	0.015	8	0
34	35	0	-42.598	-42.748	61	2.59	0.015	8	0
35	36	0	-41.192	-42.598	402	2.59	0.015	8	0
36	0	0	-36.271	-41.192	1935	2.59	0.015	4	19
37	38	0	-94.792	-94.500	672	6.48	0.015	8	0
38	39	0	-96.083	-94.792	7684	6.48	0.015	8	1
39	0	0	-96.194	-96.083	707	6.48	0.015	10	0

Table 5.2: Identification number for boundary conditions used in the simulations.

Boundary description	**Identification number**
Dropshaft with inflow hydrograph	4
Three-way junction	7
Two-way junction	8
Downstream reservoir	9
Constant flow discharge	10

ify the upstream and downstream invert elevations for every tunnel segment, respectively. The sixth, seventh and eighth columns list the length, diameter and Manning's roughness for each tunnel segment, respectively. The ninth column indicates the identification number of the boundary condition specified upstream of each pipe. Five different boundary conditions were considered in the simulations, the description of which is listed in Table 5.2. The mathematical formulation for these boundary conditions can be obtained from Chapter 4. The tenth column designates the Id of the inflow hydrograph imposed upstream of every tunnel segment. The inflow hydrographs were specified at 19 open boundaries between junctions and dropshafts. These inflow hydrographs, which are shown in Figs. 5.9 - 5.11, are based upon triangular hydrographs with peak flows corresponding to the 5-year storm event.

For the simulations, two scenarios are considered. These scenarios are (1) excluding the Thornton reservoir (actual state), and (2) assuming the Thornton reservoir is in operation (future state). In the first scenario, a zero-water flux boundary (tunnel with dead end) is imposed downstream of pipe segment 1. In the second scenario, the stage-storage curve for the Thornton reservoir

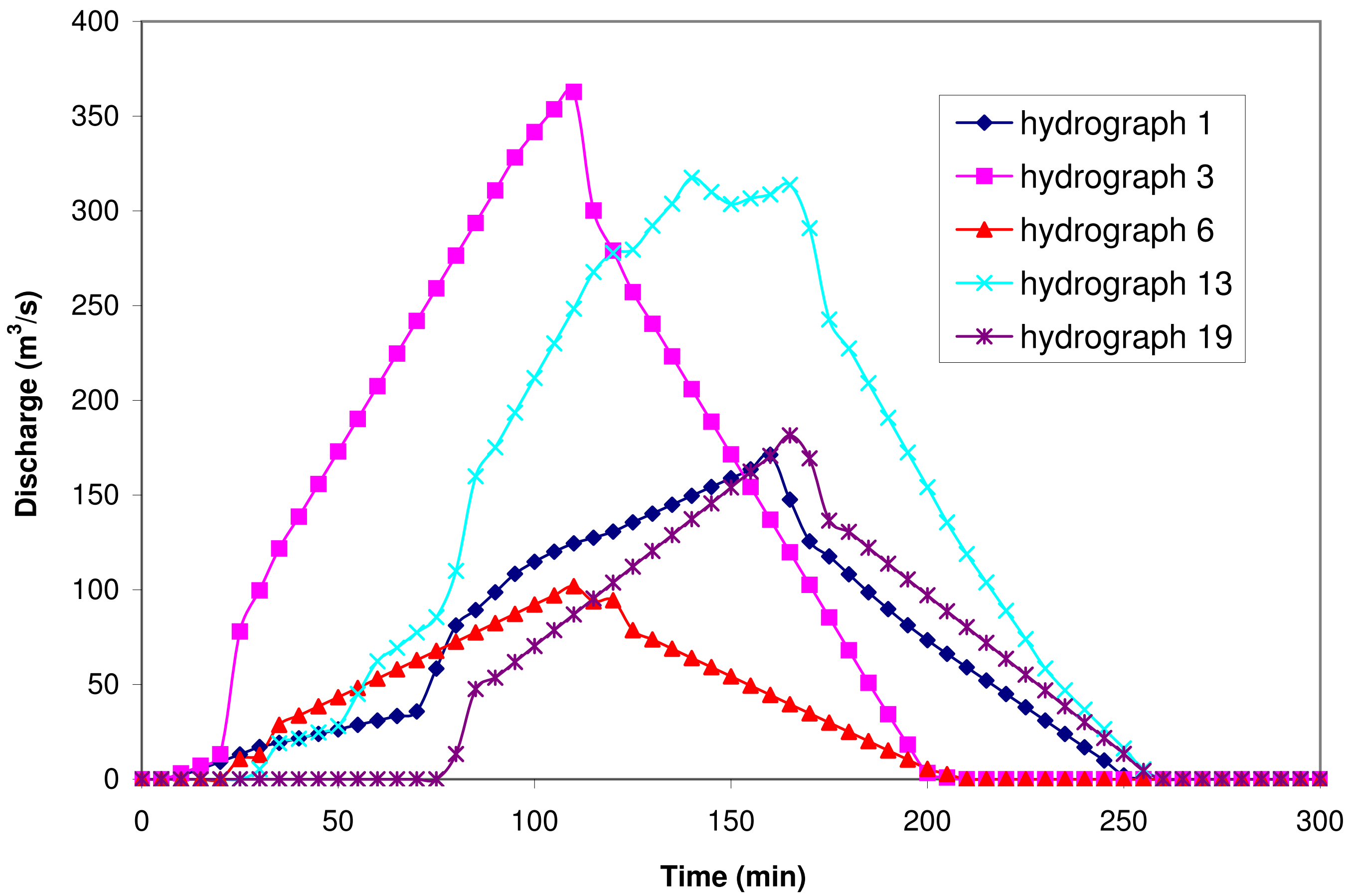

Figure 5.9: Inflow hydrographs for the simulations.

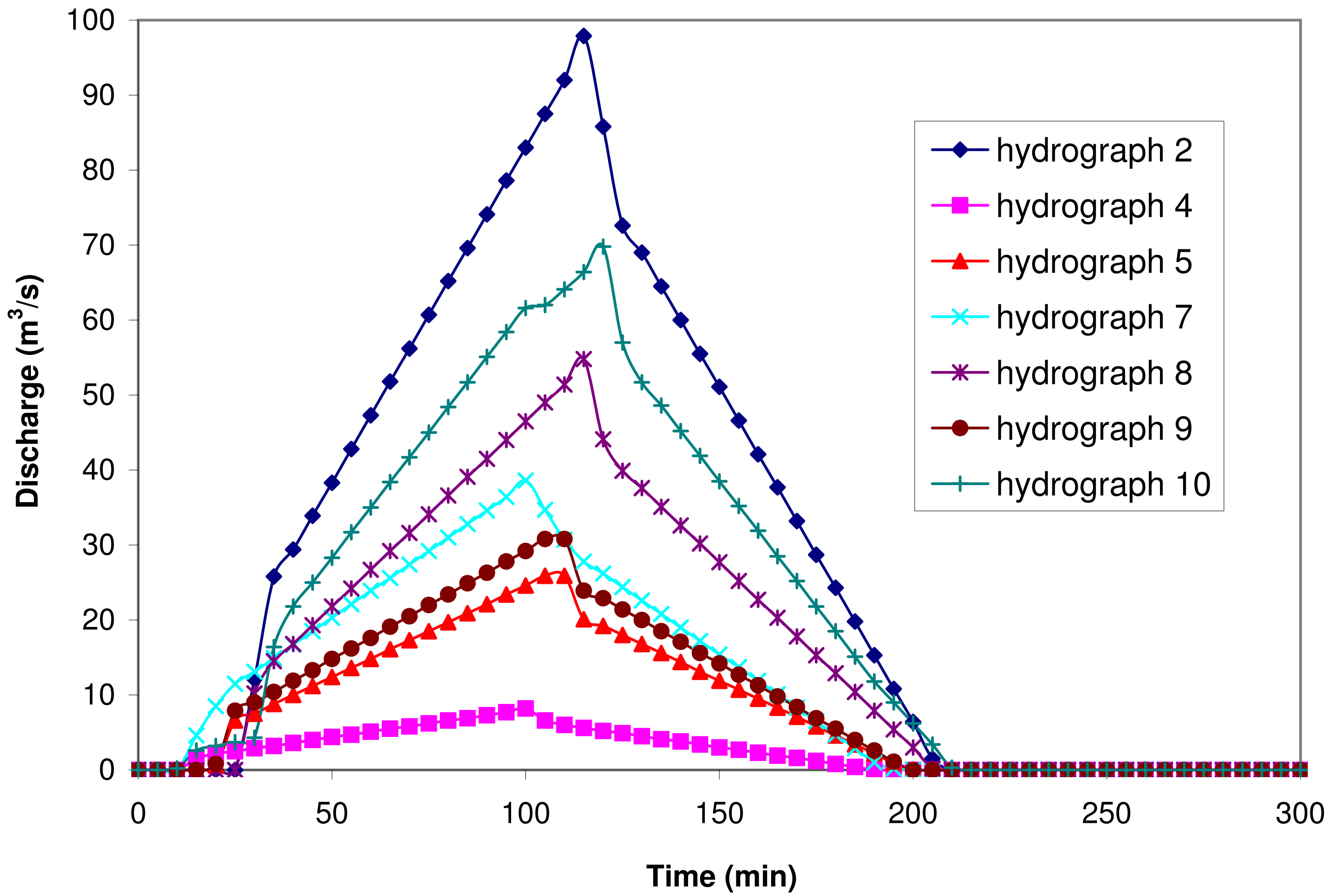

Figure 5.10: Inflow hydrographs for the simulations (Cont.)

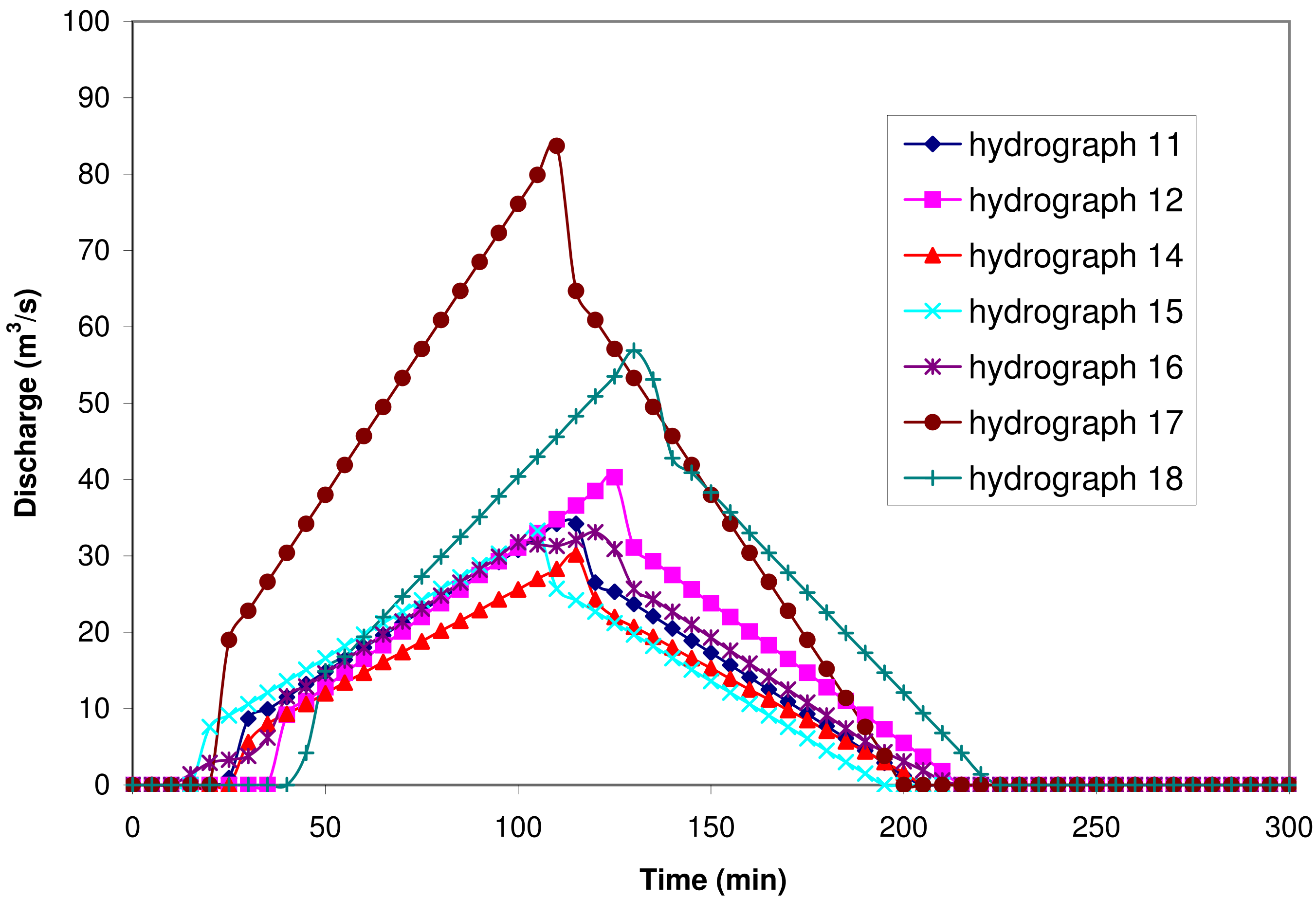

Figure 5.11: Inflow hydrographs for the simulations (Cont.)

is specified downstream of pipe segment 1. This curve is shown in Fig. 5.12. For the initial conditions, a dry-bed state is used in both scenarios. That is, zero flow depth and discharge throughout the sewer network is specified at the initial time ($t = 0$).

5.4 Simulation results and discussions

The simulations presented in this section are only intended to illustrate the capability of the modified Preissmann model in simulating the formation and propagation of hydraulic transients in complex hydraulic systems. Following the simulation results for the two considered scenarios are presented and discussed.

5.4.1 First scenario

Figs. 5.13 - 5.18 show hydraulic gradelines (measured from the invert of the pipe rather than from a horizontal datum) along two main lines (Fig. 5.19) at several instants. As shown in Fig. 5.19, the first main line extends from $x = 0\ m$ to $x = 25150\ m$ and the second from $x = 25200\ m$ to $x = 40500\ m$. For clarity in presentation of results, the first main line is subdivided into two sections. The first section extends from $x = 0\ m$ to $x = 10000\ m$ and the second from $x = 10000\ m$ to $x = 25150\ m$. Table 5.3 presents the stationing used in the model for defining the tunnel segments of the system.

Figs. 5.13 - 5.18 show the presence of open-channel bores, open channel-pressurized flow interfaces and their interactions at different times. These figures also show that the system starts to presssurize at the three-way junction of pipes 1, 2 and 16 at about $t = 1$ hour. Right after this junction gets

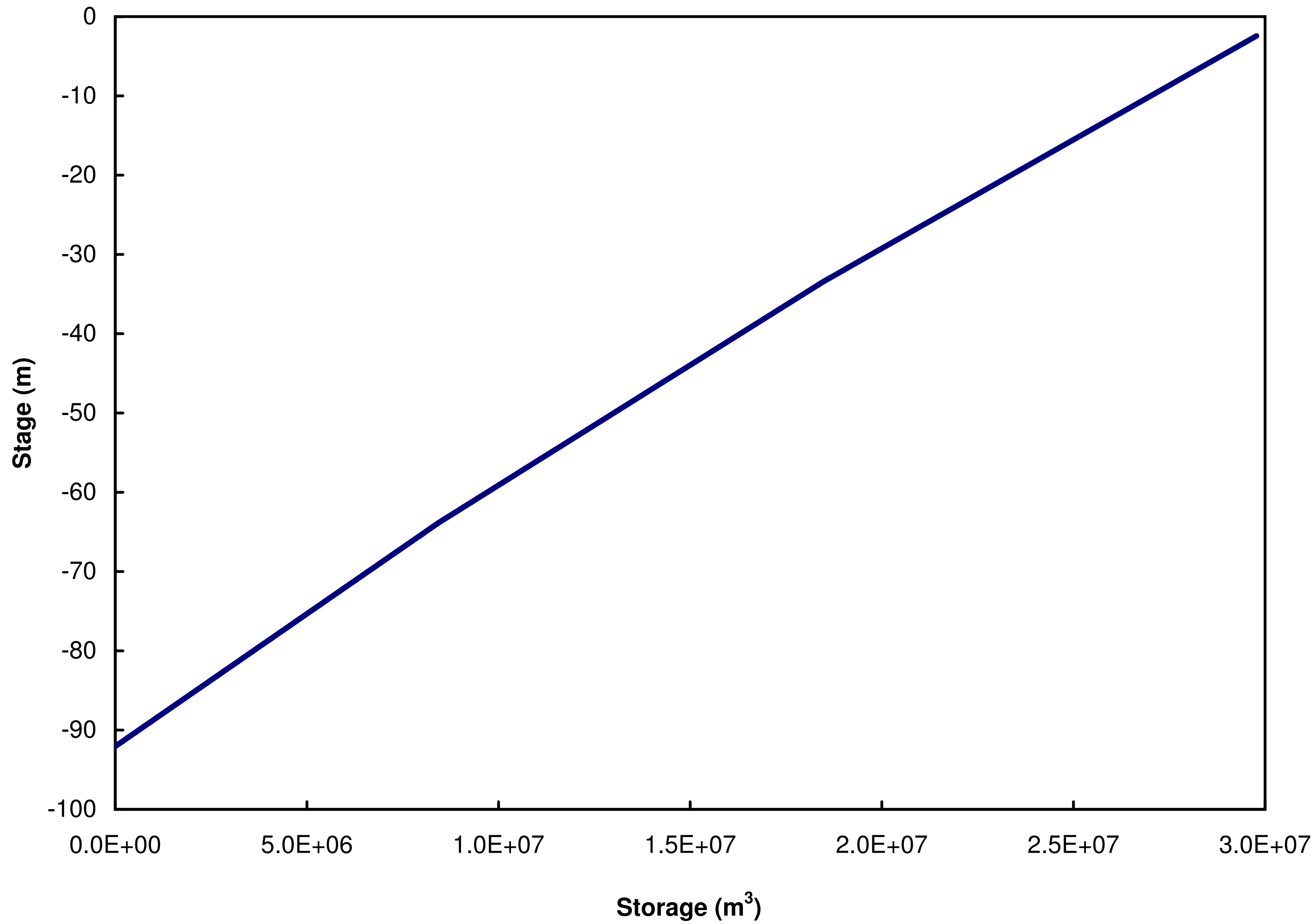

Figure 5.12: Stage-storage curve for the Thornton reservoir.

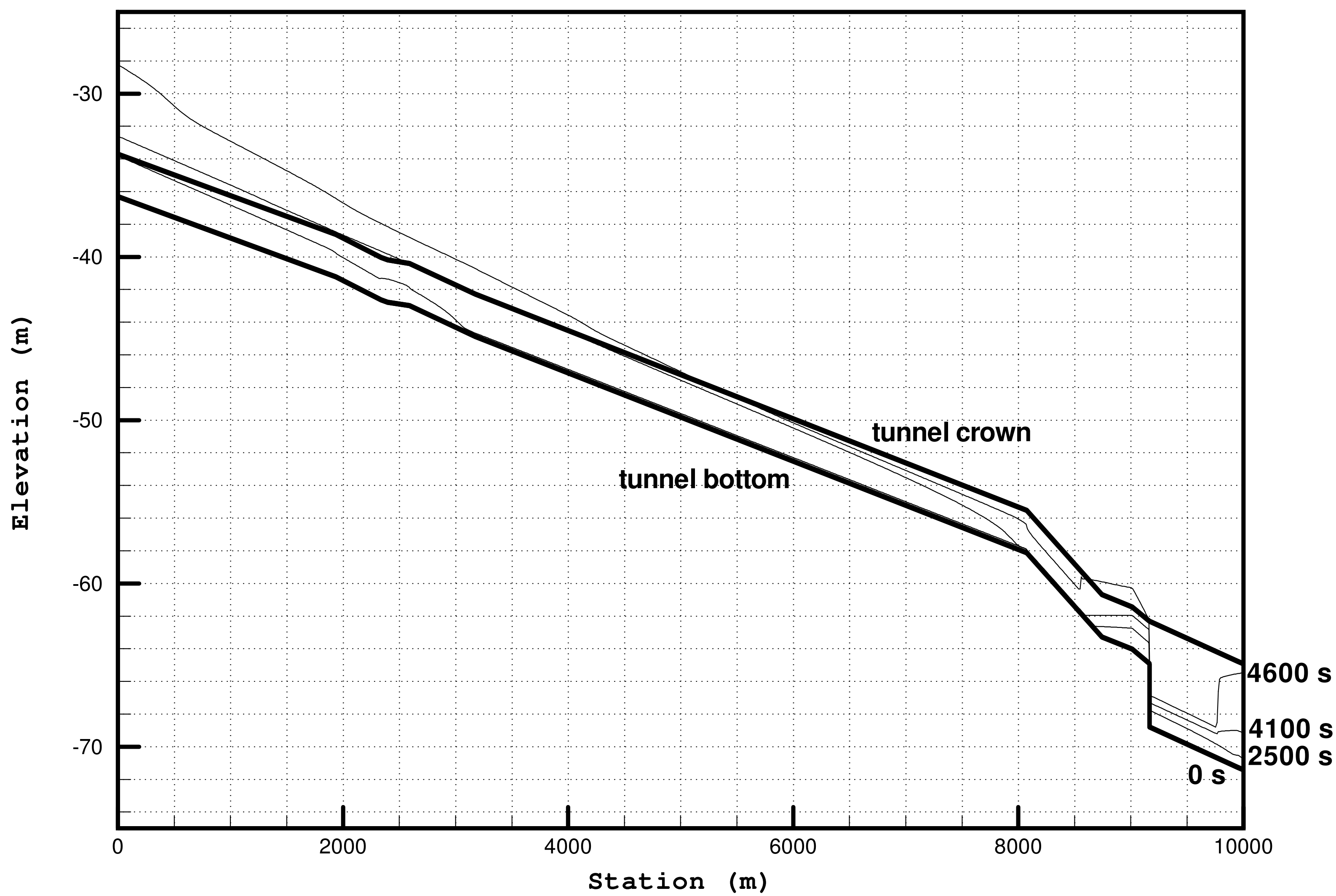

Figure 5.13: Computed hydraulic gradelines between stations $x = 0$ m and $x = 10000$ m from 0 s to 4600 s (No reservoir).

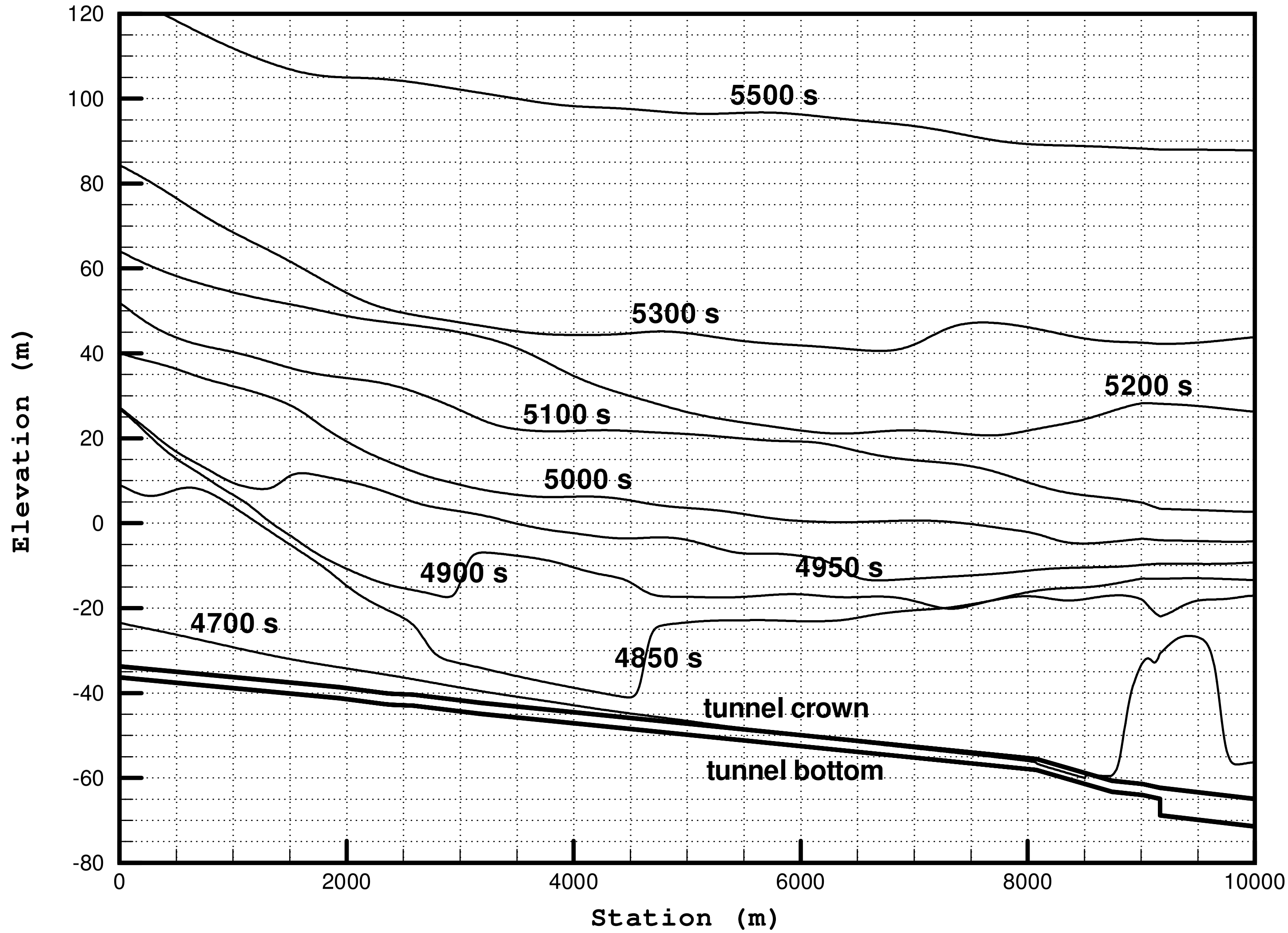

Figure 5.14: Computed hydraulic gradelines between stations $x = 0$ m and $x = 10000$ m from 4700 s to 5500 s (No reservoir).

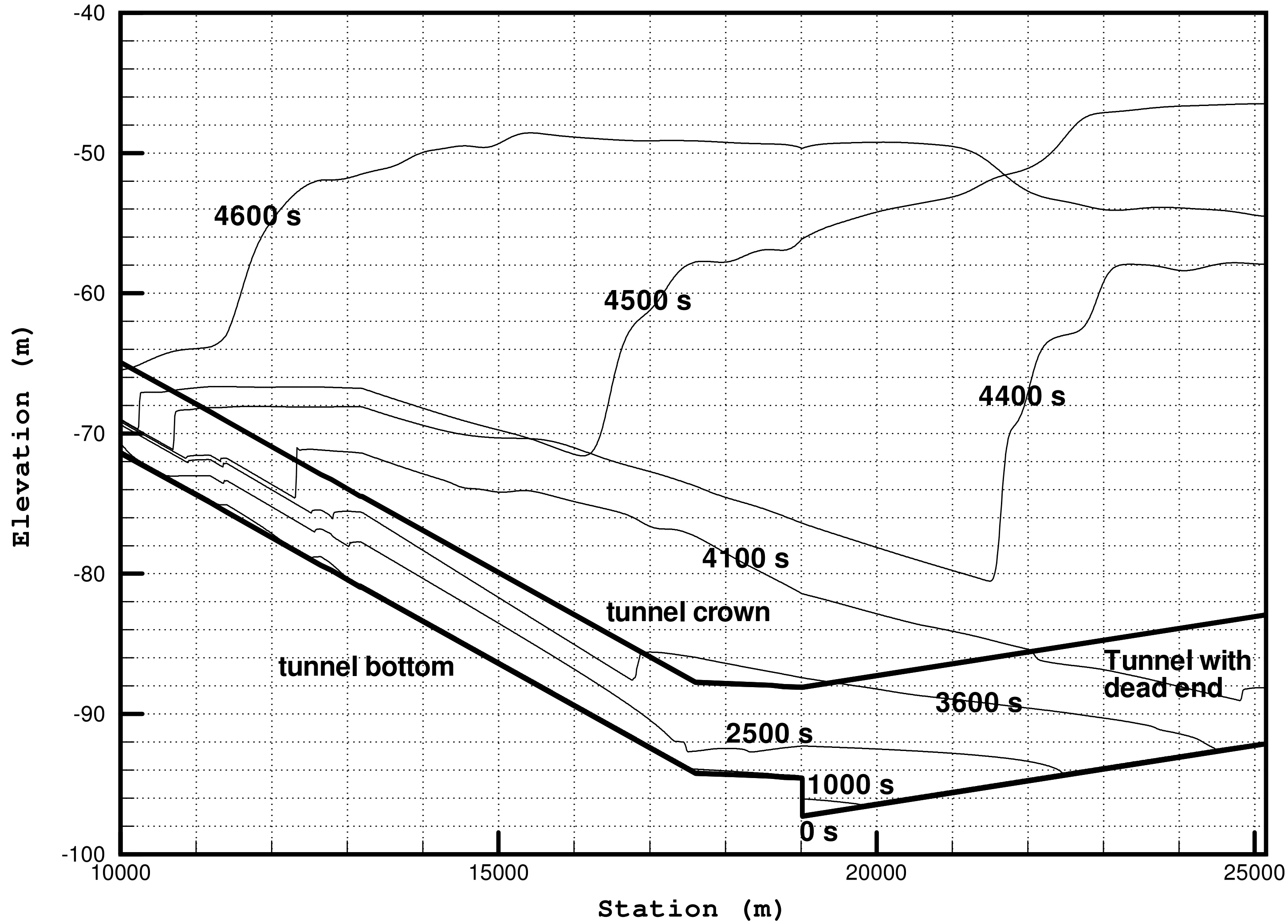

Figure 5.15: Computed hydraulic gradelines between stations $x = 10000$ m and $x = 25150$ m from 0 s to 4600 s (No reservoir).

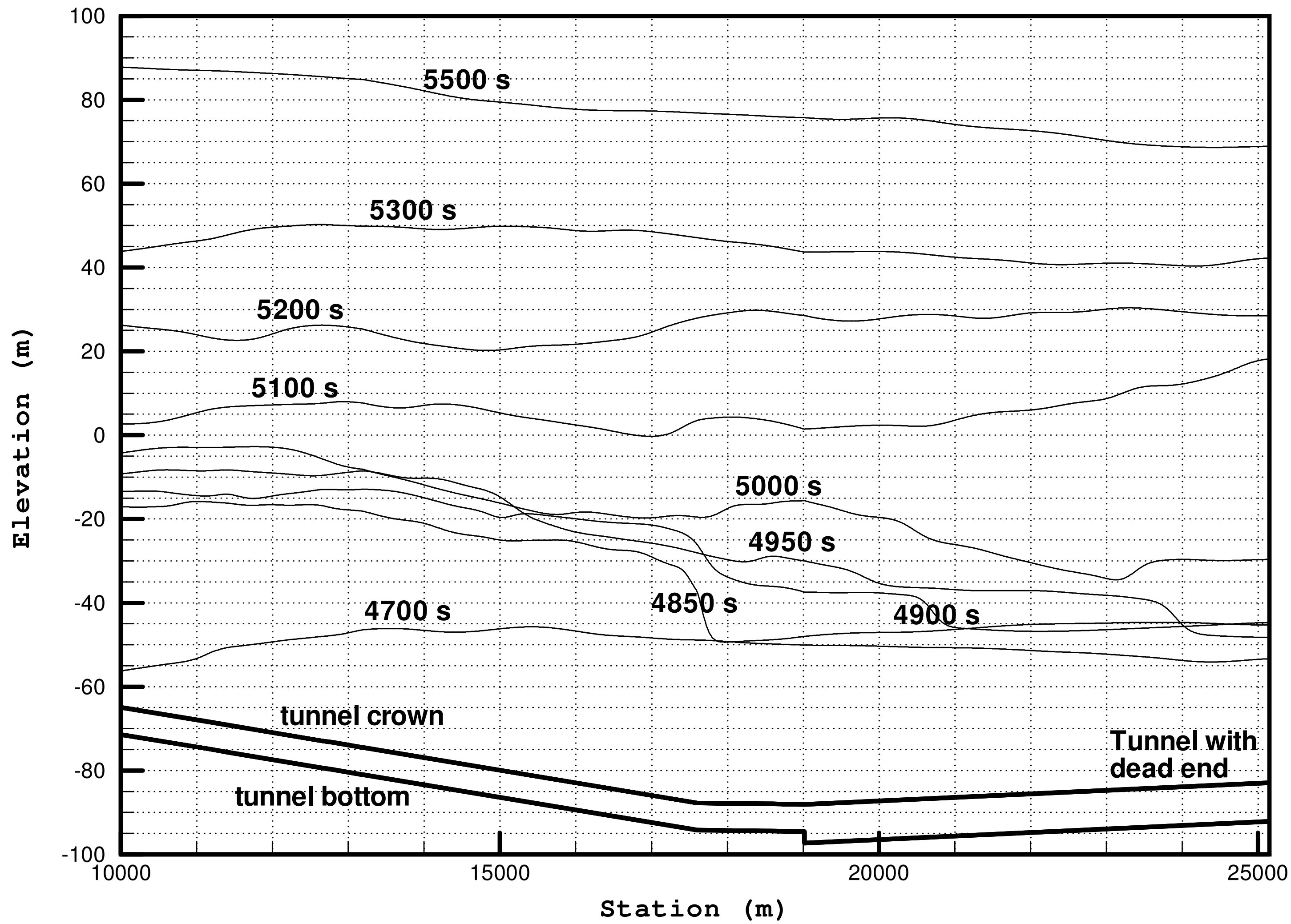

Figure 5.16: Computed hydraulic gradelines between stations $x = 10000$ m and $x = 25150$ m from 4700 s to 5500 s (No reservoir).

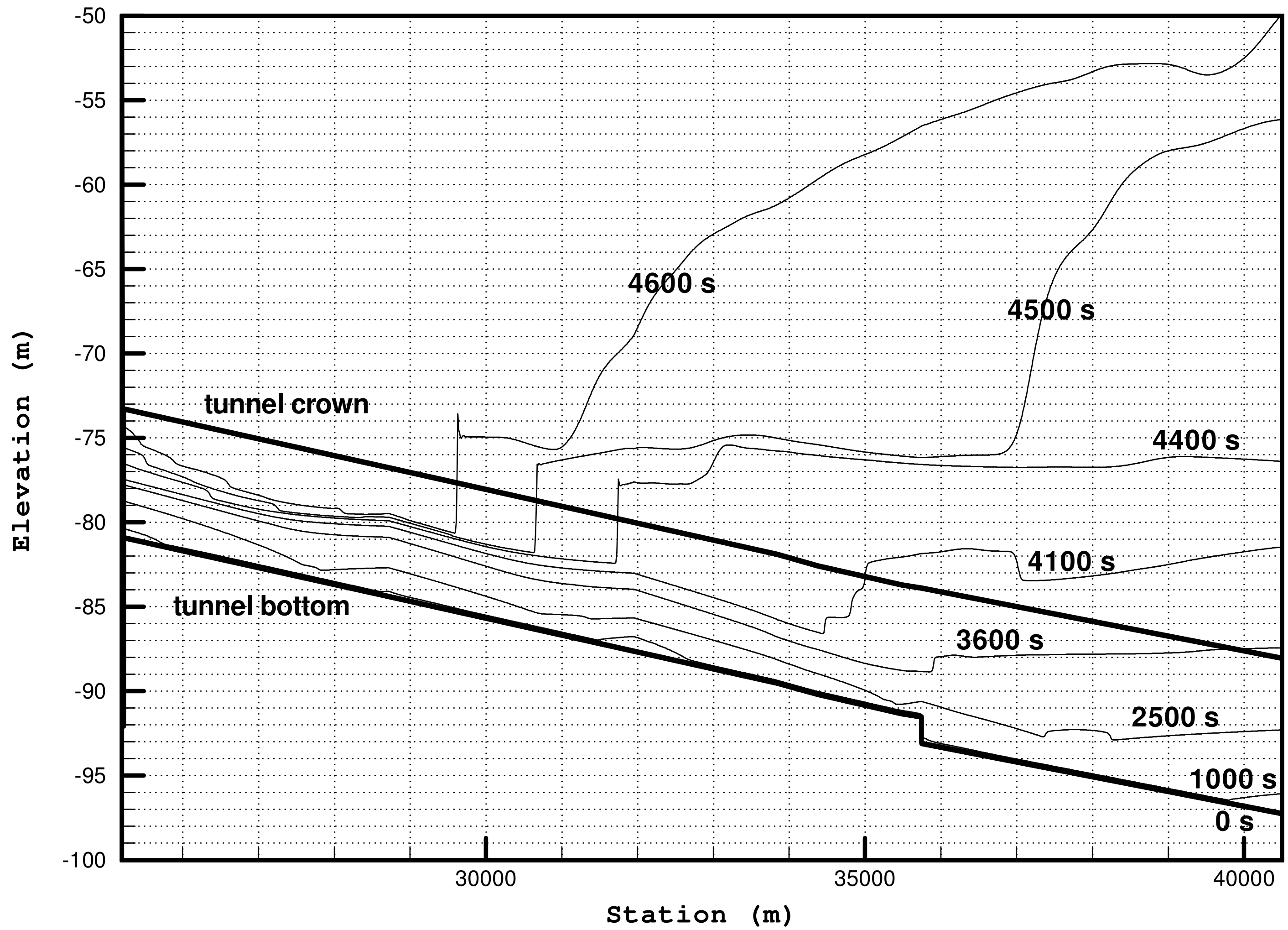

Figure 5.17: Computed hydraulic gradelines between stations $x = 25200$ m and $x = 40500$ m from 0 s to 4600 s (No reservoir).

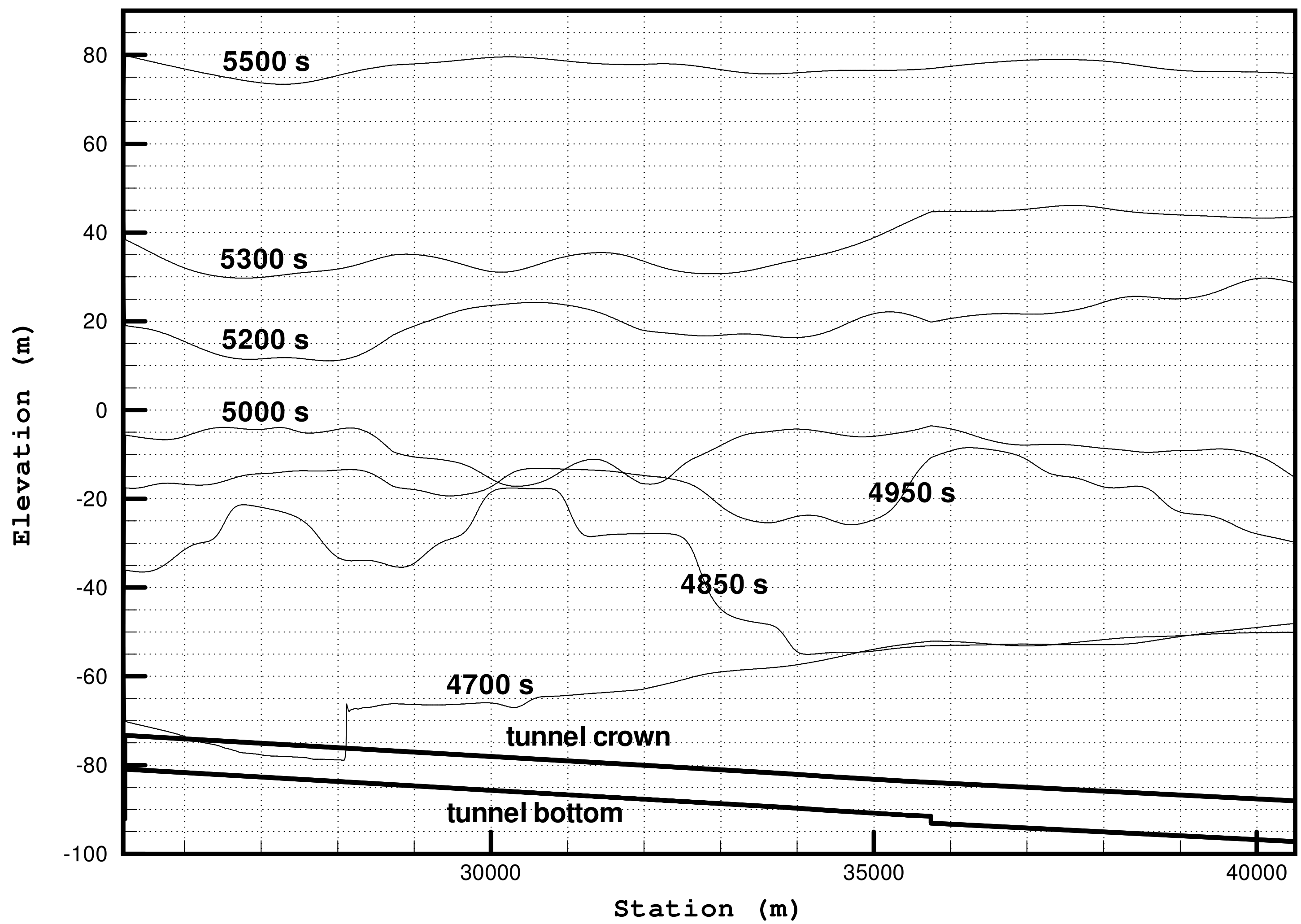

Figure 5.18: Computed hydraulic gradelines between stations $x = 25200$ m and $x = 40500$ m from 4700 s to 5500 s (No reservoir).

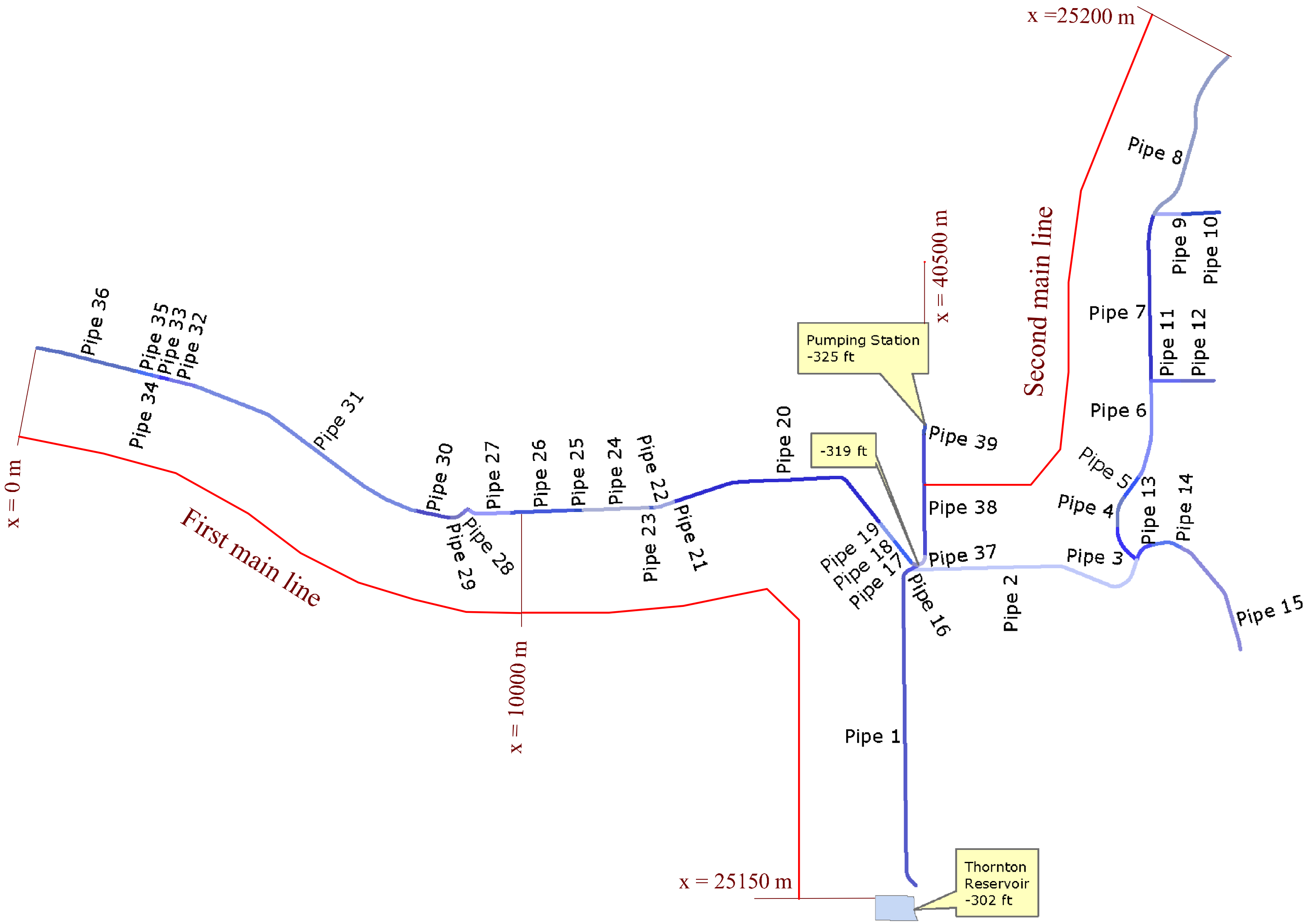

Figure 5.19: Definition of sections considered for presentation of results.

Table 5.3: Stationing used in the model for defining the tunnel segments of the Calumet system.

Upstream stationing (m)	Downstream stationing (m)	Pipe ID
0	1935	36
1935	2337	35
2337	2398	34
2398	2590	33
2590	3175	32
3175	8074	31
8074	8743	30
8743	9011	29
9011	9165	28
9165	9947	27
9947	11188	26
11188	11403	25
11403	12650	24
12650	12789	23
12789	13164	22
13164	13197	21
13197	17605	20
17605	18104	19
18104	18603	18
18603	18776	17
18776	19016	16
19016	25226	1
25226	28719	8
28719	31952	7
31952	33840	6
33840	34376	5
34376	35487	4
35487	35745	3
35745	40554	2

pressurized, two sharp pressurization waves (positive open channel-pressurized flow interfaces) start to move upstream from the junction through pipes 2 and 16. The amplitude of each of these waves increases as the wave moves further upstream inside these pipes. Immediately after the pressurization of the junction of pipes 1, 2 and 16, another wave also starts to propagate downstream from this junction towards the dead end (location of Thornton reservoir in second scenario). This wave propagates smoothly over the adverse slope in pipe 1. When this wave reaches the dead end, the wave is magnified and reflected back. The results also show that pressurization may start from upstream (5.13). Upstream pressurization may be created when the inflow rate exceeds the capacity of the tunnel at some point upstream. At later times complex interactions of waves occur. In this scenario, no outflow from the system is allowed, resulting in a continuous increase of the hydraulic gradelines as long as there is flow entering the system.

The elevation of the ground level of the Chicago city above the Deep Tunnel system is between 8 and 30 ft (2.4 and 9.1 m). In the actual Calumet system, there are several relief structures with their overflow crests at the ground level. Not allowing overflows in the simulations clearly invalidates our results for gradelines above the Chicago city ground levels. Prediction of overflows is beyond the scope of this thesis. It is recalled that the objective of this chapter is only intended to illustrate the capability of the modified Preissmann model in simulating the formation and propagation of hydraulic transients.

5.4.2 Second scenario

In a similar way to the first scenario, Figs. 5.20 - 5.25 show hydraulic gradelines at several instants for the second scenario. The results show that the gradelines for the second scenario are the same as those for the first scenario for $t < \approx 4000\ s$. After this time, the Thornton reservoir starts to receive water from the system and becomes the mechanism of control and stabilization for the hydraulic transients in the system. For instance, at $t = 5500\ s$, between stations $x = 0\ m$ and $x = 10000\ m$ the maximum elevation for the hydraulic gradeline in the first scenario was about +120 m and about +28 m in the second scenario. At the same instant ($t = 5500\ s$), between stations $x = 10000\ m$ and $x = 25150\ m$ the maximum elevation for the hydraulic gradeline in the first scenario was about +88 m and about +13 m in the second scenario. Also, at $t = 5500\ s$, between stations $x = 25200\ m$ and $x = 40500\ m$ the maximum elevation for the hydraulic gradeline in the first scenario was about +80 m and about -15 m in the second scenario. These results clearly shows that the large storage capacity of the Thornton reservoir effectively controlled and stabilized the hydraulic transients in the Calumet system.

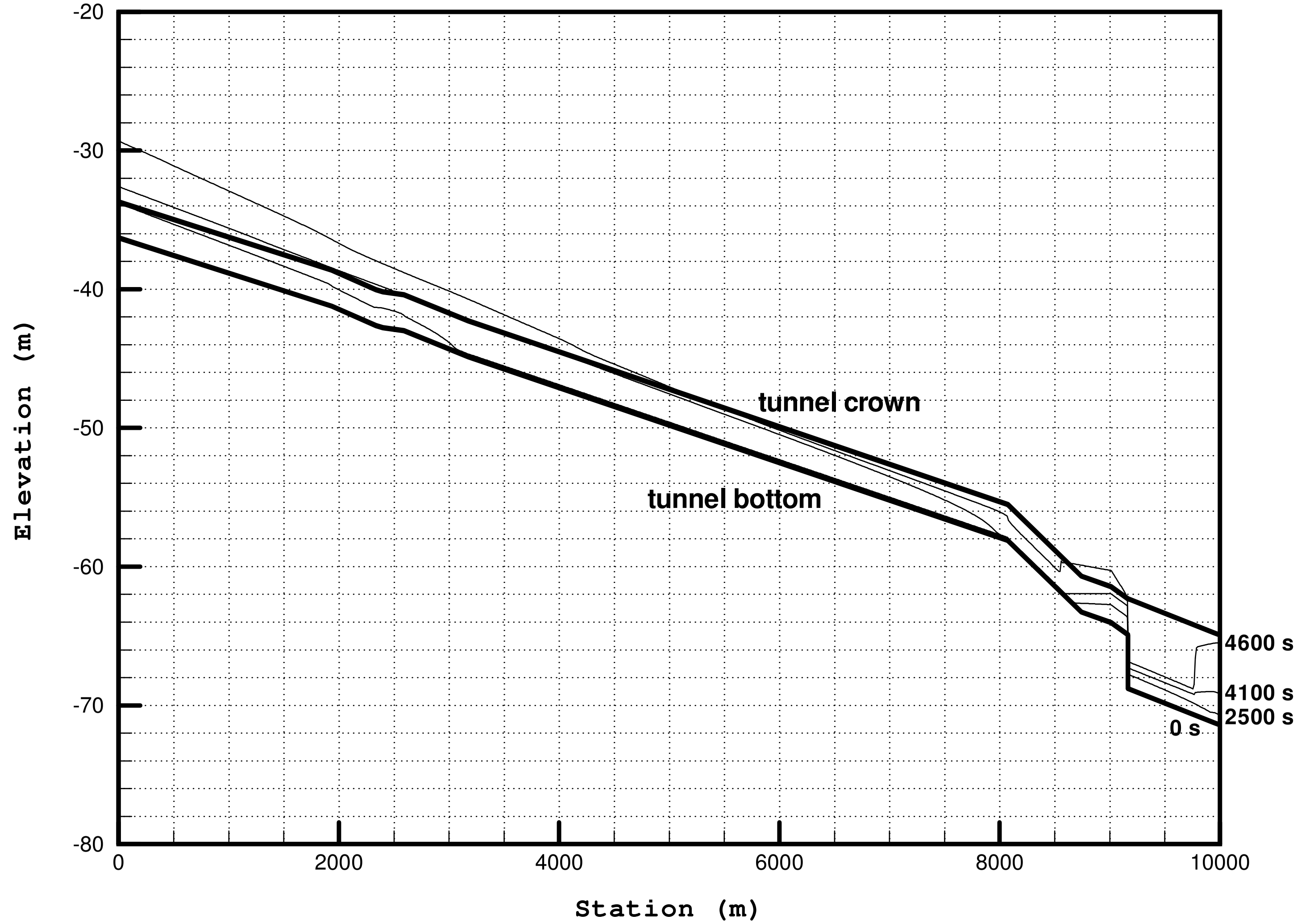

Figure 5.20: Computed hydraulic gradelines between stations $x = 0$ m and $x = 10000$ m from 0 s to 4600 s (with reservoir).

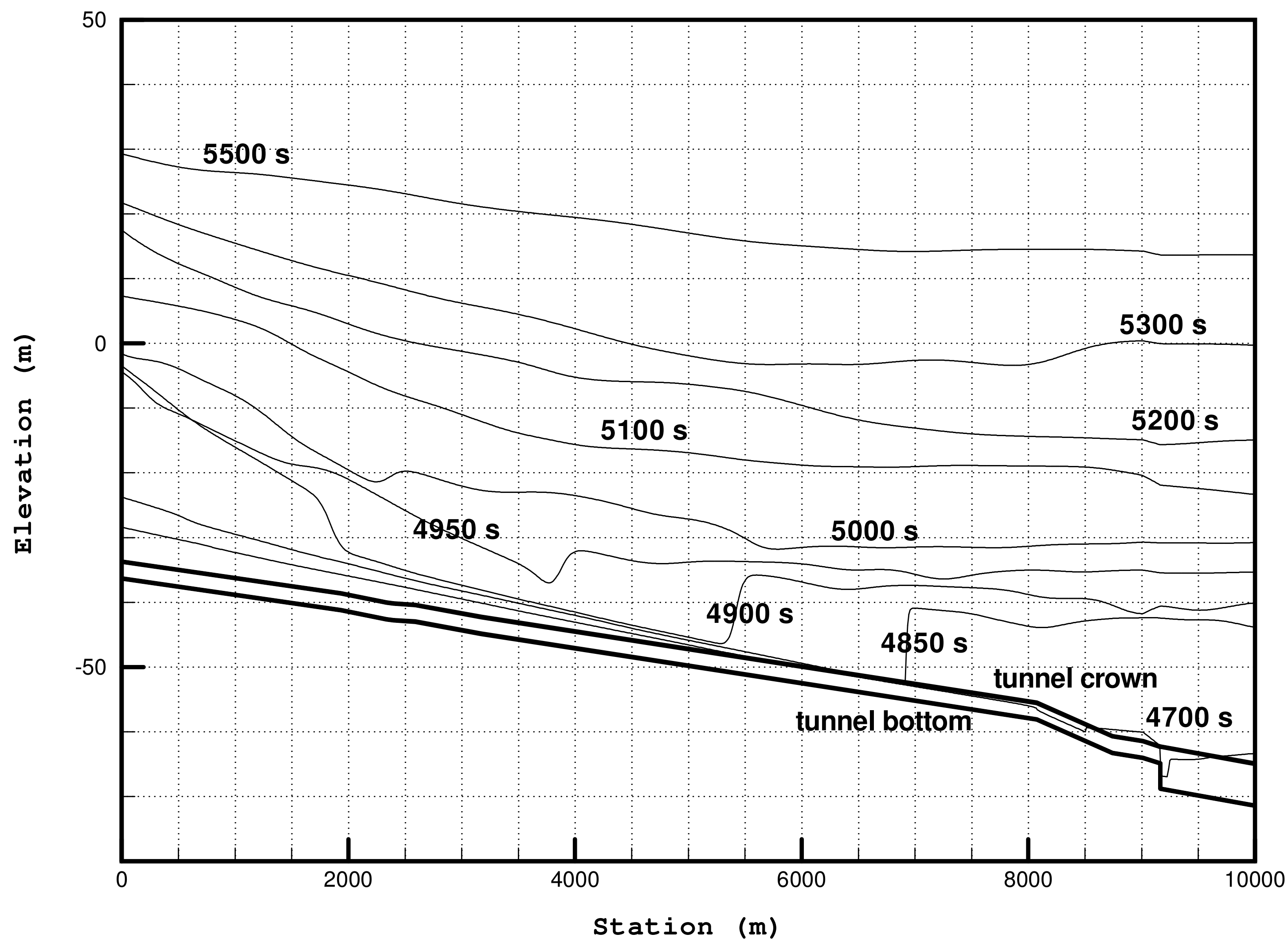

Figure 5.21: Computed hydraulic gradelines between stations $x = 0$ m and $x = 10000$ m from 4700 s to 5500 s (with reservoir).

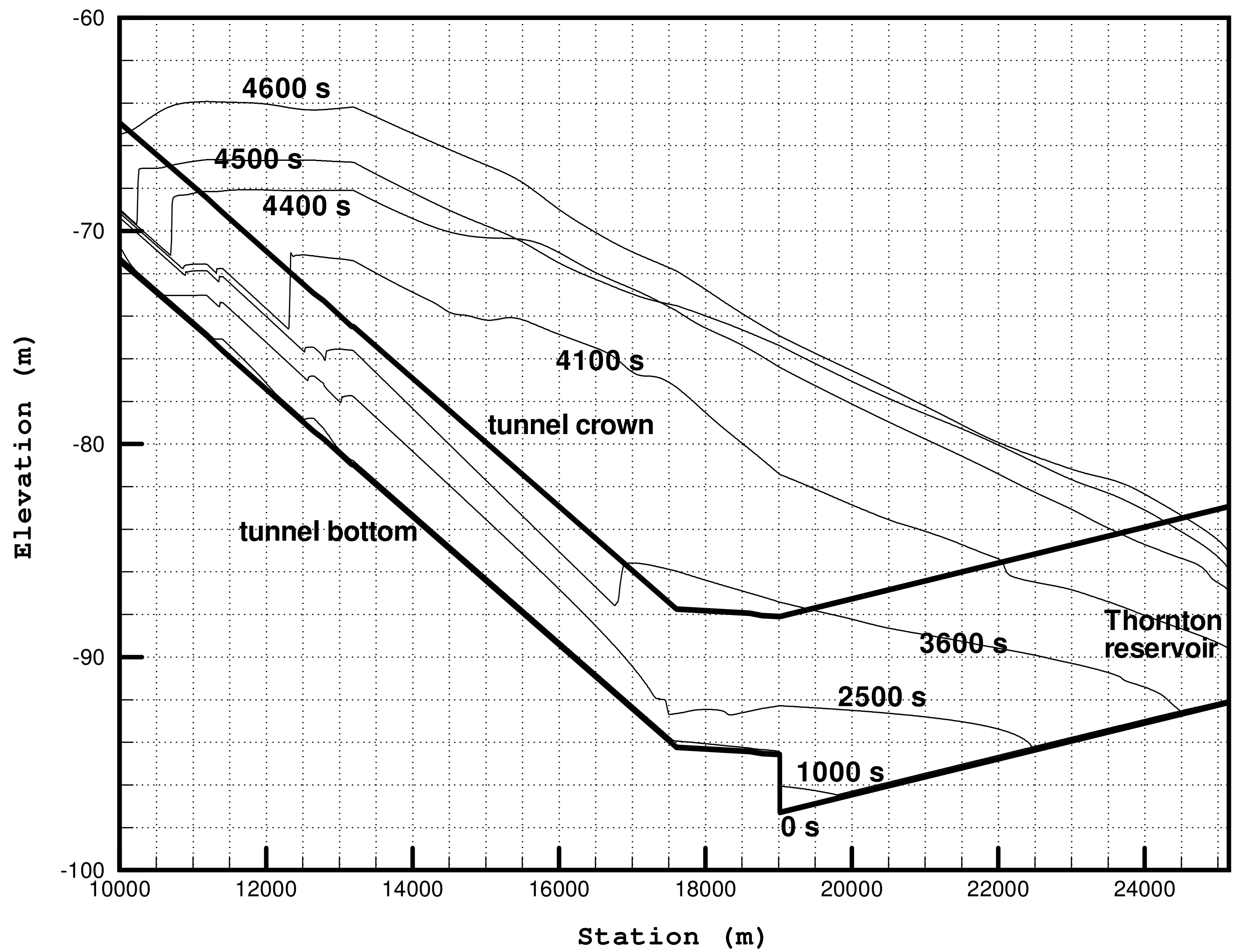

Figure 5.22: Computed hydraulic gradelines between stations $x = 10000$ m and $x = 25150$ m from 0 s to 4600 s (with reservoir).

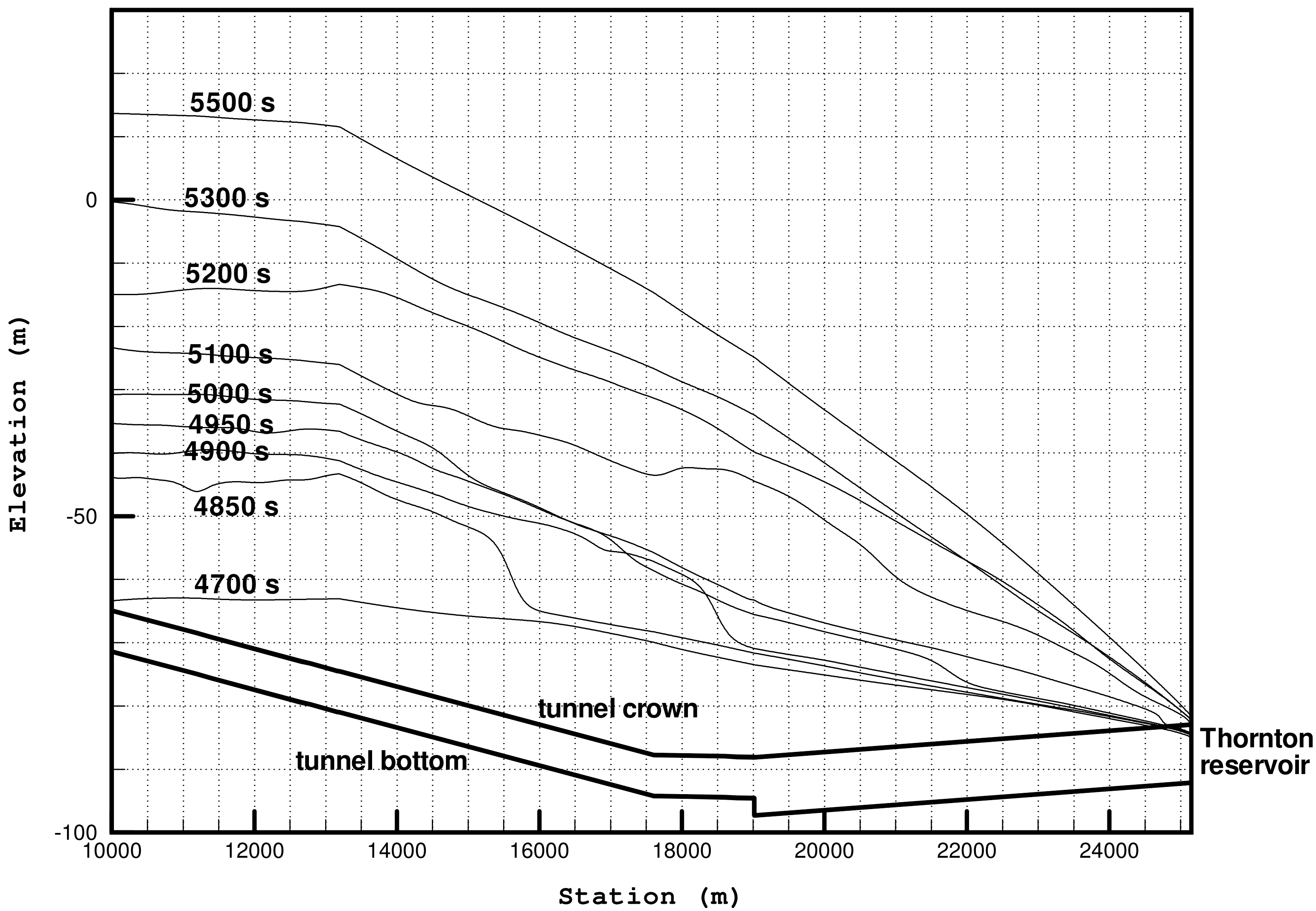

Figure 5.23: Computed hydraulic gradelines between stations $x = 10000$ m and $x = 25150$ m from 4700 s to 5500 s (with reservoir).

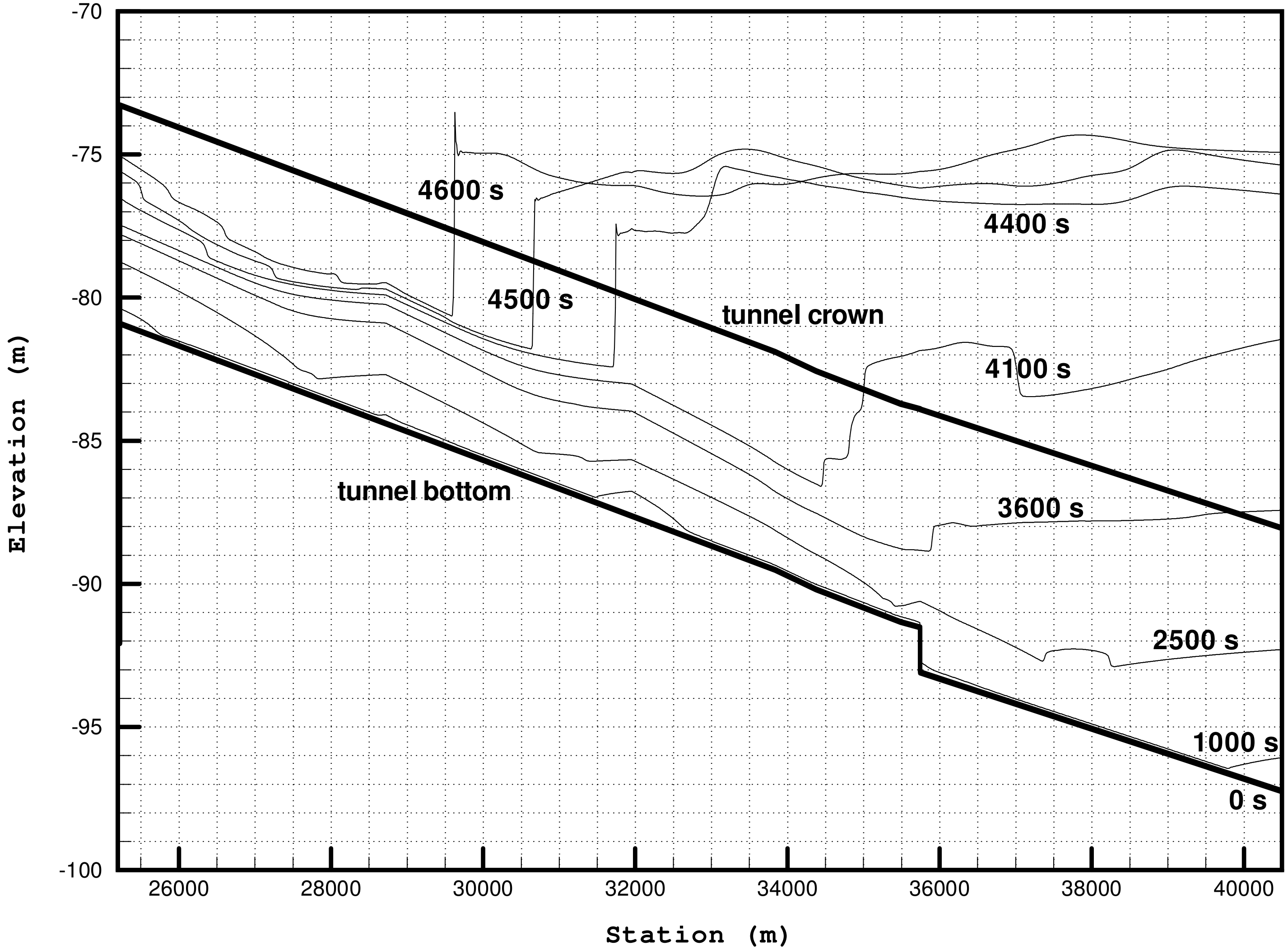

Figure 5.24: Computed hydraulic gradelines between stations $x = 25200$ m and $x = 40500$ m from 0 s to 4600 s (with reservoir).

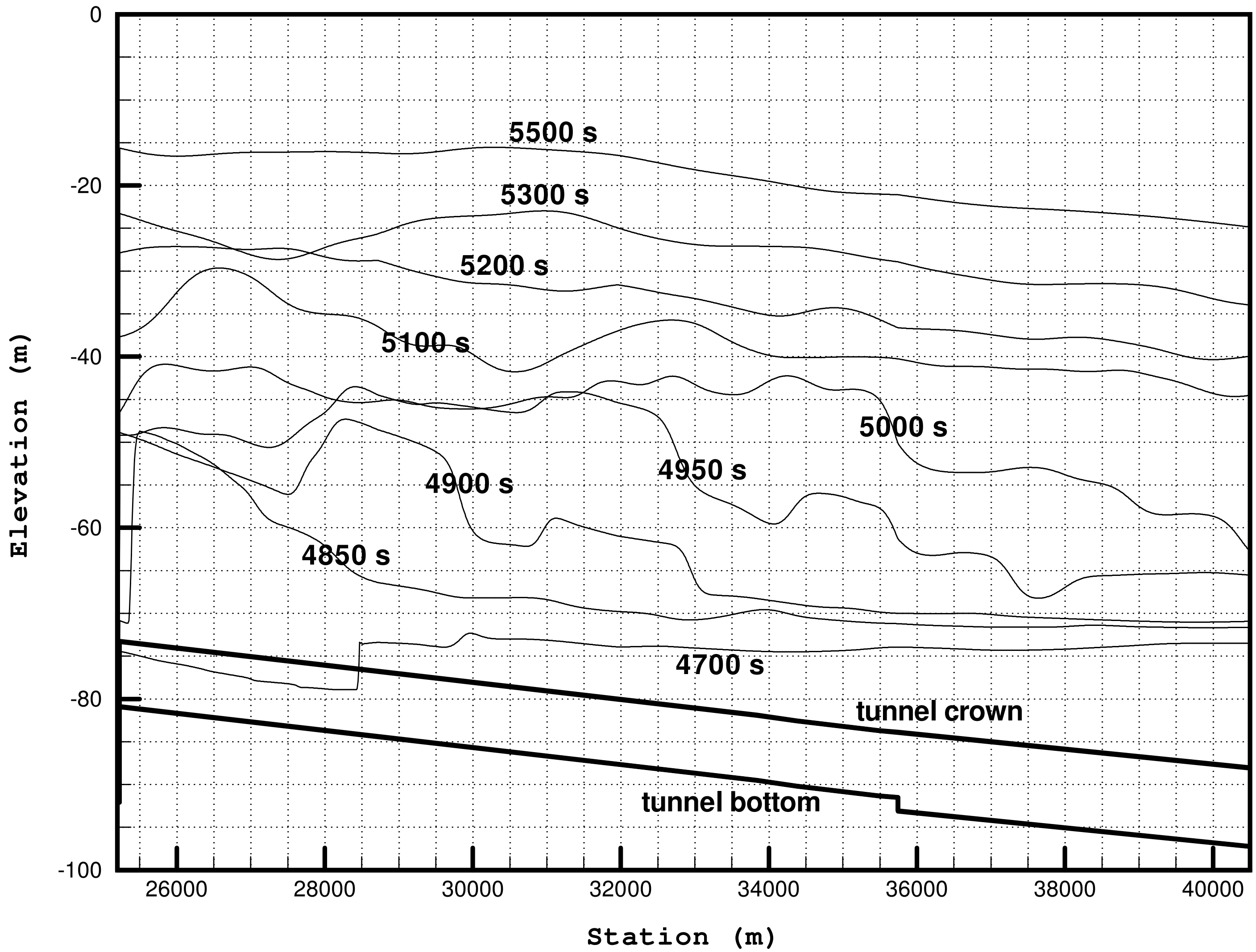

Figure 5.25: Computed hydraulic gradelines between stations $x = 25200$ m and $x = 40500$ m from 4700 s to 5500 s (with reservoir).

Chapter 6

Conclusion

The main aim of this thesis is to advance our understanding of the process of flood-wave propagation through storm-sewer systems by improving the methods available for simulating unsteady flows in closed conduits ranging from free surface flows, to partly free surface-partly pressurized flows (mixed flows), to fully pressurized flows. The formulated models can accurately describe complex flow features –such as negative open channel-pressurized flow interfaces, interface reversals, and open-channel surges– that have not been addressed well, or not considered at all, by previous models. This work also represents an advance in computational efficiency, economy in terms of memory requirements, and improved accuracy.

Specifically, this thesis has accomplished the following:

1. Two fully-conservative, efficient and robust models capable of simulating unsteady flows in closed conduits ranging from free surface flows, to partly free surface-partly pressurized flows, to fully pressurized flows have been implemented. In the first model, pressurized flows are simulated as free surface flows using a hypothetical narrow open-top slot ("Preissmann slot"). In the second model, free surface and pressurized flows are treated

independently while interacting through a moving interface.

In the first model, a gradual transition between the pipe and the slot is introduced and an explicit Finite Volume (FV) Godunov-type Scheme (GTS) is used to solve the free surface flow governing equations. This model is called the *modified Preissmann model*. It is clear that any model implemented within the Preissmann slot framework is valid only for conditions where no sub-atmospheric flows occur. Numerical tests for free surface and pressurized flows show that to achieve a given level of accuracy, second-order GTS schemes are significantly faster to execute than the fixed-grid Method of Characteristics (MOC) with space-line interpolation, which has been the most frequently used scheme for simulating transient flows in sewers.

In the second model, both free surface and pressurized flows are handled using shock-capturing methods –specifically GTS schemes. These methods capture discontinuities in the solution automatically, without explicitly tracking them (LeVeque 2002). Open channel-pressurized flow interfaces are treated using a shock tracking-capturing approach. In this case, cell boundaries are introduced at the location of open channel-pressurized flow interfaces, subdividing some regular cells into two sub-cells, resulting in a variable mesh arrangement that varies from one time step to the next. However, the vast majority of grid cells do not vary. By introducing a cell boundary at each open channel-pressurized flow interface, we can avoid the smearing and loss of accuracy that are inevitable when the discontinuity falls within a grid cell and the discrete solution is averaged over the cell.

Comparisons between simulated results and experiments reported in the literature show that the two formulated models can accurately describe complex flow features –such as negative open channel-pressurized flow interfaces, interface reversals, and open-channel surges. Numerical simulations also show that the formulated models are able to produce stable results for strong (rapid) transients at field scale. Comparisons of numerical efficiency between the formulated models show that the shock-tracking-capturing model is slightly more efficient than the *modified Preissmann model*. Even so, only the *modified Preissmann model* was implemented numerically for complex networks. The reason is that the numerical implementation of this model is much simpler than that based on a shock tracking-capturing approach.

2. Intrinsically conservative and second-order accurate boundary conditions have been implemented. The proposed formulation for boundary conditions maintains the conservation property of FV schemes and does not require any special treatment to handle shocks at boundaries. A numerical scheme may have second or higher-order accuracy in the internal cells. However, if this scheme is coupled with the boundary conditions having only first-order accuracy, a degradation of the accuracy of the scheme in the internal cells may occur. Thus, for the preservation of the accuracy of the numerical solution, it is necessary to use the same order of accuracy in all the cells of the computational domain (e.g., LeVeque 2002, Guinot 2003, León et al. 2006c). In the proposed models, the boundary conditions are implemented using the same order of accuracy as the internal cells (second-order).

3. The *modified Preissmann model* has been applied to simulate transient flows in complex hydraulic systems. The Tunnel and Reservoir Plan

(TARP) Calumet system of the Metropolitan Water Reclamation District of Greater Chicago is used as the test case. This application was only intended to illustrate the capability of this model in simulating the formation and propagation of hydraulic transients in complex hydraulic systems.

In general, the scope of this work is limited to single-phase flows (liquids). However, a simplified model for air-water mixture flows, which is valid when the amount of gas in the conduit is small, has been implemented in the pressurized flow regime. This work does not include the prediction of any type of air entrainment or air release.

In view of the results and conclusions obtained in this study, the following may be worth considering for future investigations.

1. A comprehensive experimental investigation for sewer networks in single and two-phase flow conditions, which goes beyond simply calibrating existing models, is necessary in order to understand the flow behavior and to guide future model development.

2. Since much of the complex dynamics in unsteady sewer flows is due to the air phase; it is suggested to incorporate the air-phase flow component to the mixed flow model.

3. Implementation of the shock tracking-capturing approach for complex systems.

References

[1] Ackers, P., and Harrison, A. J. M. (1964). "Attenuation of flood waves in partfull pipes." *Proc. of the Institution of Civil Engineers*, 28, 361-382.

[2] Alcrudo, F., Garcia-Navarro, P., and Saviron, J-M. (1992). "Flux-difference splitting for 1D open channel flow equations." *Int. J. for Numerical Methods in Fluids*, 14, 1009-1018.

[3] Brook, B. S., Falle, S. A. E. G., and Pedley, T. J. (1999). "Numerical solutions for unsteady gravity-driven flows in collapsible tubes: Evolution and roll-wave instability of a steady state." *J. Fluid Mech.*, 396, 223-256.

[4] Bziuk, P. T. (1988). "An experimental investigation of the pressure transients during the transition from gravity flow to surcharged flow in a storm sewer system." *BASc. thesis, University of Windsor, Windsor, Ontario, Canada.*

[5] Caleffi, V., Valiani, A., and Zanni, A. (2003). "Finite volume method for simulating extreme flood events in natural channels." *J. Hydraul. Research*, 41(2), 167-177.

[6] Cannizzaro, D., and Pezzinga, G. (2005). "Energy dissipation in transient gaseous cavitation." *J. Hydraul. Eng.*, 131(8), 724-732.

[7] Cardle, J. A. (1984). "An investigation of hydraulic transients in combination free surface and pressurized flows." *Ph.D. thesis, Dept. of Civil and Mineral Eng., Univ. of Minessota, USA.*

[8] Cardle, J. A., Song, C. C. S. and Yuan, M. (1988). "Measurements of mixed transient flows." *J. Hydraul. Eng.*, 115(2), 169-182.

[9] Chaudhry, M. H. (1987). *Applied hydraulic transients*, 2nd edition, Van Nostrand Reinhold, New York.

[10] Chaudhry, M. H., and Hussaini, M. Y. (1985). "Second-order accurate explicit finite-difference schemes for water hammer analysis." *J. Fluids Eng.*, 107, 523-529.

[11] Chaudhry, M. H., Bhallamudi, S. M., Martin, C. S., and Naghash, M. (1990). "Analysis of transient in bubbly homogeneous, gas-liquid mixtures." *J. Fluids Eng.*, 112, 225-231.

[12] Chen, C. L. (1995). "Free surface stability criterion as affected by velocity distribution." *J. Hydraul. Eng.*, 121(2), 736-743.

[13] Cunge, J. A. and Wegner, M. (1964). "Intégration numérique des équations d'écoulement de Barré de Saint-Venant par un schéma implicite de différences finies: Application au cas d'une galerie tantôt à surface libre." *La Houille Blanche*, 1, 33-39.

[14] Dressler, R. (1949). "Mathematical solution of the problem of roll-waves in inclined open channels." *Commun. Pure Appl. Math.*, 2, 149-194.

[15] Franz, D. D., and Melching, C. S. (1997). "Full Equations (FEQ) model for the solution of the full, dynamic equations of motion for one-dimensional unsteady flow in open channels and through control structures." *U.S. Geological Survey Water-Resources investigations*, Urbana, Illinois, USA, Report 96-4240.

[16] Fuamba, M. (2002). "Contribution on transient flow modelling in storm sewers." *J. Hydraul. Research*, 40(6), 685-693.

[17] Fujihara, M., and Borthwick, A. G. L. (2000). "Godunov-type solution of curvilinear shallow water equations." *J. Hydraul. Eng.*, 126(11), 827-836.

[18] Ghidaoui, M. S. (2004). "Review of sewer surcharging phenomena and models." *Internal Technical Rep.*, Univ. of Illinois at Urbana - Champaign, Urbana, IL.

[19] Ghidaoui, M. S., and Cheng, Y. P. H. (1997). "Energy equation in unsteady open channel flows: Formulation and application." *Advances in Comput. Eng. Sience*, 582-587.

[20] Ghidaoui, M. S., and Karney, B. W. (1994). "Equivalent differential equations in fixed-grid characteristics method." *J. Hydraul. Eng.*, 120(10), 1159-1175.

[21] Ghidaoui, M. S., Karney, B. W., and McInnis, D. A. (1998). "Energy estimates for discretization errors in water hammer problems." *J. Hydraul. Eng.*, 124(4), 384-393.

[22] Ghidaoui, M. S. and Kolyshkin, A. A. (2002). "Roll waves and surges in channels: Onset and initial development." *Proc., 2nd International Symposium on Flood Defense*, Beijing, China.

[23] Ghidaoui, M. S., Zhao, M., McInnis, D. A., and Axworthy, D. H. (2005). "A review of water hammer theory and practice." *Applied Mechanics Review, ASME*, 58(1), 49-76.

[24] Glaister, P. (1988). "Approximate Riemann solutions of the shallow water equations." *J. Hydraul. Research*, 26(3), 293-306.

[25] Godunov, S. K. (1959). "Finite difference methods for the computation of discontinuous solutions of the equations of fluid mechanics." *Math. Sbornik*, 47, 271-306.

[26] Goldberg, D. E., and Wylie, E. B. (1983). "Characteristics method using time-line interpolations." *J. Hydraul. Eng.*, 109(5), 670-683.

[27] Guinot, V. (2000). "Riemann solvers for water hammer simulations by Godunov method." *Int. J. Numer. Methods Eng.*, 49, 851-870.

[28] Guinot, V. (2001a). "Numerical simulation of two-phase flow in pipes using Godunov method." *Int. J. Numer. Meth. in Eng.*, 50, 1169-1189.

[29] Guinot, V. (2001b). "The discontinuous profile method for simulating two-phase flow in pipes using the single component approximation." *Int. J. Numer. Meth. Fluids*, 37, 341-359.

[30] Guinot, V. (2003). *Godunov-type schemes*, Elsevier Science B.V., Amsterdam, The Netherlands.

[31] Guo, Q., and Song, C. C. S. (1990). "Surging in urban storm drainage systems." *J. Hydraul. Eng.*, 116(12), 1523-1537.

[32] Guo, Q., and Song, C. C. S. (1991). "Dropshaft hydrodynamics under transient conditions." *J. Hydraul. Eng.*, 117(8), 1042-1053.

[33] Hamam, M. A. (1982). "Transient of gravity to surcharged flow." *Ph.D. thesis, Univ. of Windsor, Windsor, Ontario, Canada.*

[34] Hamam, M. A. and McCorquodale, J. A. (1982). "Transient conditions in the transition from gravity to surcharged sewer flow." *Canadian J. of Civ. Eng.*, 9, 189-196.

[35] Hirsch, C. (1990). *Numerical computation of internal and external flows*, Vols. 1 and 2, Wiley, New York.

[36] Holly, M., and Preissmann, A. (1977). "Accurate calculation of transport in two dimensions." *J. Hydraul. Eng.*, 103(11), 1259-1277.

[37] Hwang, Y-H., and Chung, N-M. (2002). "A fast Godunov method for the water hammer problem." *Int. J. Numer. Meth. Fluids*, 40, 799-819.

[38] Karney, B. W. (1990). “Energy relations in transient closed-conduit flow.” *J. Hydraul. Eng.*, 116(10), 1180-1196.

[39] Karney, B. W. and Ghidaoui, M. S. (1997). “Flexible discretization algorithm for fixed-grid MOC in pipelines.” *J. Hydraul. Eng.*, 123(11), 1004-1011.

[40] Kordyban, E. (1977). “Some characteristics of high waves in closed channels approaching Kelvin-Helmholtz instability.” *J. Fluids Eng.*, 99, 339-346.

[41] Kranenburg, C. (1990). “On the stability of gradually varying flow in wide open channels.” *J. Hydraul. Research*, 28, 621-628.

[42] Kranenburg, C. (1992). “On the evolution of roll waves.” *J. Fluid Mech.*, 245, 249-261.

[43] Lai, C. (1989). “Comprehensive method of characteristics models for flow simulation.” *J. Hydraul. Eng.*, 114(9), 1074-1095.

[44] Langseth, J. O. (1996). “On an implementation of a front tracking method for hyperbolic conservation laws.” *Advances in Eng. Software*, 26(1), 45-63.

[45] León, A. S., Ghidaoui, M. S., Schmidt, A. R., and García, M. H. (2005). “Importance of numerical efficiency for real time control of transient gravity flows in sewers.” *Proc., XXXI IAHR Congress*, Seoul, Korea.

[46] León, A. S., Ghidaoui, M. S., Schmidt, A. R., and García, M. H. (2006a). “Godunov-type solutions for transient flows in sewers.” *J. Hydraul. Eng.*, 132(8), 800-813.

[47] León, A. S., Ghidaoui, M. S., Schmidt, A. R., and García M. H. (2006b). “An efficient numerical scheme for modeling two-phase bubbly homogeneous air-water mixtures.” *Proc., ASCE-EWRI World Water and Environmental Congress*, Omaha, Nebraska.

[48] León, A. S., Ghidaoui, M. S., Schmidt, A. R., and García, M. H. (2006c). “An efficient second-order accurate shock capturing scheme for modeling one and two-phase waterhammer flows.” *J. Hydraul. Eng.* Submitted for review.

[49] León, A. S., Schmidt, A. R., Ghidaoui, M. S., and García, M. H. (2006d). “Review of sewer surcharging phenomena and models.” *Civil Engineering Studies, Hydraulic Engineering Series No. 78*, Univ. of Illinois, Urbana, IL.

[50] Leonard, B. P. (1991). “The ultimate conservative difference scheme applied to unsteady one-dimensional advection.” *Comput. Methods Appl. Mech. Eng.*, 88, 17-74.

[51] LeVeque, R. J. (2002). *Finite volume methods for hyperbolic problems*, Cambridge Univ. Press, Cambridge.

[52] LeVeque, R. J., and Shyue K. M. (1995). "One-dimensional front tracking based on high resolution wave propagation methods." *SIAM J. Sci. Comput.*, 16, 348-377.

[53] Li, J., and McCorquodale, A. (1999). "Modeling mixed flow in storm sewers." *J. Hydraul. Eng.*, 125(11), 1170-1180.

[54] Liang, J. H., Ghidaoui, M. S., Deng, J. Q., and Gray, W. G. (2007). "A Boltzmann-based finite volume algorithm for surface water flows on cells of arbitrary shapes." *J. Hydraul. Research*, Submitted for review.

[55] Liggett, J. A., and Chen, L. C. (1994). "Monitoring water distribution systems: the inverse method as a tool for calibration and leak detection." *Proc., Conf. on Improving Efficiency and Reliability of Water Distribution Sys.*

[56] Martin, C. S. (1993). "Pressure-wave propagation in two-component flow." *Proc., Computer modeling of free-surf. and press. flows*, NATO ASI Series E, Applied Sciences Vol. 274, Pullman, WA, U.S.A., 519-552.

[57] Padmanabhan, M., and Martin, C. S. (1978). "Shock-wave formation in flowing bubbly mixtures by steepening of compression waves." *Int. J. Multiphase Flow*, 4, 81-88.

[58] Pagliara, S., and Yen, B. C. (1997). "Sewer network hydraulic model: NISN." *Civil Eng. Studies, Hyd. Eng. Series no.53.*, Dept. of Civil Eng., Univ. of Illinois at Urbana - Champaign, Urbana, IL.

[59] Pezzinga, G. (2000). "Evaluation of unsteady flow resistances by quasi-2D or 1D models." *J. Hydraul. Eng.*, 126(10), 778-785.

[60] Sanders, B. F. (2001). "High-resolution and non-oscillatory solution of the St. Venant equations in non-rectangular and non prismatic channels." *J. Hydraul. Research*, 39(3), 321-330.

[61] Sanders, S. (2005). "Deep Tunnel." *WGN-TV CoverStories: WGN-TV, Oct. 10, 2005.* (Oct. 18, 2006).

[62] Schmidt, A. R., Ghidaoui, M. S., León, A. S., and García, M. H. (2005). "Review of sewer surcharging phenomena and models." *Proc., XXXI IAHR Congress*, Seoul, Korea.

[63] Sibetheros, I. A., Holley, E. R., and Branski, J. M. (1991). "Spline interpolations for water hammer analysis." *J. Hydraul. Eng.*, 117(10), 1332-1349.

[64] Song C. C. S., Cardle J. A., and Leung, K. S. (1984). "Transient mixed-flow models for storm sewers." *J. Hydraul. Eng.*, 109(11), 1487-1503.

[65] Szymkiewicz, R., and Mitosek, M. (2004). "Analysis of unsteady pipe flow using the modified finite element method." *Commun. in Numer. Meth. in Eng.*, 21(4), 183-199.

[66] Toro, E. F. (2001). *Shock-capturing methods for free-surface shallow flows*, Wiley, LTD, Chichester, U.K.

[67] Trajkovic, B., Ivetic, M., Calomino, F., and D'Ippolito, A. (1999). "Investigation of transition from free surface to pressurized flow in a circularpipe." *Water Science and Technology*, 39(9), 105-112.

[68] Vasconcelos, J. G. and Wright, S. J. (2003). "Surges associated with air expulsion in near-horizontal pipelines." *Proc. of FEDSM'03, 4th ASME-JSME Joint Fluids Engineering Conference*, Honolulu, Hawaii, USA, July 6-11, 2003.

[69] Vasconcelos, J. G., Wright, S. J., and Roe, P. L. (2006). "Improved simulation of flow regime transition in sewers: Two-component pressure approach." *J. Hydraul. Eng.*, 132(6), 553-562.

[70] Ven Te Chow Hydrosystems Lab. (2006). "Applied Research: Tunnel And Reservoir Plan." <http://vtchl.uiuc.edu/applied-research/environmental-hydraulics/tarp/> (Oct. 18, 2006).

[71] Wiggert, D. C. (1972). "Transient flow in free-surface, pressurized systems." *J. Hydraul. Division, ASCE*, 98(1), 11-27.

[72] Wiggert, D. C. and Sundquist, M. J. (1977). "Fixed-grid characteristics for pipeline transients." *J. Hydraul. Eng.*, 103(12), 1403-1415.

[73] Wood, D. J., Lingireddy, S., Boulos, P. F., Karney, B. W., and McPherson, D. L. (2005). "Numerical methods for modeling transient flow in distribution systems." *J. of the American Water Works Association*, 97(7), 104-115.

[74] Wylie, E. B., and Streeter, V. L. (1983). *Fluid transients*, FEB Press, Ann Arbor, Michigan.

[75] Wylie, E. B., and Streeter, V. L. (1993). *Fluid transient in systems*, Prentice-Hall, Englewood Cliffs, N.J.

[76] Yen, B. C. (1986). *Hydraulics of sewers*, Chapter 1 in Advances in Hydroscience, Urban Storm Drainage, Academic Press, London, Vol. 14, 1-115.

[77] Yen, B. C. (2001). *Hydraulics of sewer systems*, in Stormwater collection systems design Handbook, McGraw-Hill.

[78] Zanuttigh, B., and Lamberti, A. (2002). "Roll waves simulation using shallow water equations and Weighted Average Flux method." *J. Hydraul. Research*, 40(5), 610-622.

[79] Zhao, M., and Ghidaoui, M. S. (2004). "Godunov-type solutions for water hammer flows." *J. Hydraul. Eng.*, 130(4), 341-348.

[80] Zielke, W., Perko, H. D., and Keller, A. (1989). "Gas release in transients pipe flow." *Proc., 6th International Conference on Pressure Surges*, BHRA, Cambridge, England, Oct. 4-6, 3-13.

[81] Zoppou, C., and Roberts, S. (2003). "Explicit schemes for dam-break simulations." *J. Hydraul. Eng.*, 129(1), 11-34.

Author's Biography

Arturo S. León was born in Ayacucho, Peru, on January 26, 1975. He graduated from the National University of San Cristobal de Huamanga (Peru) in 1996 with a Bachelor degree in Civil Engineering. In 1998, he obtained the title of Civil Engineer in the same university. In 2000, he obtained the degree of Master of Science in Hydraulic Engineering from the National University of Engineering (Lima-Peru).

From 1996 to 2002 before he joined the University of Illinois, Mr. León worked as a research and teaching assistant, and as a hydraulic engineer. As a research assistant, he worked intensively on local scour experiments around cylindrical piers (Master thesis). As a teaching assistant, he assisted in teaching the courses of "Fluid Mechanics I" and "Fluid Mechanics II". As a hydraulic engineer, he worked in the design and construction of several hydraulic structures including, channels, culverts, intakes, dams, drop structures, energy dissipators, tunnels, road drainage, pumping stations, erosion and sediment control structures, etc. During this period, he also published two books (in Spanish).

At the University of Illinois, Mr León has been working on developing a transient mixed flow (simultaneous occurrence of free surface and pressurized flows) model. He also worked as a teaching assistant for two courses "Hydraulic Analysis and Design of Engineering Systems" and "Open Channel Hydraulics" in 2004 and 2005. He is also an author of one book chapter and several journal and conference papers.